Liliang Ouyang

Study on Microextrusion-based 3D Bioprinting and Bioink Crosslinking Mechanisms

Springer

Springer Theses

Recognizing Outstanding Ph.D. Research

Aims and Scope

The series "Springer Theses" brings together a selection of the very best Ph.D. theses from around the world and across the physical sciences. Nominated and endorsed by two recognized specialists, each published volume has been selected for its scientific excellence and the high impact of its contents for the pertinent field of research. For greater accessibility to non-specialists, the published versions include an extended introduction, as well as a foreword by the student's supervisor explaining the special relevance of the work for the field. As a whole, the series will provide a valuable resource both for newcomers to the research fields described, and for other scientists seeking detailed background information on special questions. Finally, it provides an accredited documentation of the valuable contributions made by today's younger generation of scientists.

Theses are accepted into the series by invited nomination only and must fulfill all of the following criteria

- They must be written in good English.
- The topic should fall within the confines of Chemistry, Physics, Earth Sciences, Engineering and related interdisciplinary fields such as Materials, Nanoscience, Chemical Engineering, Complex Systems and Biophysics.
- The work reported in the thesis must represent a significant scientific advance.
- If the thesis includes previously published material, permission to reproduce this must be gained from the respective copyright holder.
- They must have been examined and passed during the 12 months prior to nomination.
- Each thesis should include a foreword by the supervisor outlining the significance of its content.
- The theses should have a clearly defined structure including an introduction accessible to scientists not expert in that particular field.

More information about this series at http://www.springer.com/series/8790

Liliang Ouyang

Study
on Microextrusion-based 3D
Bioprinting and Bioink
Crosslinking Mechanisms

Doctoral Thesis accepted by
Tsinghua University, Beijing, China

Author
Dr. Liliang Ouyang
Department of Mechanical Engineering
Tsinghua University
Beijing, China

Supervisors
Prof. Wei Sun
Department of Mechanical Engineering
Tsinghua University
Beijing, China

Department of Mechanical Engineering
and Mechanics
Drexel University
Philadelphia, USA

Prof. Jason A. Burdick
Department of Bioengineering
University of Pennsylvania
Philadelphia, USA

Supervisor's Foreword

It is my great pleasure to introduce Dr. Ouyang's thesis work, which is recognized as an Outstanding Doctoral Thesis by Tsinghua University. Dr. Ouyang joined my laboratory and started his Ph.D. study in September 2012, working on extrusion-based 3D bioprinting, novel bioink development, and embryonic stem cell printing. In 2015, he received a scholarship from the China Scholarship Council and conducted one-year visiting research with Prof. Jason A. Burdick at the University of Pennsylvania. Dr. Ouyang completed his doctoral work in July 2017, ending up with an impressive list of high-impact publications in the field of biofabrication.

In this dissertation, Dr. Ouyang presents a comprehensive study on microextrusion 3D bioprinting as well as the mechanisms of bioink crosslinking. Three-dimensional bioprinting is normally referred to using living cells as building blocks for constructing cellular structures, where the cell-containing ink materials are termed as bioinks. In the last decade, 3D bioprinting has been witnessed with numerous progresses and applications, while the fundamentals of the printing technology, as well as the effect of printing process and bioink crosslinking on the structural printability and cellular function, have not been fully investigated. To bridge this gap, Dr. Ouyang has conducted a comprehensive study on the microextrusion-based cell-printing process, and the use of responsive bioinks and their crosslinking. A number of novel printing/crosslinking strategies were developed and presented in this thesis work, for example, a dual-crosslinking strategy for shear-thinning supermolecular bioink printing (Chap. 4), a synergetic optimization method for thermo-responsive bioink printing (Chap. 5), and an in-situ crosslinking strategy for printing non-viscous photo-crosslinkable hydrogels (Chap. 6). In addition, this thesis also reports some fundamental studies on a signal pathway activation, cell–matrix interaction, as well as a proliferation-induced embryoid body (EB) formation mechanism as results of bioprinting (Chap. 7). Findings, as well as the developed methodologies from those studies, have greatly enriched the field of bioprinting.

I am proud of Dr. Ouyang for what he has accomplished during his Ph.D. study and proud of presenting this thesis book to the bioprinting and biofabrication community.

Beijing, China/Philadelphia, USA   Prof. Wei Sun, Ph.D.
May 2019

Parts of this Thesis have been Published in the Following Documents:

Journal Publications:

Ouyang L, Highley CB, Sun W, Burdick JA. A Generalizable Strategy for the 3D Bioprinting of Hydrogels from Nonviscous Photo-crosslinkable Inks. *Advanced Materials*. 2017; 29(8):1604983.

Ouyang L, Yao R, Zhao Y, Sun W. Effect of bioink properties on printability and cell viability for 3D bioplotting of embryonic stem cells. *Biofabrication*. 2016; 8(3):035020.

Ouyang L[#], Highley CB[#], Rodell CB, Sun W, Burdick JA. 3D Printing of Shear-Thinning Hyaluronic Acid Hydrogels with Secondary Cross-Linking. *ACS Biomaterials Science & Engineering*. 2016; 2(10):1743–1751. ([#] Equal contribution)

Ouyang L[#], Yao R[#], Mao S, Chen X, Na J, Sun W. Three-dimensional bioprinting of embryonic stem cells directs high-throughput and highly uniform embryoid body formation. *Biofabrication*. 2015; 7(4):044101. ([#] Equal contribution)

Ouyang L[#], Yao R[#], Chen X[#], Na J, Sun W. 3D printing of HEK 293FT cell-laden hydrogel into macroporous constructs with high cell viability and normal biological functions. *Biofabrication*. 2015; 7(1):015010. ([#] Equal contribution)

Zhang T, Yan KC, Ouyang L, Sun W. Mechanical characterization of bioprinted in vitro soft tissue models. *Biofabrication*. 2013; 5(4):045010.

Acknowledgements

Mr. Long Zhao, Mr. Yu Li, Mrs. Jia Wang, Mr. Yongyi Quan, Mrs. Shuangshuang Mao, and Dr. Karen Chang Yan at THU, as well as Dr. Yi-cheun Yeh, Dr. Christopher B. Rodell, and Dr. Kwang Hong Song at UPenn.

I am profoundly grateful to all the teachers and mentors who have helped me in the last twenty-one years since my primary education. I am also very grateful to my friends for accepting me with nothing but trust.

I would like to say thank you to my parents and my big family for their spiritual support throughout my education and my life in general. I owe a unique debt of gratitude to my grandma, who has deeply impacted me with her easy philosophy of life. Last but not least, I would like to express my special appreciation to my beautiful wife Li for her unreserved support and contribution to my work and our family. She is a great wife and also a great mother.

Contents

Abbreviations

3DP	Three-dimensional Printing
3T3	NIH 3T3 Fibroblast
Ad	Adamantane
Ad-HA	Adamantane Hyaluronic Acid
Alg	Alginate
BSA	Bovine Serum Albumin
CAD	Computer-Aided Design
DAPI	4′,6-diamidino-2-phenylindole
DC	Dual Crosslinking
DMSO	Dimethyl Sulfoxide
DTT	DL-Dithiothreitol
EB	Embryoid Body
ECM	Extracellular Matrix
FBS	Fetal Bovine Serum
FDM	Fused Deposition Modeling
G′	Storage Modulus
G″	Loss Modulus
GAPDH	Glyceraldehyde 3-Phosphate Dehydrogenase
Gel	Gelatin
GelMA	Gelatin Methacryloyl
GH	Guest–Host
HA	Hyaluronic Acid
HEK 293FT	Human Embryonic Kidney 293FT cell
I2959	Irgacure 2959 (4-(2-hydroxyethoxy)phenyl-(2-propyl)ketone)
LAP	Lithium Phenyl-2,4,6-trimethylbenzoylphosphinate
LIF	Leukemia Inhibitory Factor
MeHA	Methacrylated Hyaluronic Acid
mESC	Mouse Embryonic Stem Cell
MMP	Matrix Metalloproteinase
MMP-deg	Matrix Metalloproteinase-degradable Crosslinker

Nanog	Homeodomain-bearing Transcriptional Factor
NorHA	Norbornene-functionalized Hyaluronic Acid
Oct-4	Octamer-Binding Transcription Factor 4
PBS	Phosphate-Buffered Saline
PCR	Polymerase Chain Reaction
PEG	Polyethylene Glycol
PEGDA	Poly(ethylene Glycol) Diacrylate
RGD	Arginine–Glycine–Aspartic Acid
SSEA1	Stage-Specific Embryonic Antigen 1
βCD	β-Cyclodextrin
βCD-HA	β-Cyclodextrin–Hyaluronic Acid
η	Viscosity
τ	Shear Force
$\dot{\gamma}$	Shear Rate
C	Circularity
Pr	Printability
v_{ink}	Ink Velocity
v_{noz}	Nozzle Velocity

Chapter 1
Introduction

3D printing (3DP), also known as additive manufacturing, is believed to be a revolutionary manufacturing technology in the twenty-first century [1, 2]. Compared with traditional processing techniques (e.g., turning, casting), 3DP benefits from the rapid prototyping of complex and customized structure: based on a bottom-to-up logic, 3DP allows for freeform manipulation of building blocks [3]. The properties of the materials being processed are critical to such a manufacturing fashion. This consideration has led to numerous progress in developing printable ink materials, including metal, ceramics, plastics, and elastomers.

The applications of 3DP in biomedicine vary with the ink materials and thus final products. For example, prototyping printed from non-biocompatible plastic could be used in surgery planning or guidance, while the customized orthodontic appliance would be another example. The next stage comes to the implantation of 3D printed product that is biocompatible but nondegradable, such as titanium bone scaffold [4]. One more step further, researchers have applied degradable biomaterials to print implantable scaffolds that would guide the native tissue regeneration and would thus achieve the ideal repair [5]. What this thesis presents belongs to another stage, where cells and other biological elements are directly incorporated in the 3DP process to create a living product, which is termed as 3D bioprinting [6]. This technology is supposed to lead to organ printing in the future, which might sound crazy but is actually happening.

1.1 Motivation

Organ failure is one of the major problems affecting human health. Traditional organ transplantation methods (e.g., autologous and allogeneic transplantation) experience fundamental challenges such as donor shortage, immune rejection, and ethical disputes. The number of people on the organ transplant waiting list continues to be much larger than the number of donors, which grows slowly. The recent progress in tissue engineering might provide new solutions to this problem.

As an interdisciplinary area, tissue engineering combines the fundamentals of engineering and life sciences and is dedicated to the development of biological alternatives for maintaining, repairing, or improving tissue function [7]. A traditional strategy for tissue engineering is to obtain a small number of patient-derived cells, which are expanded in vitro and seeded on a polymeric scaffold together with growth factors, followed by implantation [8]. Despite advances made in the past decades, a successful repair is still hindered by some enduring challenges such as cell seeding, complex scaffold and cellular heterogeneity [9]. Based on the idea of additive manufacturing, 3D printing manipulates building blocks spatially and temporarily and would be potential serving as a novel fabrication technology for tissue engineering [10]. For example, multi-material, pore-controllable, and complex acellular scaffolds have been fabricated.

Nevertheless, poor cell localization and mismatch with in vivo microenvironment remain problems. In 2003, researchers directly printed living cells using inkjet printing [11, 12], which led to a new research field—3D bioprinting. Since then, printing a cellular construct has become a new strategy for tissue engineering. 3D bioprinting combines the scaffold manufacturing with cell seeding, namely uses cell-containing ink materials, also known as bioinks, to build up tissue constructs directly. One of the most critical aspects in 3D bioprinting is the bioink, which not only determines the implementation of the printing technology but also defines the 3D cellular microenvironment [13]. Though numerous bioinks have been developed and applied in bioprinting practice, rarely few work has been done that could reveal the nature of bioprinting and bioinks and could summarize a practical guideline. Given this, we seek to carry out a comprehensive study on microextrusion 3D bioprinting from the perspective of the bioink crosslinking mechanism.

1.2 Scope and Contents

The topic of this thesis is 3D bioprinting, a multidisciplinary field involving manufacturing, biomaterials and regenerative medicine. The relevant keywords include 3D bioprinting, biofabrication, bioink, crosslinking and tissue engineering [14]. The objective of this thesis is to investigate a generalizable route for microextrusion bioprinting studies, which will be achieved by general analysis, comprehensive case studies, and applications proof-of-concept.

Specifically, bioink and its crosslinking mechanism are highlighted throughout the study. Different bioprinting technologies vary with bioink crosslinking strategies. By analyzing the general bioprinting process from raw materials to final products, we divide it into two parts, i.e., forming gel filament and building up 3D structure, both of which are closely associated with the crosslinking of bioink. In this study, three different microextrusion bioprinting technologies are developed and optimized based on different bioink crosslinking mechanisms, including guest-host self-assembly, gelatin-based thermal crosslinking and photo-crosslinking. All these technologies are studied following the same path, which includes process design, filament gener-

ation, structure fabrication, post-stabilization, cell damage control, and fundamental biological characterization.

A dual-crosslinking strategy was first used to facilitate the 3D bioprinting of hyaluronic acid (HA) based on guest-host chemistry and covalent crosslinking, where gel filaments were maintained by supramolecular bonds immediately upon extrusion until covalent crosslinking resulted in further stabilization. The printed scaffolds allowed for cell attachment and performed excellent mechanical properties, which suggested the potential in cartilage and cardiac tissue engineering considering the wide use of HA in these areas [15]. This approach does not require the use of other support materials or printable components and can be generalized to other hydrogels where supramolecular and covalent cross-linking chemistries can be combined [16]. Secondly, we introduced a practical method to optimize the typical gelatin-based printing process, where structure printability and cell viability were investigated simultaneously. The results indicated time-dependence of gelatin-based bioinks in addition to the commonly known thermal sensitivity. After optimization, mouse embryonic stem cells were printed into well-defined 3D hydrogel constructs with high cell viability (>90%) [17]. Thirdly, we developed a generalizable technology for the 3D bioprinting of photo-crosslinkable hydrogels without limitations to ink viscosity (can be low to 2.5 mPa·s). Different from commonly used pre- or post-crosslinking approaches, an in situ crosslinking strategy was established by introducing a photopermeable capillary to crosslink bioink and print standard filaments simultaneously. Various photo-crosslinkable hydrogels, both synthetic and natural with either ultraviolet or visible light, were tested in this system with excellent printability and embedded cell viability (>90%). Through incorporating a coaxial nozzle with this method, we were able to print complex building blocks, including core-shell, hollow tubular, and heterogeneous filaments where material composition varied along the filament [18].

These three systems call for different rheological properties and crosslinking mechanisms for bioinks, and yield products with varying properties, which could be utilized in a specific application accordingly. In this study, we presented some fundamental application examples with these systems. Firstly, Wnt signal pathway was demonstrated to be successfully activated in 3D bioprinted structure based on genetically engineered embryonic cells, which suggested potential in studying cell interactions and tissue remodeling [19]. Then we investigated the generation of the pluripotent embryoid body (EB) in 3D bioprinted microenvironment, where the EBs were seen with comprehensively better homogeneity, quality, and higher yield when compared to commonly used suspension and hanging-drop methods [20]. Furthermore, we used the generalizable 3D bioprinting system to tune cell behavior by introducing a peptide motif (Arginine-Glycine-Aspartic, RGD) or degradable crosslinker in the bioink formulation, both of which turned out to be helpful for cell spreading and migration [18].

This study not only adds to the technological options but also provides a general research route for microextrusion 3D bioprinting. Also, this study may serve as a guideline for people who need to develop a printing process for specific bioink.

1.3 Chapter Outline

This thesis is articulated into eight chapters (Fig. 1.1), the remaining of which is as follows:

Chapter 2 introduces the background and the recent progress of 3D bioprinting. Specifically, the state of the art of bioprinting technologies, bioinks and application areas are reviewed, along with comments on challenges and perspectives.

Chapter 3 presents the materials and methods used in this study. It comprehensively analyzes the general bioprinting process and refines key questions accordingly, which leads to the formation of general criteria and research route. Some of the general experimental methods are also enclosed.

Chapter 4 presents the 3D bioprinting of shear-thinning and self-healing bioinks [16]. Based on the analysis in Chap. 3, structure printability and stability are mainly studied with the novel supramolecular hydrogel formulations. Corresponding solutions are provided to address specific technical problems, such as oxygen inhibition and cell attachment.

Chapter 5 presents the 3D bioprinting of gelatin-based thermo-sensitive bioinks [17]. It mainly introduces a synergy optimization approach both before and after bioprinting: the rheological characterization and bioprinting outcomes (e.g., structure printability and cell viability) are systematically monitored and controlled. Some unnoted questions are revealed here, such as time-dependence of this typical bioink.

Chapter 6 presents the 3D bioprinting of non-viscous photo-crosslinkable bioinks [18]. Given the enduring limitation of bioink viscosity, the in situ crosslinking strategy

Fig. 1.1 Flow diagram of this thesis, showing the structure with all chapters
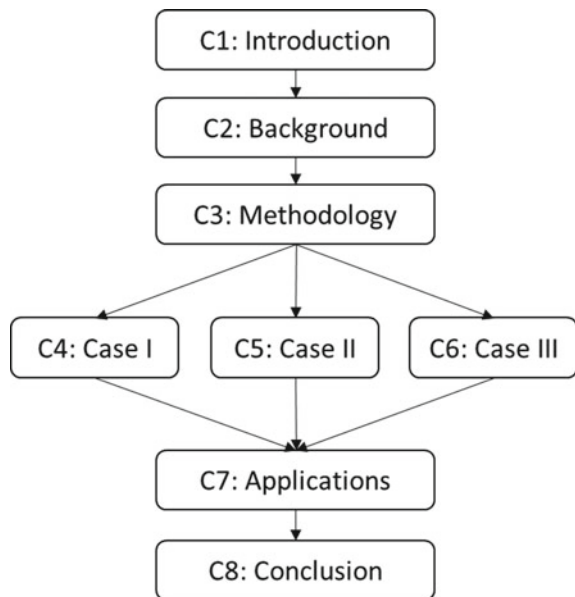
is developed to allow for versatile bioprinting of different bioinks at a low viscosity. All the established criteria are met through optimization.

Chapter 7 presents comprehensive studies on biological characterization and applications, including signal pathway activation [19], embryoid body formation [20], and cell behavior control [18].

Chapter 8 concludes this thesis and provides some suggestions regarding future work could be considered.

References

1. Murphy SV, Atala A (2014) 3D bioprinting of tissues and organs. Nat Biotechnol 32(8):773–785
2. Huang S, Liu P, Mokasdar A, Hou L (2013) Additive manufacturing and its societal impact: a literature review. Int J Adv Manuf Technol 67(5–8):1191–1203
3. Mandrycky C, Wang Z, Kim K, Kim DH (2016) 3D bioprinting for engineering complex tissues. Biotechnol Adv 34(4):422–434
4. Ryan GE, Pandit AS, Apatsidis DP (2008) Porous titanium scaffolds fabricated using a rapid prototyping and powder metallurgy technique. Biomaterials 29(27):3625–3635
5. Bose S, Vahabzadeh S, Bandyopadhyay A (2013) Bone tissue engineering using 3D printing. Mater Today 16(12):496–504
6. Moroni L, Boland T, Burdick JA, De Maria C, Derby B, Forgacs G, Groll J, Li Q, Malda J, Mironov VA, Mota C, Nakamura M, Shu W, Takeuchi S, Woodfield TBF, Xu T, Yoo JJ, Vozzi G (2018) Biofabrication: a guide to technology and terminology. Trends Biotechnol 36(4):384–402
7. Langer R, Vacanti J (1993) Tissue Engineering. Science 260(5110):920–926
8. Drury JL, Mooney DJ (2003) Hydrogels for tissue engineering: scaffold design variables and applications. Biomaterials 24(24):4337–4351
9. Griffith LG, Naughton G (2002) Tissue engineering–current challenges and expanding opportunities. Science 295(5557):1009–1014
10. Mironov V, Reis N, Derby B (2006) Review: bioprinting: a beginning. Tissue Eng 12(4):631–634
11. Mironov V, Boland T, Trusk T, Forgacs G, Markwald RR (2003) Organ printing: computer-aided jet-based 3D tissue engineering. Trends Biotechnol 21(4):157–161
12. Boland T, Mironov V, Gutowska A, Roth EA, Markwald RR (2003) Cell and organ printing 2: fusion of cell aggregates in three-dimensional gels. Anat Rec A Discov Mol Cell Evol Biol 272(2):497–502
13. Holzl K, Lin SM, Tytgat L, Van Vlierberghe S, Gu LX, Ovsianikov A (2016) Bioink properties before, during and after 3D bioprinting. Biofabrication 8(3)
14. Groll J, Boland T, Blunk T, Burdick JA, Cho DW, Dalton PD, Derby B, Forgacs G, Li Q, Mironov VA, Moroni L, Nakamura M, Shu W, Takeuchi S, Vozzi G, Woodfield TB, Xu T, Yoo JJ, Malda J (2016) Biofabrication: reappraising the definition of an evolving field. Biofabrication 8(1):013001
15. Burdick JA, Prestwich GD (2011) Hyaluronic acid hydrogels for biomedical applications. Adv Mater 23(12):H41–H56
16. Ouyang L, Highley CB, Rodell CB, Sun W, Burdick JA (2016) 3D printing of shear-thinning hyaluronic acid hydrogels with secondary cross-linking. ACS Biomater Sci Eng 2(10):1743–1751
17. Ouyang L, Yao R, Zhao Y, Sun W (2016) Effect of bioink properties on printability and cell viability for 3D bioplotting of embryonic stem cells. Biofabrication 8(3):035020

18. Ouyang L, Highley CB, Sun W, Burdick JA (2017) A generalizable strategy for the 3D bio-printing of hydrogels from nonviscous photo-crosslinkable Inks. Adv Mater 29(8)
19. Ouyang L, Yao R, Chen X, Na J, Sun W (2015) 3D printing of HEK 293FT cell-laden hydrogel into macroporous constructs with high cell viability and normal biological functions. Biofabrication 7(1):015010
20. Ouyang L, Yao R, Mao S, Chen X, Na J, Sun W (2015) Three-dimensional bioprinting of embryonic stem cells directs high-throughput and highly uniform embryoid body formation. Biofabrication 7(4):044101

Chapter 2
3D Bioprinting and Bioink: Background

This chapter generally introduces the field of 3D bioprinting, starting with the related concepts and their history. The definitions of bioprinting and bioink are clarified based on the most recent literature. The brief history of this field is reviewed, and the technology trends are presented from different angles, which all indicate a booming development. Then a comprehensive overview of state of the art is presented in terms of bioprinting technologies, bioinks, and application areas. Given the inconsistent classification method in literature, here we classify the bioprinting techniques according to the dimensions of the building blocks, which meet the essential characteristics of this bottom-to-up methodology. This chapter ends with the general challenges and some perspectives from the author.

2.1 Concepts and History

As an emerging technology, 3D bioprinting has been called numerous names, including biofabrication, cell printing, tissue/organ printing, and bioplottering [1–3]. Currently, the word "bioprinting" is more frequently used regarding the 3D printing with living cells, which is one of the most important contents of biofabrication [4]. In 2015, the Oxford Dictionary defined bioprinting as "the use of 3D printing technology with materials that incorporate viable living cells, e.g., to produce tissue for reconstructive surgery." Compared to other well-known 3D printing fields that deal with plastic, elastomer, ceramics, and metals, bioprinting is recognized by the highlight of manipulating living cells.

The concept of bioink comes along with that of bioprinting, referring to the inks used in the 3D bioprinting process. Researchers have recently suggested clarifying this concept as a cell-laden ink, to distinguish from the work of printing acellular scaffolds seeded with cells afterward [4, 5]. To enable living cell encapsulation, the bioink formulation is usually a hydrated solution with suitable physiological conditions (e.g., suitable osmotic pressure and pH). This is also correlated to the nature of the extracellular matrix (ECM), which is a 3D network of extracellular macromolecules

providing structural and biochemical support of surrounding cells [6]. These considerations have driven the use of hydrogel materials as the bioink network as they could create similar 3D microenvironment to ECM [7]. Apart from cells, different components are possible to be incorporated in bioink, including nano/microparticles, growth factors, and other biomacromolecules [7–9]. It should be noted that some novel types of bioinks have also been explored, including cell aggregates and cell-laden microgels [10, 11].

As a fabrication technology, 3D bioprinting is believed to enjoy great potential over some conventional approaches for tissue engineering (Table 2.1). Casting method is widely used to replicate a solid model with fine features, which, however, fails to engineer materials heterogeneity and complex geometry with 3D voids. The porous scaffold is treated as one of the most important elements in tissue engineering, where it provides structural support for cell growth. However, such conditions on a substrate (either flat or asperous) might not represent the microenvironment in vivo, where cells are surrounded by ECM. Moreover, the challenges in heterogeneity and cell seeding efficiency also hinder the use of porous scaffolds [14]. Based on the principle of additive manufacturing, 3D bioprinting provides a new strategy for engineering 3D tissue model by manipulating biological components spatially and temporarily. It allows for direct locating of multiple cells into a 3D matrix environment replicating a customized model.

3D bioprinting have attracted massive attention since 2003 when researchers printed living cells using an ink-jet printer for the first time [15, 18], followed by the use of other techniques such as microextrusion approach (Fig. 2.1). In 2009, the listed company, Organovo, launched the first commercial bioprinter, and IOP Publishing released a high-impact peer-review journal *Biofabrication*, focusing on bioprinting field. With the foundation of the International Society for Biofabrication (ISBF) in 2010, the community has been well organized via the ISBF annual conference and other activities (Fig. 2.1). 3D bioprinting is regarded as one of the most promising biotechnologies that would bring revolutions to human health. In the last decade, it

Table 2.1 Comparison of different biofabrication technologies. Reproduced, with permission from [12, 13]

	Casting	Porous scaffold	3D bioprinting
Materials	Natural/synthetic polymer, cell suspension	Natural/synthetic polymer, mental, ceramic	Natural/synthetic polymer, cell suspension
Resolution	>500 nm	100 nm–1000 μm	10–1000 μm
Advantages	Reusable mold, high resolution, cell-friendly	Controllable porosity, mechanical properties, materials versatility	Directly cell manipulation, complex and heterogeneous architecture
Disadvantages	Lack of porosity, heterogeneity	Low cell seeding efficiency, poor heterogeneity	Possible cell damage, limitation to materials
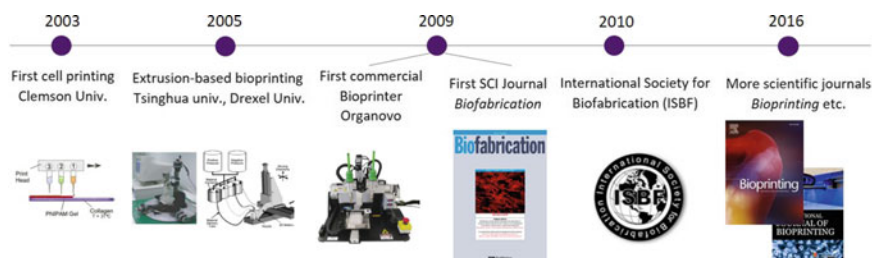
Fig. 2.1 Brief timeline of bioprinting history. Reproduced, with permission from [15–17]

has been seen with dramatic growth in both academia and industry: The numbers of bioprinting publications and newly established companies have been growing exponentially since 2003 (Fig. 2.2a, b). According to the recent Gartner curve hype cycle on 3D printing technologies, it will still take 5–10 years for 3D bioprinting to reach mainstream adoption in life science R&D (Fig. 2.2c), which also indicates the necessity of further investigation into this technology toward the translational stage.

2.2 State of the Art

2.2.1 Bioprinting Technologies

Numerous bioprinting technologies have emerged since the ink-jet printing was firstly used in cell printing. People have tried to classify them based on different criteria, such as driven force (e.g., thermal, piezoelectric, pneumatic, piston, and screw driving) and depositing approach (e.g., nozzle-based jetting or extruding, nozzle-free printing such as laser-direct-write and stereolithography) [12, 19–21]. Taking the nature of additive manufacturing, here we sort all the technologies into three categories based on the geometry of building blocks (Fig. 2.3).

2.2.1.1 Drop-Based Bioprinting (Zero-Dimensional Building Block)

Various techniques have been applied to generate cell-laden drop as a building block, including ink-jet, valve-based, acoustic, and laser-assisted approaches (Fig. 2.3a). Similar to the commercial ink-jet printer, ink-jet bioprinting patterns ink drops onto a surface according to the computer-aided design (CAD). The deposited drops are usually generated by the burst of microbubbles induced by thermal or piezoelectric effects. Valve-based bioprinting applies a mechanical or solenoid valve in the nozzle to control the generation of drops. Both ink-jet and valve-based approaches allow for the creation of submicron drops with the volume low to 1 pl per drop, which

(a)

(b)

(c)
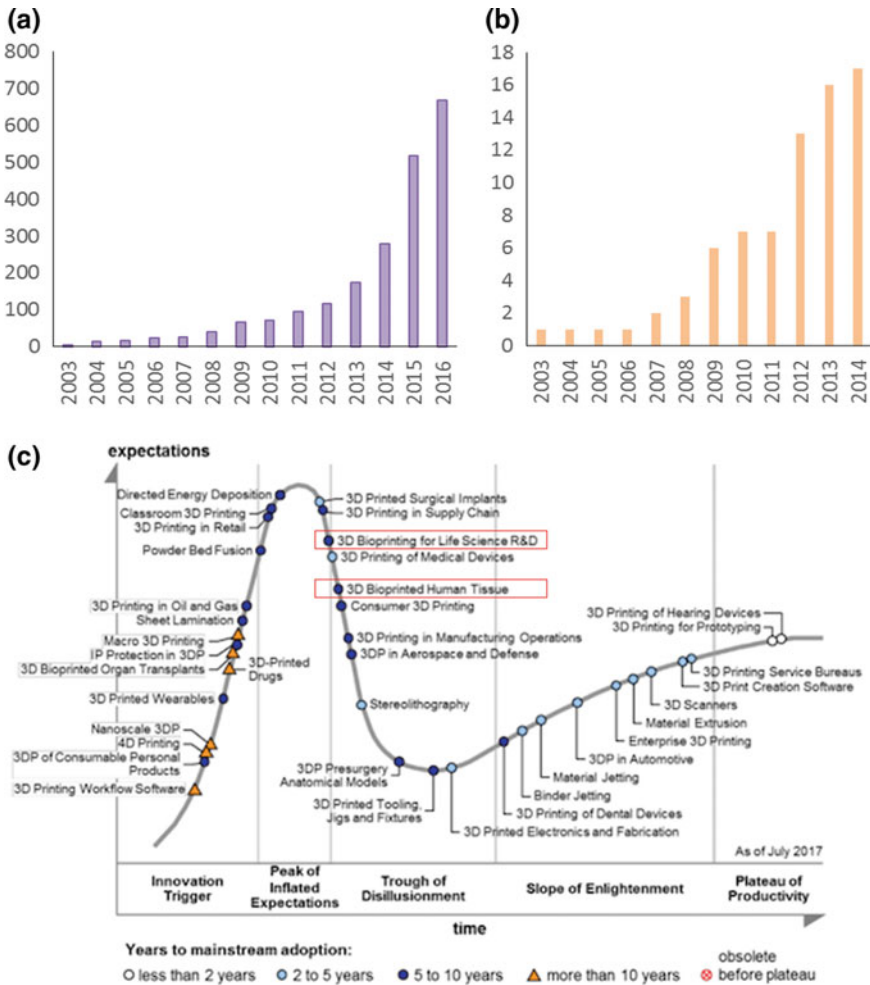
Fig. 2.2 Growth of bioprinting. Numbers of **a** publications and **b** new companies each year since 2003. **c** Gartner curve hype cycle for 3D printing technologies as of July 2017. *Data source* **a** Web of Science searched with "bioprinting" as keyword; **b** IDTechEX report "3D Bioprinting 2014–2024"; **c** Gartner, Inc

also means that only low-viscosity bioinks are applicable (<20 mPa·s) [22, 23]. In acoustic bioprinting, bioink drops are generated due to the acoustic force in the local area, where a microhole is designed to allow for drop jetting [24]. In a laser-based approach, the laser is used to either directly guide cell movement or induce a cell-laden drop generation on a reversed platform coated with cell-laden bioinks. This is possible because of the exposure of a microbubble generated by the laser energy [25]. In this case, viscous bioinks are usually used to maintain the coating layer.
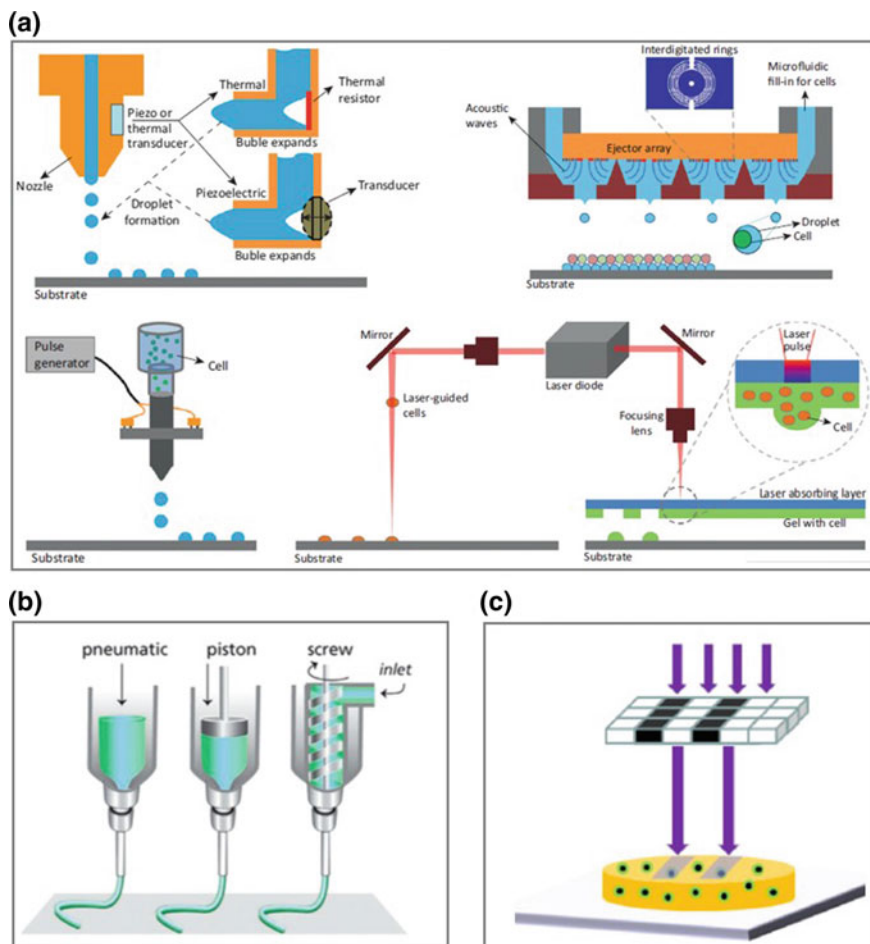
Fig. 2.3 Schematic of different types of bioprinting technologies based on the building blocks of **a** drop, **b** filament, and **c** plane. Reproduced, with permission from [6, 12, 21]

These drop-based approaches rely on the specific driving mechanisms for drop generation and deposition. Cell damages would come from the thermal effects, surface tension when bubbles break, impulse force when drops hit the bed, and water evaporation. Generally, 85% or higher cell viability could be maintained after process optimization [26, 27].

2.2.1.2 Filament-Based Bioprinting (One-Dimensional Building Block)

Microextrusion bioprinting is the main approach that uses cell-laden filaments as the building blocks. Similar to the commonly used fused deposition modeling (FDM)
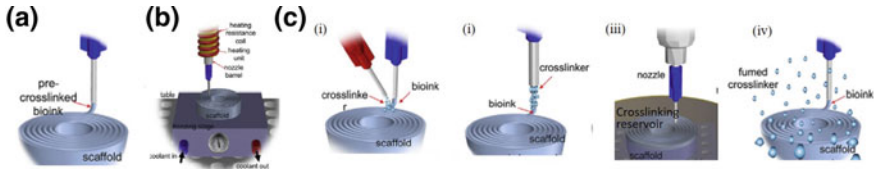
Fig. 2.4 Schematic of crosslinking strategies used in microextrusion bioprinting: **a** pre-crosslinking, **b** thermally pre- plus post-crosslinking, and **c** various post-crosslinking performed by (i) injecting crosslinker in situ, (ii) applying a core–shell needle, (iii) printing into crosslinker batch, and (iv) spraying crosslinkers. Reproduced, with permission from [28]

3D printing, raw materials are extruded into microfilaments, driven by pneumatic, piston, or screw force (Fig. 2.3b). Pneumatic system can generate a consistently stable force on the bioinks, which also means that the extrusion flux might vary with different bioinks. Thus, air pressure should be optimized whenever new bioinks are applied. Piston-driving system can preciously control the volume of bioinks being extruded and thus the printing flux. One of the disadvantages of this approach is that the extrusion force might be delayed and accumulated when printing viscous materials, which might induce unstable extrusion. Screw-driving system is suitable for dealing with highly viscous materials as it mechanically forces the inks to flow through the thread until the nozzle end. Though high force and precious control can be achieved, the screw system adds to the risk of cell contamination and damage. Currently, pneumatic and piston systems are more used in cell printing with hydrogel-based inks.

Usually, bioinks are required to maintain structural integrity after deposition to achieve 3D construction. Apart from the extrusion driving force, other printing configurations would also affect the printing outcome, such as the bioink crosslinking strategy. Corresponding to the bioink rheological properties, varied crosslinking strategies have been applied. For example, pre-crosslinking is supposed to enhance the bioink viscosity and thus to contribute to the printing fidelity (Fig. 2.4a). For some thermo-sensitive bioink formulations, comprehensive temperature control is performed pre- and post-printing to achieve optimal printing results (Fig. 2.4b) [16]. In more cases, post-crosslinking is applied to stabilize the printed filaments immediately (Fig. 2.4c). For instance, a dual-needle or core–shell needle is used to simultaneously introduce crosslinker along with bioinks (Fig. 2.4c (i, ii)) [29, 30]. Printing bioinks into crosslinker batch or spraying crosslinker on the printing area would also contribute to the fast gelation of bioinks (Fig. 2.4c (iii, iv)).

2.2.1.3 Plane-Based Bioprinting (Two-Dimensional Building Block)

Recently, digital light processing (DLP) has been introduced to fabricate 3D cell-laden constructs for tissue engineering [31]. Based on a nozzle-free optical system, DLP allows for simultaneous gelation of a 2D plane and could possibly achieve

3D construction by combining multiple planes. Basically, the curing light source is projected with a designed pattern into photo-crosslinkable bioinks to obtain a desired 2D plane. By refreshing the bioinks, several planes could be successively generated and combined. Using a 2D pattern as the building block, DLP is likely to achieve higher printing speed. However, the continuous light irradiation might induce high cell damage, and it remains a challenge for an easy switch between layers and thus for thick 3D construct fabrication.

Comprehensive comparison of three types of technologies is presented in Table 2.2. Drop-based approaches are suitable for precise 2D patterning, but fail to build up 3D constructs effectively due to the use of normal low-viscosity inks. The plane-based type represented by DLP seems to enjoy higher printing speed as the fast generation of a two-dimensional building block. Coming out very recently, this technology is not seen with much literature (8.4% fraction) and still needs to be promoted further, such as in terms of bioinks development and effective multilayer construction. Generally, the microextrusion approach is more straightforward in the applications of tissue engineering and other biomedicine fields. Moreover, most of the commercial bioprinters in the market are based on a filament building block strategy.

Table 2.2 Comparison of bioprinting technologies based on different building blocks. Reproduced, with permission from [12, 20, 28]

	Drop-based	Filament-based	Plane-based
Cost	Low (ink-jet) or high (laser-based)	Low	High
Cell viability (%)	>85	40–95	>85
Cell density	Low	Flexible	Medium
Ink materials	Low viscosity	Various hydrogels and cell aggregates	Photo-crosslinkable
Resolution	High	Medium	High
Fidelity	Poor	Good	Good
Structural complexity	Suitable for 2D pattern	Suitable for thick 3D constructs	Suitable for 2D pattern and thin 3D constructs
Applications	Tissue engineering (bone, cartilage, skin, etc.)	Tissue engineering (vascular, bone, cartilage, neural, muscle, cancer, etc.), drug delivery, organ-on-a-chip	Tissue engineering (bone, cartilage, etc.)
Literatures' fraction[a] (%)	55.4	36.2	8.4

[a]Data from Web of Science, searched with "bioprinting" and specific technology names as keywords, from 2003 to 2016

2.2.2 Bioinks

As discussed previously, bioinks usually apply hydrogel formulations as cell carriers and matrix networks. Various hydrogel materials have been used in 3D bioprinting (Table 2.3), which could be presented as follows based on the source.

Table 2.3 Comparison of different hydrogel materials used in bioprinting. Reproduced, with permission from [7, 57–59]

Materials	Type	Crosslinking	Gelation time	Applicable technologies	Literatures' fraction[a] (%)
Collagen I	Natural protein	pH, temperature	>10 min	Drop-, filament-based	24.9
Fibrin	Natural protein	Fibrinogen + thrombin	Minutes	Drop-, filament-based	8.1
Hyaluronic acid	Natural glycosaminoglycan	Light[b], enzyme	1–5 min	Filament-based	6.3
Matrigel™	Natural ECM	Temperature	>10 min	Drop-, filament-based	1.6
Gelatin	Protein hydrolysis from collagen	Temperature, light[b]	Minutes	Drop-, filament-, plane-based	18.9
Alginate	Natural polysaccharide	Ionic	Seconds	Drop-, filament-based	23.7
Chitosan	Natural polysaccharide	pH	>10 min	Filament-based	6.1
Agarose	Natural polysaccharide	Temperature	Minutes	Drop-, filament-based	4.0
PEG	Synthetic polymer	Light[b]	Minutes	Drop-, filament-, plane-based	5.6
Pluronic F-127	Synthetic polymer	Temperature	Minutes	Filament-based	0.9

[a]Web of Science, searched with "bioprinting" and name of individual materials as keywords, from 2003 to 2016
[b]With chemical modification, e.g., methacrylation

2.2.2.1 ECM-Derived Natural Hydrogel

ECM components are believed to be able to provide an ideal environment for cell migration, proliferation, differentiation, and tissue formation. The ECM-derived materials that have been used as bioinks include collagen, fibrin, hyaluronic acid, Matrigel[TM], and gelatin.

Collagen is one of the most important proteins in the body and consists of almost 50% of the total protein. For example, the integrin in collagen contains some particular site (e.g., RGD) that would modulate the interaction between cytoskeleton and matrix materials. Under a physiological condition (e.g., neutral pH, temperature around 37 °C, and suitable osmotic pressure), collagen I could form gel within 30–60 min [32]. Collagen was reported as a bioink supplement in 2004 for the first time, where bovine aortic endothelial cells were printed [33]. Since then, collagen has been greatly investigated on the bioprinting of different cell types. Currently, the main challenges for collagen-based bioinks are the enhancement of printability and mechanical properties.

Fibrin, a highly insoluble protein multimer, is a fine needle-like crystal that is primarily derived from plasma proteins. The fibrin gel can be obtained by mixing fibrinogen and thrombin at room temperature. The crosslinking process is rapid and can be completed in a few seconds to several minutes. Because of the fast and irreversible gelation process, it is difficult to print the mixed ink of fibrinogen and thrombin directly. Given this, people have introduced two strategies for the use of fibrin in bioprinting: mix separate fibrinogen and thrombin solution at the end of the nozzle and trigger gelation in situ [34, 35]; mix fibrinogen with other bioinks and treat with thrombin afterward [36]. Similar to collagen, fibrin enjoys excellent biocompatibility but presents rapid degradation and poor mechanical properties. In order to obtain a more stable printing structure, the hybrid strategy is usually used.

Hyaluronic acid (HA) is a natural glycosaminoglycan that can be found in almost all connective tissues. As a natural extracellular matrix material, HA deserves natural biocompatibility and plays a vital role in many cell activities and tissue functions, including cell migration, proliferation, differentiation, and angiogenesis [37]. Unmodified HA cannot be effectively crosslinked and is often used as an additive with other printable ink materials, including photo-crosslinked gelatin [38] and dextran [39]. Unlike collagen and fibrin, HA can be easily modified with chemical ways to achieve different biochemical or physical properties [40]. For example, methacrylated HA can undergo photo-crosslinking reaction and has been blended with gelatin for tubular structure printing [41]. The mixture of thiolated HA and polyethylene glycol is also used as a bioink formulation [42].

Matrigel[TM] is a basement membrane matrix mixture extracted from mice tumors. Its main components are laminin, type IV collagen, nestin, heparin glycoprotein, growth factors, and matrix metalloproteinases (MMPs). Matrigel[TM] can promote different cells' differentiation and tissue formation. As a thermo-sensitive formulation, Matrigel[TM] exhibits a solution at 4 °C and would form gel within tens of minutes at 37 °C, which is not reversible. Given this, the printing of Matrigel[TM]

usually requires temperature control of the nozzle and printing platform to extrude the ink smoothly and to induce gelation in time.

Gelatin is a polypeptide polymer produced via partial hydrolysis of the collagen. Gelatin exhibits good biocompatibility and strong water absorption, has no immune rejection, and can be completely degraded in vivo. Gelatin is a typical thermo-sensitive hydrogel: It can undergo a reversible sol-gel transition between high (e.g., 37 °C) and low (e.g., 4 °C) temperatures. Meanwhile, formaldehyde, glutaraldehyde, and other chemicals containing more than two active aldehyde groups can chemically crosslink gelatin to produce a stable gel network. Also, gelatin can be modified to obtain gelatin methacrylyl (GelMA), which is a photo-crosslinkable hydrogel. Based on the dual characteristics of thermo-sensitivity and photo-crosslinkability, GelMA can be used to print structurally stable construct [43]. Also, gelatin can act as sacrificial or supportive material to produce hollow tubes or suspended structures [44].

2.2.2.2   Non-ECM Natural Hydrogel

Alginate is a polysaccharide carbohydrate extracted from brown algae and has been proved to be biocompatible with no toxicity or carcinogenicity. Alginate is linearly polymerized from monomers of β-1,4-D-mannuronic acid (M) and α-1,4-L-guluronic acid (G). M and G units are linked to a block copolymer by a 1,4 glycosidic bond in a combination of MM, GG, or MG [45]. Sodium alginate is common water-soluble alginate, which gels with divalent cations, such as Ga^{2+} and Mg^{2+}. The crosslinking network mainly forms by rapid exchange of sodium ions with divalent cations (occurs in a few seconds). Based on this gelation property, a variety of crosslinking approaches have been developed for fast gelation, as shown in Fig. 2.4c: (i) Ca^{2+} can be delivered to the simultaneously injected alginate via an additional nozzle ejector [29]; (ii) a coaxial nozzle is used to simultaneously introduce alginate (core) and Ca^{2+} (shell) [46]; (iii) directly print alginate into the solution containing Ca^{2+} [30]; (iv) atomize Ca^{2+} solution to form a crosslinking environment in the printing area [47]. Although alginate is recognized with its excellent printability and mechanical properties, the biofunctionalization remains a challenge.

Chitosan is a product of chitin undergoing deacetylation and is a natural, non-toxic, biodegradable polysaccharide, being widely used in bone, cartilage, and skin tissue engineering [48]. Chitosan is generally dissolved under acidic conditions, and a gel reaction can be carried out by adjusting the pH. Due to the slow gelation (up to tens of minutes) and poor mechanical properties, chitosan is generally used in combination with other ink materials.

Agarose is a galactose polymer extracted from algae, exhibiting reversible thermo-sensitivity. The agarose formulation used in 3D bioprinting is required to have a sol temperature not higher than 37 °C to ensure the stability during cell culture [49]. The printing process generally adopts the temperature-controlled process (Fig. 2.4b). Agarose can be used as a non-adhesive ink material for forming cell clusters in three-dimensional printed structures [50].

2.2.2.3 Synthetic Hydrogel

Polyethylene glycol (PEG) is the most widely used synthetic hydrogel material. Due to its biocompatibility and low immunogenicity, PEG has been used as excipients for medical and non-pharmaceutical products. PEG can be modified to carry out corresponding physical, ionic, or covalent crosslinking. A variety of photo-crosslinkable PEG materials are engineered for bioprinting, including PEG diacrylate (PEGDA) and PEG dimethacrylate (PEGDMA) [51]. The aqueous solution of these photo-crosslinking materials usually exhibits a low viscosity, which would result in structural collapse. The hybrid bioink strategy has been applied to achieve good printing fidelity [52, 53]. Generally, as a synthetic hydrogel, PEG lacks adhesion ligand required for cell attachment and growth [54].

Pluronic F-127 (PF127) is a triblock copolymer of polyethylene glycol-polypropylene glycol-polyethylene glycol (PEG-PPO-PEG), which is approved by the U.S. Food and Drug Administration (USFDA) for use as a drug release carrier [55]. The material presents a reversible thermo-sensitivity: 40% aqueous solution exhibits a sol state at 4 °C and starts to gel above 25 °C. This means that it might apply to a reverse temperature-controlled configuration in the nozzle and platform, in comparison with gelatin. Due to the excellent printability, PF127 has been used as a sacrificial or supportive material in the construction of vascular networks [56].

2.2.3 Applications

2.2.3.1 Tissue Engineering and Regenerative Medicine

So far, very few trials have been seen with the use of bioprinted tissue products in clinic due to technical issue and the lack of FDA approval [59]. Nevertheless, a large number of studies have been carried out regarding the tissue repair and regeneration based on animal models such as rats, rabbits, dogs, pigs, and monkeys. The tissues of interest include connective, epithelial, muscle, and nerve tissues. For example, people have successfully applied different types of bioinks, such as PEGDMA, hyaluronic acid, and Matrigel^{TM}, in the repair of small bone and cartilage defects [60, 61]. However, the repair of big bones with blood vessels and articular cartilage remains a challenge. The integrated repair of bone and cartilage is another goal. Skin repair is seen with more progress because of the relatively simple structure, while the enduring challenge would be scar-free repair and integration of sweat glands. Vascular tissue engineering is believed to be one of the most critical aspects as vessels exist throughout the body [62]. Despite numerous progresses, reconstruction of the multi-scale vascular network remains a challenge. Myocardial repair also attracts much attention. Apart from various cardiac patches being used in myocardial infarction, researchers have established an accurate model of heart valves in vitro. There are few repair cases for liver and lung, the main challenges for which are the lack of cell source and long-term survival. In general, simple tissues (e.g., skin, bone,

and cartilage) have been seen with numerous progresses, while complex tissues and organs still face challenges, such as vascularization and heterogeneity.

2.2.3.2 Drug Test

With the ability to fabricate customized cell-laden pattern and construct, 3D bioprinting has been used in drug testing, where the printed biomimetic model is supposed to accelerate new drug development and thus to reduce the use of animals. In vitro liver models are in favor of drug screening, and drop-based bioprinting has been used to fabricate such models for high-throughput screening [63]. Based on the 3D microenvironment created by bioprinting, researchers have developed some convection–diffusion models for drug kinetics, which helps to understand the pharmacological and toxicological properties of 3D microtissues better. Recently, some 3D bioprinting companies have begun to offer drug screening products, such as exVi-ve3D^{TM}, a liver model from Organovo [64].

2.2.3.3 Fundamental Studies

3D bioprinting has also been used in numerous fundamental studies. For example, 3D disease models are established to better mimic the in vivo environment compared with simple 2D model. Currently, varied cancer models, including ovarian cancer [65], cervical cancer [36, 66], and breast cancer [67], have been developed mainly using microextrusion bioprinting. For example, researchers applied gelatin–alginate–fibrin hybrid bioink to fabricate cervical tumor model based on Hela cells, and they found that such 3D models performed differently from the standard 2D culture in terms of drug resistance and MMPs expression [36]. Most of the current works are in the preliminary research stage, and further progress in fabrication and characterization is needed.

2.3 Challenges and Perspectives

Despite the progress made in the last decade, there remain some challenges for bioprinting toward translational applications. These challenges come from the multi-disciplines involved in the field, including engineering, materials science, and biology (Fig. 2.5).

Fig. 2.5 Schematic of a
multi-disciplinary vision of
3D bioprinting
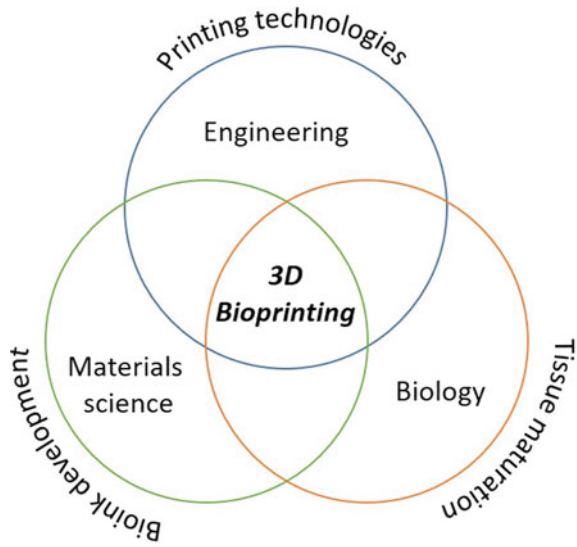
2.3.1 Bioprinting Technologies

As reviewed previously, there have been various types of bioprinting technologies being developed, and each has its own strengths. For example, ink-jet printing shares high resolution, while microextrusion printing is suitable for building up a 3D complex construct. In general, there is still demand for higher resolution and printing speed. Moreover, the next-generation bioprinting technologies should provide more features, including multi-nozzle or multi-channel printing, automatic height control, and intelligent optimization process. Engineering heterogeneous features in three-dimensional structure would be something of interest regarding the heterogeneity existed in nature. Back in 2005, researchers developed a four-nozzle microextrusion printer to deposit different materials and cells [68]. In 2016, a seven-channel nozzle was used to print multi-materials and cells, where the heterogeneous distribution of different bioinks is achieved by programming the switch among channels [69]. By combining different printing technologies, it is possible to complement each other and achieve a better outcome. The 3D bioprinting platforms that integrate a whole route, including scanning, CAD reconstruction, bioprinting, post-process, and bioreactor culture, might be another future direction.

2.3.2 Bioinks

Despite the progress on cell-encapsulation hydrogels, their use in bioprinting is still hindered due to the undesirable properties, such as low viscosity. This problem might

be addressed by introducing a novel strategy for specific bioink, such as core–shell printing of alginate-based materials. However, the generalizable bioink strategy is in demand to involve more functional biomaterials. Another challenge for bioinks would be biofunctionality. For example, to better mimic the extracellular matrix environment and to achieve similar functional and mechanical properties, bioink materials are usually required to present particular composition or gradients. Apart from the well-known bioinks containing specific components, extracellular matrix (ECM) derived from native tissue or organs has also been used in bioprinting and might be a next-generation bioink [70].

2.3.3   Tissue Maturation

Along with bioprinting technologies and bioink materials development, people have kept working on tissue maturation regarding better biofunctionality considering that most of the current bioprinting work is in a proof-of-concept stage. One of the significant aspects of tissue maturation is vascularization [62]. In native tissues, complex and multi-scale vasculatures guarantee the long-term survival of cells. Engineering vascular networks have been an enduring challenge, especially those with lumen features under 100 μm. Moreover, the match between engineering vessels and native ones in terms of mechanical properties and functionalities (e.g., permeability) remains a problem.

References

1. Mironov V, Reis N, Derby B (2006) Review: bioprinting: a beginning. Tissue Eng 12(4):631–634
2. Mironov V, Trusk T, Kasyanov V, Little S, Swaja R, Markwald R (2009) Biofabrication: a 21st century manufacturing paradigm. Biofabrication 1(2):022001
3. Mironov V, Kasyanov V, Markwald RR (2011) Organ printing: from bioprinter to organ biofabrication line. Curr Opin Biotechnol 22(5):667–673
4. Moroni L, Boland T, Burdick JA, De Maria C, Derby B, Forgacs G, Groll J, Li Q, Malda J, Mironov VA, Mota C, Nakamura M, Shu W, Takeuchi S, Woodfield TBF, Xu T, Yoo JJ, Vozzi G (2018) Biofabrication: a guide to technology and terminology. Trends Biotechnol 36(4):384–402
5. Groll J, Boland T, Blunk T, Burdick JA, Cho DW, Dalton PD, Derby B, Forgacs G, Li Q, Mironov VA, Moroni L, Nakamura M, Shu W, Takeuchi S, Vozzi G, Woodfield TB, Xu T, Yoo JJ, Malda J (2016) Biofabrication: reappraising the definition of an evolving field. Biofabrication 8(1):013001
6. Malda J, Visser J, Melchels FP, Jungst T, Hennink WE, Dhert WJ, Groll J, Hutmacher DW (2013) 25th anniversary article: engineering hydrogels for biofabrication. Adv Mater 25(36):5011–5028
7. Hospodiuk M, Dey M, Sosnoski D, Ozbolat IT (2017) The bioink: a comprehensive review on bioprintable materials. Biotechnol Adv 35(2):217–239
8. Chimene D, Lennox KK, Kaunas RR, Gaharwar AK (2016) Advanced bioinks for 3D printing: a materials science perspective. Ann Biomed Eng 44(6):2090–2102

9. Ji S, Guvendiren M (2017) Recent advances in bioink design for 3D bioprinting of tissues and organs. Front Bioeng Biotechnol 5:23

10. Mironov V, Visconti RP, Kasyanov V, Forgacs G, Drake CJ, Markwald RR (2009) Organ printing: tissue spheroids as building blocks. Biomaterials 30(12):2164–2174

11. Highley CB, Song KH, Daly AC, Burdick JA (2019) Jammed microgel inks for 3D printing applications. Adv Sci (Weinh) 6(1):1801076

12. Mandrycky C, Wang Z, Kim K, Kim DH (2016) 3D bioprinting for engineering complex tissues. Biotechnol Adv 34(4):422–434

13. Ren X, Ott HC (2014) On the road to bioartificial organs. Pflugers Arch 466(10):1847–1857

14. Hollister SJ (2005) Porous scaffold design for tissue engineering. Nat Mater 4(7):518–524

15. Boland T, Mironov V, Gutowska A, Roth EA, Markwald RR (2003) Cell and organ printing 2: fusion of cell aggregates in three-dimensional gels. Anat Rec A Discov Mol Cell Evol Biol 272(2):497–502

16. Yan Y, Wang X, Pan Y, Liu H, Cheng J, Xiong Z, Lin F, Wu R, Zhang R, Lu Q (2005) Fabrication of viable tissue-engineered constructs with 3D cell-assembly technique. Biomaterials 26(29):5864–5871

17. Khalil S, Nam J, Sun W (2005) Multi-nozzle deposition for construction of 3D biopolymer tissue scaffolds. Rapid Prototyp J 11(1):9–17

18. Mironov V, Boland T, Trusk T, Forgacs G, Markwald RR (2003) Organ printing: computer-aided jet-based 3D tissue engineering. Trends Biotechnol 21(4):157–161

19. Murphy SV, Atala A (2014) 3D bioprinting of tissues and organs. Nat Biotechnol 32(8):773–785

20. Seol YJ, Kang HW, Lee SJ, Atala A, Yoo JJ (2014) Bioprinting technology and its applications. Eur J Cardiothorac Surg 46(3):342–348

21. Tasoglu S, Demirci U (2013) Bioprinting for stem cell research. Trends Biotechnol 31(1):10–19

22. Matsusaki M, Sakaue K, Kadowaki K, Akashi M (2013) Three-dimensional human tissue chips fabricated by rapid and automatic inkjet cell printing. Adv Healthc Mater 2(4):534–539

23. Xu T, Jin J, Gregory C, Hickman JJ, Boland T (2005) Inkjet printing of viable mammalian cells. Biomaterials 26(1):93–99

24. Demirci U, Montesano G (2007) Single cell epitaxy by acoustic picoliter droplets. Lab Chip 7(9):1139–1145

25. Schiele NR, Corr DT, Huang Y, Raof NA, Xie Y, Chrisey DB (2010) Laser-based direct-write techniques for cell printing. Biofabrication 2(3):032001

26. Xu T, Zhao W, Zhu JM, Albanna MZ, Yoo JJ, Atala A (2013) Complex heterogeneous tissue constructs containing multiple cell types prepared by inkjet printing technology. Biomaterials 34(1):130–139

27. Faulkner-Jones A, Greenhough S, King JA, Gardner J, Courtney A, Shu W (2013) Development of a valve-based cell printer for the formation of human embryonic stem cell spheroid aggregates. Biofabrication 5(1):015013

28. Ozbolat IT, Hospodiuk M (2016) Current advances and future perspectives in extrusion-based bioprinting. Biomaterials 76:321–343

29. Liu YG, Hamid Q, Snyder J, Wang CY, Sun W (2016) Evaluating fabrication feasibility and biomedical application potential of in situ 3D printing technology. Rapid Prototyp J 22(6):947–955

30. Gao Q, He Y, Fu JZ, Liu A, Ma L (2015) Coaxial nozzle-assisted 3D bioprinting with built-in microchannels for nutrients delivery. Biomaterials 61:203–215

31. Hribar KC, Choi YS, Ondeck M, Engler AJ, Chen S (2014) Digital plasmonic patterning for localized tuning of hydrogel stiffness. Adv Func Mater 24(31):4922–4926

32. Park JY, Choi JC, Shim JH, Lee JS, Park H, Kim SW, Doh J, Cho DW (2014) A comparative study on collagen type I and hyaluronic acid dependent cell behavior for osteochondral tissue bioprinting. Biofabrication 6(3):035004

33. Smith CM, Stone AL, Parkhill RL, Stewart RL, Simpkins MW, Kachurin AM, Warren WL, Williams SK (2004) Three-dimensional bioassembly tool for generating viable tissue-engineered constructs. Tissue Eng 10(9–10):1566–1576

34. Xu T, Gregory CA, Molnar P, Cui X, Jalota S, Bhaduri SB, Boland T (2006) Viability and electrophysiology of neural cell structures generated by the inkjet printing method. Biomaterials 27(19):3580–3588
35. Cui X, Boland T (2009) Human microvasculature fabrication using thermal inkjet printing technology. Biomaterials 30(31):6221–6227
36. Zhao Y, Yao R, Ouyang L, Ding H, Zhang T, Zhang K, Cheng S, Sun W (2014) Three-dimensional printing of hela cells for cervical tumor model in vitro. Biofabrication 6(3):035001
37. Burdick JA, Chung C, Jia X, Randolph MA, Langer R (2005) Controlled degradation and mechanical behavior of photopolymerized hyaluronic acid networks. Biomacromol 6(1):386–391
38. Yue K, Trujillo-de Santiago G, Alvarez MM, Tamayol A, Annabi N, Khademhosseini A (2015) Synthesis, properties, and biomedical applications of gelatin methacryloyl (GelMA) hydrogels. Biomaterials 73:254–271
39. Pescosolido L, Schuurman W, Malda J, Matricardi P, Alhaique F, Coviello T, van Weeren PR, Dhert WJA, Hennink WE, Vermonden T (2011) Hyaluronic acid and dextran-based semi-IPN hydrogels as biomaterials for bioprinting. Biomacromol 12(5):1831–1838
40. Burdick JA, Prestwich GD (2011) Hyaluronic acid hydrogels for biomedical applications. Adv Mater 23(12):H41–H56
41. Skardal A, Zhang J, McCoard L, Xu X, Oottamasathien S, Prestwich GD (2010) Photocrosslinkable hyaluronan-gelatin hydrogels for two-step bioprinting. Tissue Eng Part A 16(8):2675–2685
42. Skardal A, Zhang JX, Prestwich GD (2010) Bioprinting vessel-like constructs using hyaluronan hydrogels crosslinked with tetrahedral polyethylene glycol tetracrylates. Biomaterials 31(24):6173–6181
43. Gramlich WM, Kim IL, Burdick JA (2013) Synthesis and orthogonal photopatterning of hyaluronic acid hydrogels with thiol-norbornene chemistry. Biomaterials 34(38):9803–9811
44. Lee W, Lee V, Polio S, Keegan P, Lee JH, Fischer K, Park JK, Yoo SS (2010) On-demand three-dimensional freeform fabrication of multi-layered hydrogel scaffold with fluidic channels. Biotechnol Bioeng 105(6):1178–1186
45. Rowley JA, Madlambayan G, Mooney DJ (1999) Alginate hydrogels as synthetic extracellular matrix materials. Biomaterials 20(1):45–53
46. Colosi C, Shin SR, Manoharan V, Massa S, Costantini M, Barbetta A, Dokmeci MR, Dentini M, Khademhosseini A (2016) Microfluidic bioprinting of heterogeneous 3D tissue constructs using low-viscosity bioink. Adv Mater 28(4):677–684
47. Yeo M, Lee JS, Chun W, Kim GH (2016) An innovative collagen-based cell-printing method for obtaining human adipose stem cell-laden structures consisting of core-sheath structures for tissue engineering. Biomacromol 17(4):1365–1375
48. Ye K, Felimban R, Traianedes K, Moulton SE, Wallace GG, Chung J, Quigley A, Choong PF, Myers DE (2014) Chondrogenesis of infrapatellar fat pad derived adipose stem cells in 3D printed chitosan scaffold. PLoS ONE 9(6):e99410
49. Serwer P (1987) Agarose gel electrophoresis of bacteriophages and related particles. J Chromatogr 418:345–357
50. Almeida CR, Serra T, Oliveira MI, Planell JA, Barbosa MA, Navarro M (2014) Impact of 3-D printed PLA- and chitosan-based scaffolds on human monocyte/macrophage responses: unraveling the effect of 3-D structures on inflammation. Acta Biomater 10(2):613–622
51. Pereira RF, Bártolo PJ (2015) 3D bioprinting of photocrosslinkable hydrogel constructs. J Appl Polym Sci 132(48):n/a–n/a
52. Censi R, Schuurman W, Malda J, di Dato G, Burgisser PE, Dhert WJA, van Nostrum CF, di Martino P, Vermonden T, Hennink WE (2011) A printable photopolymerizable thermosensitive p(HPMAm-lactate)-PEG hydrogel for tissue engineering. Adv Func Mater 21(10):1833–1842
53. Bertassoni LE, Cardoso JC, Manoharan V, Cristino AL, Bhise NS, Araujo WA, Zorlutuna P, Vrana NE, Ghaemmaghami AM, Dokmeci MR, Khademhosseini A (2014) Direct-write bioprinting of cell-laden methacrylated gelatin hydrogels. Biofabrication 6(2):024105
54. Zhang M, Desai T, Ferrari M (1998) Proteins and cells on PEG immobilized silicon surfaces. Biomaterials 19(10):953–960

55. Chang CC, Boland ED, Williams SK, Hoying JB (2011) Direct-write bioprinting three-dimensional biohybrid systems for future regenerative therapies. J Biomed Mater Res B Appl Biomater 98(1):160–170

56. Hardin JO, Ober TJ, Valentine AD, Lewis JA (2015) Microfluidic printheads for multimaterial 3D printing of viscoelastic inks. Adv Mater 27(21):3279–3284

57. Skardal A, Atala A (2015) Biomaterials for integration with 3-D bioprinting. Ann Biomed Eng 43(3):730–746

58. Jose RR, Rodriguez MJ, Dixon TA, Omenetto F, Kaplan DL (2016) Evolution of bioinks and additive manufacturing technologies for 3D bioprinting. ACS Biomater Sci Eng 2(10):1662–1678

59. Ozbolat IT, Peng W, Ozbolat V (2016) Application areas of 3D bioprinting. Drug Discov Today 21(8):1257–1271

60. Cui XF, Gao GF, Yonezawa T, Dai GH (2014) Human cartilage tissue fabrication using three-dimensional inkjet printing technology. J Vis Exp (JoVE) 88:e51294

61. Gao G, Schilling AF, Yonezawa T, Wang J, Dai G, Cui X (2014) Bioactive nanoparticles stimulate bone tissue formation in bioprinted three-dimensional scaffold and human mesenchymal stem cells. Biotechnol J 9(10):1304–1311

62. Novosel EC, Kleinhans C, Kluger PJ (2011) Vascularization is the key challenge in tissue engineering. Adv Drug Deliv Rev 63(4–5):300–311

63. Chang R, Nam J, Sun W (2008) Direct cell writing of 3D microorgan for in vitro pharmacokinetic model. Tissue Eng Part C Methods 14(2):157–166

64. Vaidya M (2015) Startups tout commercially 3D-printed tissue for drug screening. Nat Med 21(1):2

65. Xu F, Celli J, Rizvi I, Moon S, Hasan T, Demirci U (2011) A three-dimensional in vitro ovarian cancer coculture model using a high-throughput cell patterning platform. Biotechnol J 6(2):204–212

66. Huang TQ, Qu X, Liu J, Chen S (2014) 3D printing of biomimetic microstructures for cancer cell migration. Biomed Microdevices 16(1):127–132

67. King SM, Presnell SC, Nguyen DG (2014) Development of 3D bioprinted human breast cancer for in vitro drug screening. Can Res 74(19):2034

68. Darling A, Shor L, Khalil S, Mondrinos M, Lelkes P, Guceri S, Sun W (2005) Multi-material scaffolds for tissue engineering. Macromol Symp 227:345–355

69. Liu W, Zhang YS, Heinrich MA, De Ferrari F, Jang HL, Bakht SM, Alvarez MM, Yang J, Li YC, Trujillo-de Santiago G, Miri AK, Zhu K, Khoshakhlagh P, Prakash G, Cheng H, Guan X, Zhong Z, Ju J, Zhu GH, Jin X, Shin SR, Dokmeci MR, Khademhosseini A (2016) Rapid continuous multimaterial extrusion bioprinting. Adv Mater 29(3):201604630

70. Pati F, Jang J, Ha DH, Won Kim S, Rhie JW, Shim JH, Kim DH, Cho DW (2014) Printing three-dimensional tissue analogues with decellularized extracellular matrix bioink. Nat Commun 5:3935

Chapter 3
Materials and Methods

The goal of this chapter is to better understand the bioprinting process by theoretically analyzing the correlated topics and questions. It summarizes the general criteria and research route for bioprinting. Despite numerous microextrusion bioprinting strategies developed, very little knowledge has been defined or discovered in terms of the nature of bioprinting. We believe that these strategies share some common features (e.g., one-dimensional filament as building block) that would lead to a better understanding and exploitation of this technology. This chapter will first analyze the general process of microextrusion bioprinting step by step and extract critical questions from each step. The general criteria will be subsequently concluded in terms of structural fidelity and cell protection. Based on the bioink crosslinking mechanisms, such criteria will be used to guide the design of the bioprinting process, covering the filament formation, deposition, and structure stabilization. Overall, a research route will be presented, which will be used in the subsequent case studies. Moreover, this chapter will introduce some general methods used in the study regarding rheology, 3D printability, shear stress determination, and cellular characterization.

3.1 Process Analysis and Questions Refining

3D bioprinting is an additive manufacturing technology that processes cell-laden bioinks into 3D architecture on demand for applications in biomedicine and life science [1]. To better understand this bottom-up fabrication methodology, here we breakdown the typical microextrusion bioprinting process and analyze it stepwise (Fig. 3.1). Basically, the cell-laden formulations will experience three stages, namely bioink solution, gel filament, and 3D construct. As the raw materials, bioinks usually present in sol status inside the cartridge. The gelation properties of the biomacromolecules in the bioinks physically determine the processing, while their biocompatibility and biofunctionality will ultimately contribute to the final output in use. As the building block for 3D construction, gel filament is usually generated between the printing nozzle and platform. The associated features include filament size, geometry,
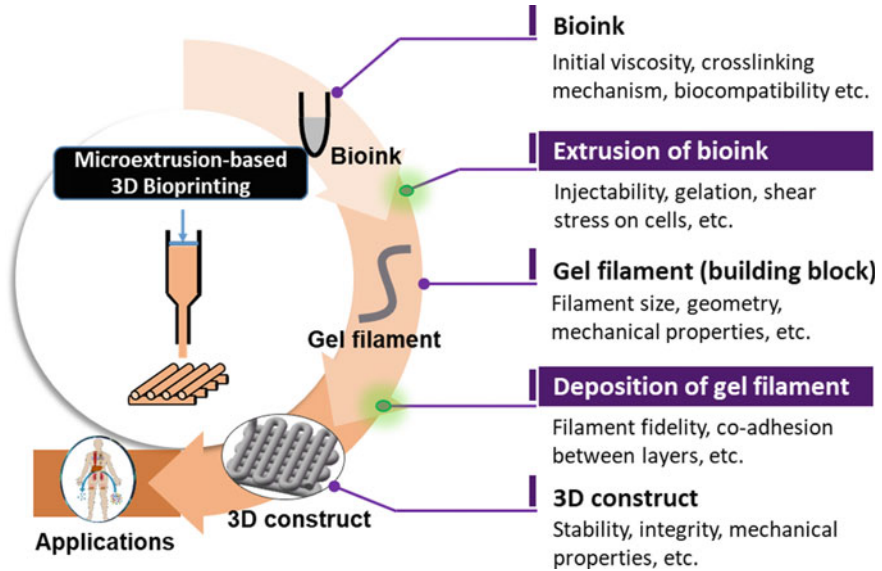
Fig. 3.1 Step-by-step analysis of the 3D bioprinting process, indicating the typical contents at each stage

fidelity, and mechanical properties among others. 3D cell-laden construct, generated from the layer-by-layer deposition of gel filaments, serves as the final product in the bioprinting process, and its integrity, stability, and mechanics are usually discussed.

To achieve a successful bioprinting practice, the transitions between these stages represent the key challenges to be addressed, which are: (i) gel filament formation from bioink extrusion and (ii) gel filament deposition into the 3D construct.

Filament generation lays the basis for 3D construction, and it usually happens along with the bioink sol–gel transition, during which bioinks are extruded from a expand space (printing cartridge) through a narrow space (printing needle) and finally to a flat surface (printing platform). To achieve this, intrinsic or external stimuli are usually applied to induce this transition corresponding to the gelation mechanism, which is termed as primary crosslinking in this thesis. The terms used in the titles of Chaps. 4–6 also indicate the primary crosslinking types that are associated with the filament generation. This process will be entirely studied because of its fundamental importance for printability and potential effect on cells (e.g., cell damages are believed to be caused by shear forces during extrusion [2]).

3D constructs are built up by manipulating generated filaments in a layer-by-layer fashion. Based on the CAD model and 3D printer system, the relative movement in $X–Y$ panel between printing nozzle and platform would result in 2D pattern deposition in each layer, while the relative movement in Z-axis would switch between layers. This calls for excellent coordination between software and hardware (e.g., speed match between extrusion and $X–Y$ movement) and suitable filament properties (e.g., strong enough to support upper layer deposition, co-adhesion between

filaments). To achieve so, additional gelation might be introduced to the constructs, which will be termed as secondary crosslinking in this thesis.

3.2 General Criteria for Bioinks and 3D Bioprinting Process

Based on the analysis above, we could summarize the general criteria for a bioprinting practice in terms of 3D structure and cells. These criteria would, in turn, guide the development and optimization of bioinks and bioprinting process (Fig. 3.2a). The 3D structure represents the processing ability and highlights the feature of this fabrication methodology, which could be characterized with 3D printability. Beyond merely showing the fabricated structure, investigators have recently applied different methods to determine and quantify printability [3–5]. Here, we will introduce some simple approaches to better characterize the printability (see 3.4). Basically, the general criteria for an excellent printability include the injectability of bioinks, filament generation, structure deposition, and stability (Fig. 3.2b).

One of the most significant differences of 3D bioprinting from other 3DP technologies (e.g., those for processing metal and plastics) is the involvement of living cells, which adds to the challenges in fabrication. It is usually required to protect the embedded cells as much as possible, which means the cell damage should be minimized from various factors, including the shear force, unadvisable temperature, and moisture (Fig. 3.2c). Cell viability (the proportion of living cells among total cells) is the primary indicator for cell damage, in addition to further characterization, such as cell proliferation, migration, and specific gene expression. Here, we specify some significant criteria as follows.
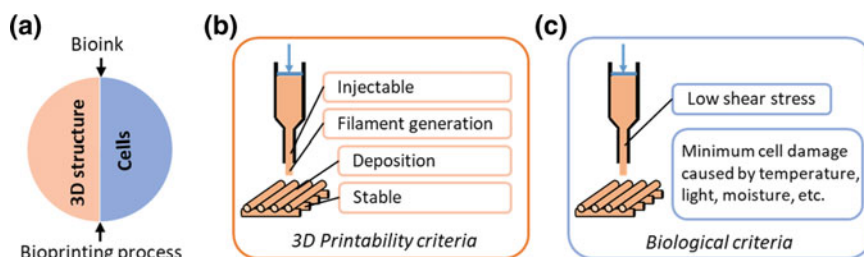
Fig. 3.2 **a** Schematic of the synergistic effects of bioink and bioprinting process on 3D structure and cells. **b** General criteria for 3D printability. **c** General criteria for biological activities

3.2.1   Bioink Injectability and Smooth Extrusion

Different from nozzle-free bioprinting technologies (e.g., stereolithography, laser-direct-writing), the microextrusion approach relies on a microneedle to deliver bioinks and perform structure deposition, where the injectability of bioinks plays a crucial role. Injectable formulations have been widely studied in the field of biomaterials, targeting at non-invasive therapeutics, including cargos (e.g., cells, drugs, growth factors) delivery and tissue engineering (e.g., cardiac regeneration) [6]. Such injectable systems might be transferrable to bioprinting process.

Beyond the typical injectable requirement, smooth extrusion is also required for the highly programmed bioprinting process as it affects the matching between bioinks delivery and 3D movement and thus affects the quality of the final products in terms of structural integrity and fidelity. Basically, low viscosity and homogeneous biomacromolecules would contribute to easy and smooth extrusion. For example, pre-crosslinking might result in disordered extrusion because of the partial gelation. Bioinks should be confirmed with the injectability and smooth extrusion before being applied in 3D bioprinting. An easy way to do so is to monitor the extrusion force during continuous printing (see 3.4.5), where a consistent force is desired.

3.2.2   Gel Filament Generation

During extrusion, bioink is affected by surface tension and inner cohesion at the nozzle tip. The former forces the bioink expand and form a sphere at the nozzle tip, while the latter makes bioink form continues filament with the help of gravity. It is commonly agreed that viscous bioink (e.g., using higher polymer concentration or adding additional components) would help to break surface tension and thus to enhance gel filament formation [7]. However, this might limit the use of numerous low-viscosity hydrogels and cause possible cell damage from high shear stress during extrusion [8]. In this thesis, we will discuss the determination of shear force and its effect on cells (see 3.4.4) and will introduce a generalizable strategy to address the viscosity issue (Chap. 6).

The generated filaments are usually characterized with their geometry, which ideally presents as a uniform fiber with a circular cross section. Because of the soft nature of hydrogel and possible less-gelation, the actual filaments might lose the original geometry and turn to be flat when being deposited on the printing platform. By calculating the volume of filament together with its length and top-view diameter, we can determine the circularity of the cross section and thus to preliminarily assess the printability of the specific bioink (Chap. 4). Normally, if one observes a gel filament hanging on the nozzle tip during extrusion, it probably indicates a good printability. In some cases, although the bioink could not deliver perfect filament on the nozzle tip, the friction and interaction between filaments and the printing

surface would help to maintain the filament pattern. Thus, characterizing the printed structures would directly reveal the printability as discussed in Sect. 3.4.3.

3.2.3 Structural Integrity

Structure integrity includes the contents of co-adhesion, fabrication fidelity, and further stability. Co-adhesion between layers is of great importance for additive manufacturing during the layer-by-layer fabrication. Suitable filaments should not be too rigid and should allow for binding with previous filaments through self-assembly or other inter-crosslinking. A simple way to assess the co-adhesion is to immerse the printed structure in incubation buffer to see if layers would detach. Furthermore, tensile tests could be applied to determine the binding force in the Z-axis.

Fabrication fidelity represents the replication of the designed model and is closely linked to printing resolution and processing control. For example, the typically occurred issue with inertial dripping at the end point of an extrusion action might affect the next move and thus affect the overall fidelity.

Structure stability under physiological conditions ensures the maintenance of the 3D cellular microenvironment. The degradation properties of the fabricated structure are usually desired to match with the cell activities and tissue remodeling process (e.g., cells would secrete extracellular matrix). Some reversible gelation (e.g., thermal gelation of gelatin) would be quickly destroyed during incubation, which might call for secondary crosslinking to stabilize the structure and adjust the degradation.

3.2.4 Cell Damage Control

The previous criteria are more about physical considerations, mainly regarding the 3D printability, while biological requirements might be more diverse ranging throughout the whole process. For example, sterilization needs to be done with any apparatus and reagents that would directly or indirectly contact cells, which include bioinks, bioink cartridge, needle, and printing platform. Some commercial bioprinting systems are highly incorporated with fume unit and UV lamp, which can provide a professional sterile environment. Another primary aspect is the biocompatibility of the bioink formulations being used to encapsulate cells. All the reagents (hydrogel polymer, initiator, crosslinker, and other supplements) in the bioink should be proved to be non-toxic with the desired dose in use. Beyond this, further biofunctionality might be expected to achieve a specific goal (e.g., angiogenesis and mineralization).

For microextrusion bioprinting, the shear force is believed to be one of the main external reasons for cell damage [2, 9]. Specifically, high viscosity, high extrusion ratio, and small needle would all result in high shear force applied to cells, which will be further discussed in Sect. 3.4.4. Apart from this, some other physicochemical stimuli also deserve concerns, such as cell apoptosis caused by long-term starv-

ing out of suitable temperature and moisture, and hydrogel dehydration. In some cases, secondary crosslinking might introduce additional hazards post-printing. For example, high ion concentration might result in undesired osmotic pressure for ionic crosslinking, while photo-crosslinking sometimes introduces free radicals, which would induce toxicity with a certain amount.

## 3.3 General Design of Bioinks and 3D Bioprinting Process

3.3.1 Bioinks and the Crosslinking Mechanism

Among the current bioink materials, collagen, gelatin, and alginate seem to be the most widely used ones (Fig. 3.3). Derived from collagen, gelatin enjoys the natural biocompatibility as a semi-protein and undergoes significant thermal responsibility for hydrogel formation [10]. As a natural biomaterial, alginate has been widely used in biomedical application because of its easy crosslinking with bivalent cation and good biocompatibility [11]. In this thesis, these two classic hydrogel materials will be both considered as bioink candidates. As discussed in Chap. 2, extracellular matrix components, such as hyaluronic acid (HA), fibrin, and collagen, might be more promising as cell-encapsulation formulation when compared with non-animal source biomaterials. For example, HA is found to be important in regulating many cellular behaviors and tissue functions, such as cell migration, proliferation, differentiation, and angiogenesis [12]. Moreover, different modifications and functionalization could be made based on the HA backbone [12]. Thus, HA is chosen as another bioink candidate in this thesis. Moreover, poly (ethylene glycol) (PEG)-based materials will be applied as the synthetic representative considering its wide use in cell-encapsulation studies.

From the aspect of materials processing, the behind crosslinking mechanism and gelation properties might matter more than the belonging type of specific bioink. Hydrogels can be formed with either physical or chemical crosslinking; the latter usually generates covalent bonds while the former does not. Here, we choose four representative types of crosslinking mechanisms, including supramolecular

Fig. 3.3 Typically used hydrogel materials in 3D bioprinting. The area of the orange circle represents the share of the indicated material, and the materials highlighted with underlines will be mainly studied in this thesis
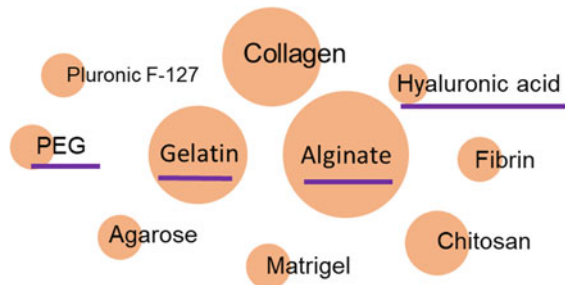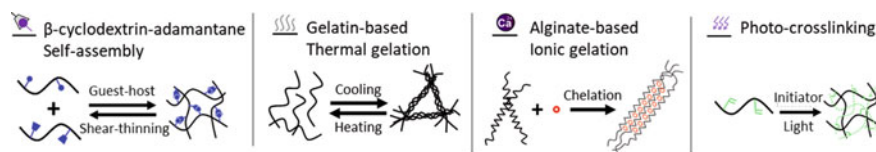
Fig. 3.4 Schematic of different crosslinking mechanisms used in this thesis

self-assembly, thermal gelation, ionic gelation, and covalently photo-crosslinking (Fig. 3.4). Supramolecular self-assembly means that molecules are held together with non-covalent bonds, such as guest–host bonding with β-cyclodextrin and adamantane groups. This guest–host chemistry will be applied to HA to form a shear-thinning formulation to meet the requirements of injectability and filament generation (Chap. 4). The thermal gelation of gelatin is due on the helix micelle formation under low temperature, which is reversible when heating up. The ionic gelation of alginate relies on the quick chelation of bivalent cation with alginate, which results in "egg" structure. As a typical covalent crosslinking, photo-polymerization can be triggered in a non-contact way and will be used in this thesis with different types of reactions. Specifically, acrylate- or methacrylate-based free radical polymerization and thiol-ene click polymerization will be investigated.

3.3.2 3D Model Design

As a primary element for tissue engineering, 3D scaffold basically provides a spatial environment for cell growth and further tissue formation. Porous scaffolds, especially those with hierarchical porosity, are of great interest considering the importance of transfer of nutrient, waste, and oxygen. With the ability to manipulate components spatially in a "bottom-up" way, 3DP serves as a perfect technology to fabricate such scaffolds.

A 3D lattice model is typically applied as an example of a structure with well-defined porosity, where filaments are deposited in parallel with a certain distance and shift with 90° between layers (Fig. 3.5a). In 3D cell-encapsulation culture, such porous structure would allow for throughout perfusion of medium (Fig. 3.5a), while bulk structure might present limited access to medium only in the near-surface area (Fig. 3.5b). It has been proved that the depth for nutrient and oxygen diffusion in hydrogel is within hundreds of micrometers, beyond which cells would be exposed to compromised microenvironments [13]. This dramatically limits the scale-up of a bulk construct with the risks of less homogeneity and controllability. From the aspect of 3D construction, the lattice model would also be representative. Placing independent filaments with a certain distance would help to assess the generation and maintenance of filaments, while the 0°–90° orientation shift would indicate the supporting between layers. Given this, we will generally use this classic model to demonstrate 3D printability in the following chapters.
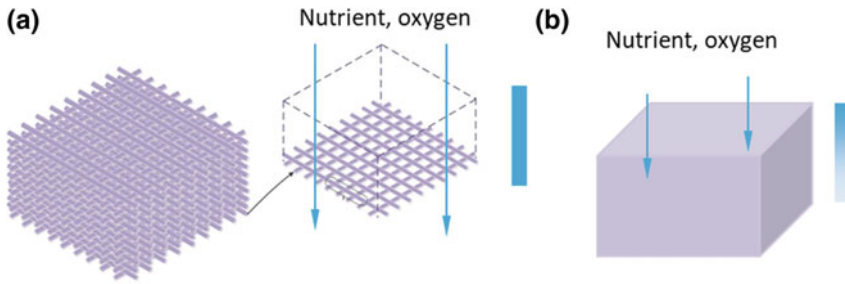
Fig. 3.5 Schematic of the nutrient and oxygen transfer in **a** porous lattice structure and **b** bulk structure. **a** Reproduced, with permission from [14]

Apart from this lattice design, other representative geometries will be presented as well, including letter pattern, cylinder, 3D pyramid, and tube and nose-like structure, which will show the processing capability from different aspects. For example, the building up of a self-standing tubular structure might test the ability of the system to withstand the possible instability and collapse considering the soft nature of hydrogel materials.

3.3.3 Process Design

Based on a well-established 3D bioprinting facility, the content of process design is more about the spatial and temporal design of gelation reactions, initially targeting as good 3D printability. Figure 3.6a shows the possible regions where gelation stimuli could be applied: (I) nozzle cartridge before squeezing happens, (II) nozzle needle where bioinks are shaped, (III) space from needle tip to printing platform, and (IV) printing platform after deposition.

Figure 3.6b shows the basic workflow about introducing gelation stimuli. The primary crosslinking, which helps to maintain filament generation, can occur in
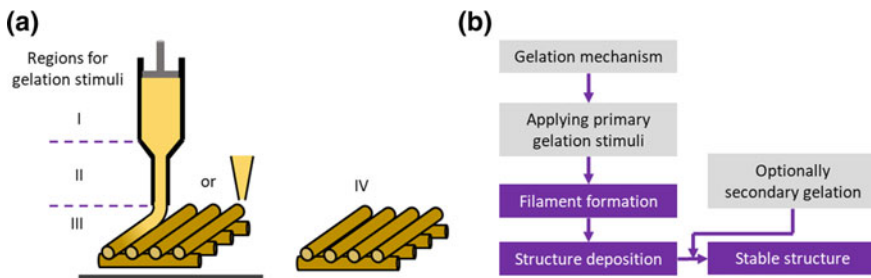
Fig. 3.6 General process design. **a** Schematic of the printing process indicating the regions where gelation stimuli can be applied. **b** Workflow based on bioink crosslinking
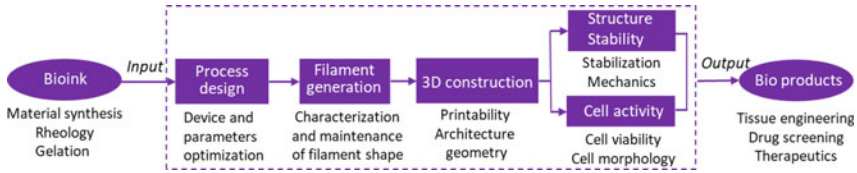
Fig. 3.7 Flowchart showing the general research route from bioink to final bioproducts

regions I–III, while optional secondary crosslinking, focusing on structure stability, usually happens in regions III or IV. Taking the FDM process as an example, raw plastics are melted in region I and start to solidify in region II and end up with full solidification in region III. In this thesis, we will assign corresponding stimuli (e.g., temperature, light) to these regions based on specific bioink.

3.4   Research Methodology

3.4.1   General Research Route

Based on the analysis above, we create a general research route as shown in Fig. 3.7, where cell-laden bioink acts as input and 3D bioproducts act as output. The in-between process contains the typical contents of a bioprinting practice, including process design, filament generation, 3D construction, structural integrity, and cell activity. The representative aspects in terms of characterization and optimization are also indicated in the chart. We will apply this route to the three cases in the following chapters with detailed discussion for each section. Some representative experimental methods are indicated as follows.

3.4.2   Rheological Characterization

To understand the rheological properties of bioink and thus to guide bioink preparation and bioprinting process optimization, continuous flow and oscillatory tests are carried out using two high-performance rheometers, Physica MCR302 (Anton Parr) and AR2000 (TA Instruments). The former rheometer allows for a wide range of temperature sweep with quick-response heating and cooling units. It is used to characterize thermo-sensitive bioinks (Chap. 5) with a cone geometry (diameter 25 mm and angle 120 min). The latter rheometer is equipped with an adaptable testing platform, which could be replaced by a transparent one for the introduction of light. This will be used to measure photo-crosslinkable formulations in situ (Chaps. 4 and 6) together with a cone geometry (diameter 20 mm and angle 59 min 42 s).

The applied continuous flow test is performed with controlled shear rate ($\dot{\gamma}$, s^{-1}), from which the viscosity (η, Pa s) curve against shear rate, also termed as flow curve, is usually obtained. The viscosity of Newtonian fluid keeps constant with shear rate, while non-Newtonian fluid (e.g., pseudoplastic or dilatant) presents varying viscosity under different shear rate. Oscillatory test allows for more variable settings, such as strain (%) and frequency (Hz). Storage (G', Pa) and loss (G'', Pa) moduli are typically obtained from this test to characterize the viscoelasticity of the tested sample. We mainly use the oscillatory test to determine the gelation status of bioink, where the dramatic increase of G' usually means the happening of gelation. More specifically, we define the point where G' surpasses G'' as the gelation point, which means a sol status when $G' < G''$ and a gel status when $G' > G''$. Unless otherwise stated, G' and G'' are presented as closed and open points, respectively, in the same plot. The major variables are set as follows with further details in the corresponding text, shear rate (1–100 s^{-1}), oscillatory strain (0.01–500%), frequency (0.01–100 Hz), and temperature (4–37 °C). Unless otherwise stated, viscosity values are measured by using flow test with a shear rate of 10 s^{-1}. For in situ measurement of photo-crosslinkable formulations, UV lamp (320–390 nm, Omnicure S1000) and visible lamp (400–500 nm, Omnicure S1500) are used.

3.4.3   3D Printability Characterization

As analyzed previously, one can preliminarily tell the printability from bioink extrusion status, where continuous uniform filaments are desired. Different from standard filaments with a circular cross section, printed filaments might be fatted and lose the shape because of gravity during deposition on printing platform. One can easily analyze the size of printed filaments from top view under a microscope, while it might be challenging to tell the features on the side. By assigning the compromised filament with an oval cross section, we can calculate the ratio of the major and minor axes and use it to determine how well it maintain the original shape, or how much it collapses. The detailed methods and results can be found in Chap. 5.

Further characterization can be done with 3D-printed construct regarding the printability. There are three types of gelation status for bioinks during extrusion, the less-, proper-, and over-gelation (Fig. 3.8), which will result in different extrusion status and 3D structure outputs. With the less-gelation bioink, no proper filaments can be formed, and there is a big chance for the printed lattice structure to be fused together. With the proper-gelation, standard filament and lattice structure can be delivered, while over-gelation might result in snatchy filament and ugly construct. To better distinguish these statuses and determine printability, we could analyze the geometry of the lattice pore, which is supposed to be a square for ideal printing. The pore under less-gelation would turn round because of the fusion between filaments while that under over-gelation would be irregular-shaped (Fig. 3.8). Given this, we could characterize the concavity or convexity of the pore based on circularity:
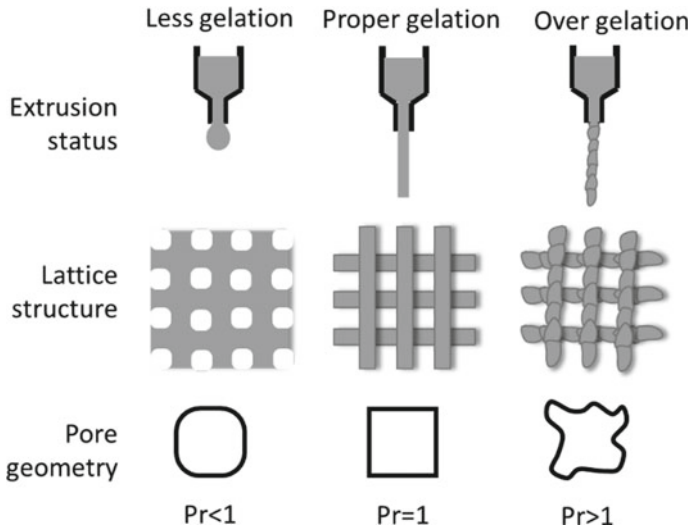
Fig. 3.8 Schematic of different gelation status during extrusion and the analysis of lattice structure and the associated pore geometry. Reproduced, with permission from [15]

$$C = \frac{4\pi A}{L^2} \tag{3.1}$$

where C is the circularity, A is the area, and L is the perimeter of the pore. The C value is 1 for a circle and is $\pi/4$ for a square. Based on this, here we propose to define a printability variable, Pr, as follows:

$$Pr = \frac{\pi}{4C} = \frac{L^2}{16A} \tag{3.2}$$

In this case, the standard printability value would be 1, while Pr > 1 indicates over-gelation and Pr < 1 indicates less-gelation. This approach can help us to semi-quantify the printability and guide the optimization of the printing parameters. Further information about this method can be found in Chap. 5.

3.4.4 Shear Stress Determination

Shear stress is believed to be a major cause for cell damage during microextrusion bioprinting. In this thesis, we presented the relationship between cell viability and shear force induced in the needle [16]. For non-Newtonian fluid, which applies to most of the hydrogel-based bioinks, shear stress (τ) can be expressed as

$$\tau = \eta\dot{\gamma} = K\dot{\gamma}^n \tag{3.3}$$

Fig. 3.9 Distribution of velocity and shear stress in laminar flow. Reproduced, with permission from [15]
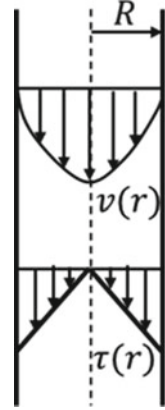
where η is the viscosity, $\dot{\gamma}$ is shear rate, K is a coefficient related by materials concentration and temperature, while n is flow coefficient.

To determine $\dot{\gamma}$, we assume the bioink extrusion to be laminar flow in the needle (Fig. 3.9). The flow velocity profile would be parabola-shaped, while the shear stress profile is triangle-shaped with zero stress in the center. Shear rate can be defined as

$$\dot{\gamma}(r) = \frac{\mathrm{d}v(r)}{\mathrm{d}r} = \frac{2v_{\max}}{R^2} \cdot r \tag{3.4}$$

where $v_{\max}$ is the maximum velocity in the axis, r is the distance from the axis, and R is the inner diameter of the needle. For microextrusion bioprinting, extrusion flux Q can be expressed as

$$Q = \pi R^2 v_{\mathrm{avg}} = \frac{\pi R^2 v_{\max}}{2} \tag{3.5}$$

where v_{avg} is the average velocity of bioink in the needle. Based on Eqs. (3.4) and (3.5), the shear rate can be expressed as

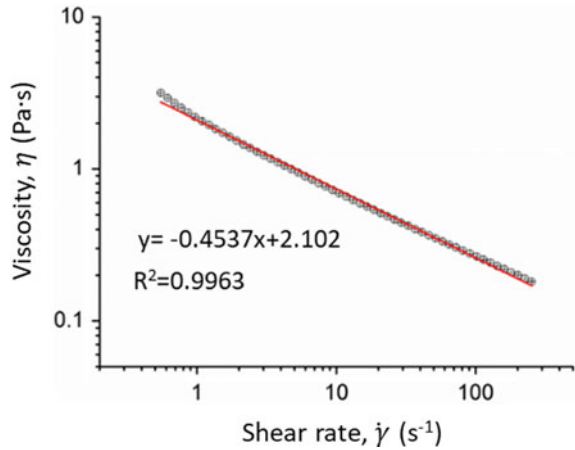$$\dot{\gamma}(r) = \frac{4Q}{\pi R^4} \cdot r \tag{3.6}$$

For better demonstration, we use the maximum shear rate ($\dot{\gamma}_{\max}$) as representative and it is expressed as

$$\dot{\gamma}_{\max} = \frac{4Q}{\pi R^3} \tag{3.7}$$

Furthermore, Eq. (3.3) is transferred to the following equation,

$$\eta = K\dot{\gamma}^{n-1} \tag{3.8}$$

Fig. 3.10 Linear fitting of a typical flow curve from rheological characterization. Reproduced, with permission from [15]

which can be further changed to

$$\lg(\eta) = \lg(K) + (n-1)\lg(\dot{\gamma}) \tag{3.9}$$

This means a linear relationship between viscosity and shear rate in logarithmic coordinates (flow curve) with $\lg(K)$ as Y-intercept and $(n-1)$ as the slope. Figure 3.10 shows a representative flow curve of 5% gelatin plus 1% alginate (testing temperature is 27.5 °C) mixture with good linearity ($R^2 = 0.9963$). Thus, K and n can be determined in this specific example. Based on the determined $\dot{\gamma}_{max}$, K and n, we can calculate the maximum shear stress by using Eq. (3.3).

3.4.5 Other Experimental Methods

3.4.5.1 Cell Culture

All the cells used in this thesis are maintained at 37 °C and 5% CO_2 with the corresponding medium changed every two days. When cells were 80–90% confluent, 0.25% trypsin solution was added (0.05–0.1 ml/cm^2) for 2–5 min for cell detachment, followed by quenching with the same volume of the corresponding culture medium. After centrifugation (800 rpm, 5 min), cell pellets were resuspended to the desired concentration for passaging or use. The regular maintenance of mouse embryonic stem cells (mESCs) applies the above protocol for adherent culture, where the cell culture dish was particularly coated with 0.1 wt% gelatin at least two hours in advance to enhance cell attachment. For suspension culture, 0.2–0.5×10^6/ml of mESCs were seeded in a non-treated culture dish, and low-speed centrifugation was used for medium change and passaging. In hanging-drop culture, 20 µl cell suspension at a density of 0.01×10^6/ml was dripped in an array on the inner surface of

the petri dish lid, which was carefully placed back to the dish containing phosphate buffered saline (PBS) for culture. 20 µl fresh medium was added to the drop every two days.

The culture medium recipes for different cells are as follows: NIH 3T3 fibroblasts (3T3)-MEM-alpha supplemented with 10% fetal bovine serum (FBS), 1% L-glutamine, and 1% penicillin-streptomycin; human embryonic kidney 293FT cells (293FT), mouse myoblast cells (C2C12), and cervical cancer cells (Hela)-DMEM supplemented with 10% FBS and 1% penicillin-streptomycin; mESC-DMEM supplemented with 15% knock out TM SR serum replacement, 0.1 mM MEM nonessential amino acids, 2 mM GlutaMax-1, 1 mM sodium pyruvate, 1% penicillin-streptomycin, 1000 U/ml leukemia inhibitory factor, and 0.1 mM β-mercaptoethanol.

3.4.5.2   Sterile Operation

Sterile disposable consumables (e.g., cartridge syringe and petri dish) are used to prevent contamination. For the heat-resistant apparatus, such as nozzle needle and other glass or metal parts, autoclaving is applied. For those that cannot stand autoclaving, ethanol spraying and UV treatment (40 min) are performed subsequently. 3D bioprinter (printing platform and nozzle area) and cell culture hood were sterilized with ethanol and UV (40 min) before use.

All the prepared non-viscous solutions (e.g., culture medium, $CaCl_2$ solution and initiator solution) are filter-sterilized (0.22 µm) before use. Similar to pasteurization, gelatin and alginate solutions are treated with three cycles of 70 °C for 30 min every hour. For modified hyaluronic acid and gelatin, filter sterilization was performed before freeze-drying, and materials powder was treated with UV for 40 min before dissolving in the desired buffer.

3.4.5.3   Smooth Extrusion Measurement

To measure the extrusion force, a flexible force sensor (FlexForce[TM], Tekscan) was placed between the cartridge piston and nozzle pusher, where the sensing region was fully covered by their contact area. By recording the exported voltage value obtained from the incorporated signal transfer, and using the force calibration curve as a reference, the actual force could be determined. This force value could be used to determine the difficulty of extruding specific bioinks, while its fluctuation with time might indicate non-stationary of extrusion.

3.4.5.4   Compression Test

Standard cylinder (diameter 6 mm and thickness 1.8 mm) or cubic ($10 \times 10 \times 5$ mm) models are printed for compression test (Q800, TA Instruments or ELF3200, BOSE).

The stress–strain curve is obtained under a ramp compression (~10% strain per min), and compression modulus was determined during strain 10–20%, where the linear correlation coefficient (R^2) was confirmed to be 0.94–0.99. The limit load and strain are also recorded.

3.4.5.5 Fluorescence Labeling

To better visualize the printed structure, some of the bioinks (e.g., methacrylated and norbornene-functionalized hyaluronic acid) are pre-labeled with fluorescence. Briefly, polymer powder is combined in a triethanolamine buffer (pH 10) with a fluorescent peptide (either GCKK-fluorescein or GCKK-rhodamine), such that the molar ratio polymer:fluor-peptide is approximately 1:2 (moles of full-length polymer molecule: moles fluorescent peptide). The reaction proceeds at room temperature for 2 h, after which the solution is neutralized and then purified by dialysis and lyophilization to yield the final product. Compared with blending fluorescence dye with hydrogel formulations, the conjugation would more precisely indicate the labeled polymer without concerns of dye release.

3.4.5.6 LIVE/DEAD^TM Staining

To perform LIVE/DEAD^TM staining, cell-laden constructs are immersed in working solution containing 1 µM Calcein-AM and 2 µM propidium iodide. After 15 min incubation at room temperature, the samples are washed with PBS and observed under fluorescence (Olympus BX51) and confocal microscope (Nikon Z2) systems. Living (green) and dead (red) cells are counted using Image-J, and cell viability is calculated as the proportion of living cells among total cells.

3.4.5.7 Immunostaining

Cells or cell-laden samples were fixed with 4% paraformaldehyde (PFA) for 20 min and permeabilized with 0.1% Triton-X 100 in PBST (0.1% Tween in PBS) for 30 min. After blocking with 5% bovine serum albumin (BSA) in PBST for 1 h, the samples were incubated with the primary antibodies (Oct4 and SSEA1 were used for embryonic stem cells staining) for 12 h at 4 °C. The samples were washed with PBST and then incubated with the second antibodies Alexa Fluor® 594 and 488 for 2 h. Nucleus staining was optionally performed with DAPI (5 µg/ml) after washing the samples. Confocal microscope (Nikon Z2) was used to analyze the results.

3.4.5.8 Flow cytometry

To perform flow cytometry, cells are harvested from 3D-bioprinted samples after dissolving the hydrogel constructs (e.g., immersing cell-laden gelatin–alginate construct in 150 mM sodium chloride buffer containing 55 mM sodium citrate and 20 mM EDTA for 5 min). For collected cell aggregates (e.g., embryoid bodies), they are treated with cell dissociation reagent (StemPro Accutase) at 37 °C for 5 min to obtain single cell suspension. In the case of ESCs printing, immunostaining of markers Oct4 and SSEA1 is performed, followed by analysis using a flowcytometer (FACS Aria III, BD).

3.4.5.9 qRT-PCR

After washing with PBS three times, 1 mL Trizol (Invitrogen) was added to each cell sample, followed by 10 min incubation on ice and 1 min stirring to complete homogenization. The mixtures are then transferred to 1.5 mL EP tube, supplemented with 200 μL chloroform followed by vigorous shaking and 5 min incubation at room temperature. Samples are then centrifuged at 12,000 rpm, and 4 °C for 15 min and the upper aqueous layer is collected to a new tube. RNA is isolated through being blended with isopropanol, followed by 15 min incubation at room temperature. After centrifuging at 12,000 rpm and 4 °C for 10 min, the supernatant is removed and the RNA is washed with 75% ethanol. After centrifuging at 7500 rpm and 4 °C for 5 min, the collected RNA is dissolved in DEPC water. The concentration of RNA is determined by measuring the absorbance at 260 nm in a spectrophotometer (Thermo-Scientific) and the purity of RNA is estimated from the ratio of readings at 260 and 280 nm.

RNA samples are transcribed to cDNA using PrimeScript ™ II 1st strand cDNA Synthesis Kit (TaKaRa). qRT-PCR is performed on a real-time PCR detection system (CFX96, Bio-Rad) with Maxima SYBR Green qPCR master mix (Thermo-Scientific) in triplicate as per manufacturer's instructions. Relative expression is determined by delta–delta Ct method with the expression of GAPDH as housekeeping reference. The sequence of the gene-specific primers for PCR is as follows: GAPDH, (5′ primer) CATCACCATCTTCCAGGAGC and (3′ primer) ATGCCAGTAGCTTC-CCGTC; Oct4, (5′ primer) GAAGCAGAAGAGGATCACCTTG and (3′ primer) TTCTTAAGGCTGAGCTGCAAG; Nanog, (5′ primer) CCTCAGCCTCCAGCA-GATGC and (3′ primer) CCGCTTGCACTTCACCCTTTG.

3.4.5.10 Western Blot

Wnt3a protein expression is quantified by western blot. Wnt3a-293FT cells (final concentration 10^7 cells/ml) is 3D-printed as described above. After 10 h incubation, the culture medium is replaced with DMEM/F12 medium without FBS but supplemented with 0.1 μg/ml heparin (SIGMA, H3149, USA). 48 h later, the supernatant

around tissue constructs is removed. The constructs are then dissolved in 55 mM sodium citrate and 20 mM EDTA in 0.9 wt% NaCl and stirred using a pipette for 10 min to allow alginate depolymerization and cell isolation. Cells are lysed in RIPA buffer, and cell lysates (20 μg total protein per lane) are separated by electrophoresis on a 12% polyacrylamide gel. Then proteins are transferred from the gel onto a nitrocellulose membrane and blocked for 1 h at RT in TBS containing 5% skimmed milk and 0.1% Tween 20, followed by overnight incubation at 4 °C with the primary antibody (Mouse anti-Flag-M2 (Sigma), 1/1000 dilution) in the same buffer. Membranes are then incubated with the secondary antibody (goat anti-mouse IgG (HRP-linked) (Jackson), 1/1000 dilution) for 1 h in 1 × TBS with 1% skim milk and 0.1% Tween20 at RT. Proteins are detected using ECL + solution (DingGuo) and gel image system (Bio-Rad, Chemi-Doc™XRS + System, USA).

3.4.5.11 Scanning Electron Microscope

The details of 3D-printed structure (e.g., porosity and cell morphology) are checked by scanning electron microscope (SEM). After fixation with 4% PFA for 30 min, cell-laden construct is frozen in −80 °C, followed by freeze-drying for 24 h. With gold-spray, the dry construct is analyzed under an SEM system (Quanta 200, FEI).

3.4.5.12 Statistical Analysis

Unless otherwise stated, all data are presented as Mean ± standard deviation. Data are analyzed using GraphPad Prism software for analysis of variance (ANOVA) together with Bonferroni or Tukey HSD post-test. The significance is defined as: $*p < 0.05$, $**p < 0.01$, and $***p < 0.001$.

References

1. Groll J, Boland T, Blunk T, Burdick JA, Cho DW, Dalton PD, Derby B, Forgacs G, Li Q, Mironov VA, Moroni L, Nakamura M, Shu W, Takeuchi S, Vozzi G, Woodfield TB, Xu T, Yoo JJ, Malda J (2016) Biofabrication: reappraising the definition of an evolving field. Biofabrication 8(1):013001
2. Blaeser A, Campos DFD, Puster U, Richtering W, Stevens MM, Fischer H (2016) Controlling shear stress in 3D bioprinting is a key factor to balance printing resolution and stem cell integrity. Adv Healthc Mater 5(3):326–333
3. He Y, Yang F, Zhao H, Gao Q, Xia B, Fu J (2016) Research on the printability of hydrogels in 3D bioprinting. Sci Rep 6:29977
4. Chung JHY, Naficy S, Yue ZL, Kapsa R, Quigley A, Moulton SE, Wallace GG (2013) Bio-ink properties and printability for extrusion printing living cells. Biomater Sci 1(7):763–773
5. Kyle S, Jessop ZM, Al-Sabah A, Whitaker IS (2017) 'Printability' of candidate biomaterials for extrusion based 3D printing: state-of-the-art. Adv Healthc Mater 6(16)

6. Radhakrishnan J, Krishnan UM, Sethuraman S (2014) Hydrogel based injectable scaffolds for cardiac tissue regeneration. Biotechnol Adv 32(2):449–461
7. Malda J, Visser J, Melchels FP, Jungst T, Hennink WE, Dhert WJ, Groll J, Hutmacher DW (2013) 25th anniversary article: engineering hydrogels for biofabrication. Adv Mater 25(36):5011–5028
8. Colosi C, Shin SR, Manoharan V, Massa S, Costantini M, Barbetta A, Dokmeci MR, Dentini M, Khademhosseini A (2016) Microfluidic bioprinting of heterogeneous 3D tissue constructs using low-viscosity bioink. Adv Mater 28(4):677–684
9. Yan KC, Nair K, Sun W (2010) Three dimensional multi-scale modelling and analysis of cell damage in cell-encapsulated alginate constructs. J Biomech 43(6):1031–1038
10. Sung HW, Huang DM, Chang WH, Huang RN, Hsu JC (1999) Evaluation of gelatin hydrogel crosslinked with various crosslinking agents as bioadhesives: in vitro study. J Biomed Mater Res 46(4):520–530
11. Rowley JA, Madlambayan G, Mooney DJ (1999) Alginate hydrogels as synthetic extracellular matrix materials. Biomaterials 20(1):45–53
12. Burdick JA, Prestwich GD (2011) Hyaluronic acid hydrogels for biomedical applications. Adv Mater 23(12):H41–H56
13. Novosel EC, Kleinhans C, Kluger PJ (2011) Vascularization is the key challenge in tissue engineering. Adv Drug Deliv Rev 63(4–5):300–311
14. Zhang T, Yan KC, Ouyang L, Sun W (2013) Mechanical characterization of bioprinted soft tissue models. Biofabrication 5(4):045010
15. Ouyang L, Yao R, Zhao Y, Sun W (2016) Effect of bioink properties on printability and cell viability for 3D bioplotting of embryonic stem cells. Biofabrication 8(3):035020
16. Nair K, Gandhi M, Khalil S, Yan KC, Marcolongo M, Barbee K, Sun W (2009) Characterization of cell viability during bioprinting processes. Biotechnol J 4(8):1168–1177

Chapter 4
3D Bioprinting of Shear-Thinning Self-assembly Bioink

When applying a new material as a bioink in microextrusion bioprinting, numerous considerations need to be addressed. As stated in Chap. 3, one of the primary considerations is printability, which normally encompasses the material's ability to (i) be injected from a printhead (ii) undergo rapid gelation upon deposition, and (iii) exhibit suitable mechanical properties that would support the printed structure. Given this, we seek to explore hydrogel formulation that could meet these criteria. Specifically, in this chapter, we will apply a shear-thinning and rapidly self-healing guest–host hydrogel based on hyaluronic acid (HA) to microextrusion 3DP. Adamantane (Ad, guest) and β-cyclodextrin (CD, host) moieties are separately coupled to HA, to create two hydrogel precursors that form a supramolecular assembly upon mixing [1]. It is hypothesized that such formulation would allow for smooth extrusion and temporary stabilization post-extrusion because of the shear-thinning and self-healing properties, respectively. To enhance the structural integrity of the supramolecularly crosslinked hydrogel, we also introduce photo-crosslinkable groups onto the macromers. We then investigate how each type of crosslinking (guest–host, photo-crosslinking, and their combination) affects the printability of multilayer scaffolds. Post-crosslinking methods are also explored concerning structural integrity and stability over time. Printed structures can be further functionalized to support cell culture. Similar dual-crosslinking mechanisms based on supramolecular and covalent bonding may enable the development of 3D printable hydrogel bioinks from materials that cannot otherwise be printed.

Parts of this chapter have been published in *ACS Biomaterials Science and Engineering* [2].

4.1 Bioink Preparation and Characterization

4.1.1 Guest–Host Chemistry Modification of Hyaluronic Acid

Hyaluronic acid (HA) is a non-sulfated glycosaminoglycan widely distributed throughout connective, epithelial, and neural tissues [3, 4]. Various chemical modifications have been applied to HA to achieve different functionalization, which is usually performed based on the glucuronic acid, carboxylic acid, N-acetyl group, and two hydroxy groups [3]. With high repeatability and controllability, esterification of the carboxylic acid is one of the most widely used reactions. Guest–host chemistry has been recently applied to HA to form supramolecular hydrogels, showing great potential in tissue engineering (e.g., cardiac, cartilage) and molecule delivery (e.g., drug, siRNA) as injectable biomaterials [1, 5]. Here, we aim to develop a bioink based on guest–host HA formulation with adamantane and β-cyclodextrin as guest and host groups, respectively [1].

Adamantane-HA (Ad-HA) and β-cyclodextrin-HA (CD-HA) were synthesized as described previously [1]. Briefly, to make HA (90 kDa, Lifecore) dissolvable in dimethyl sulfoxide (DMSO), the tetrabutylammonium salt of HA (HA-TBA) was firstly prepared by adding Dowex-100 and Tetrabutylammonium hydroxide in 2 wt% HA aqueous solution. Ad-HA was obtained through anhydrous coupling of 1-adamantane acetic acid to HA-TBA via ditert-butyldicarbonate (Boc2O)/4-dimethylaminopyridine (DMAP) esterification in DMSO. CD-HA was obtained by coupling 6-(6-aminohexyl)amino-6-deoxy-β-cyclodextrin (β-CD-HDA) to HA-TBA via an amidation reaction using (benzotriazol-1-yloxy)tris(dimethylamino)phosphonium hexafluorophosphate (BOP) in anhydrous DMSO. Both Ad-HA and CD-HA reactions were dialyzed against DI water for one week, followed by freeze-drying. The modification percentage of adamantane (21%) and β-cyclodextrin (25%) for the modified macromers were determined by ^{1}H NMR (Bruker 360 MHz) (Fig. 4.1).
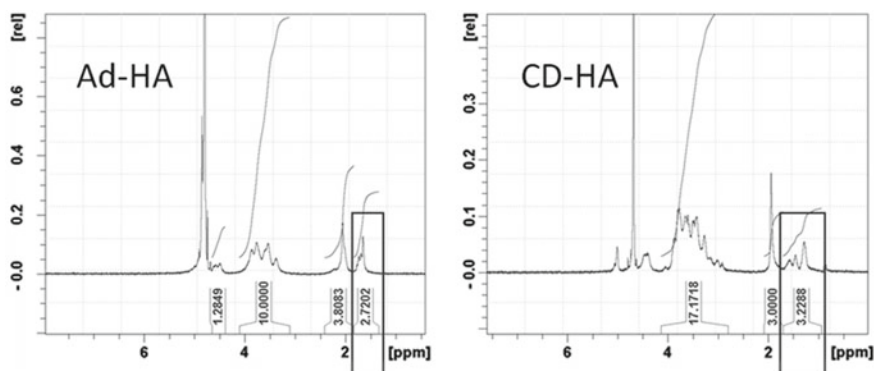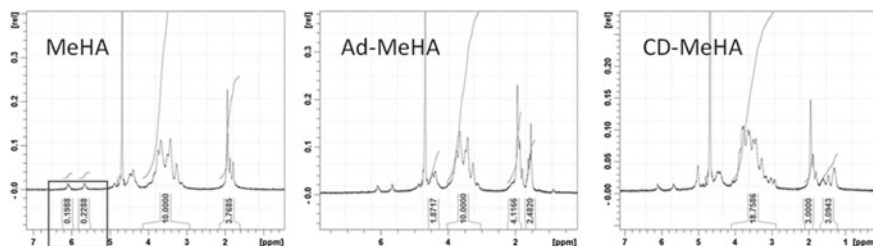

Fig. 4.1 ^{1}H-NMR spectrum of Ad-HA and CD-HA. Reproduced, with permission from [2]

Fig. 4.2 ^{1}H-NMR spectrum of MeHA, Ad-MeHA, and CD-MeHA. Reproduced, with permission from [2]

4.1.2 Methacrylation of Hyaluronic Acid

As a supramolecular network, guest–host self-assembly usually presents significant shear-thinning property, which might make it unstable to maintain shape fidelity. To achieve covalent crosslinking network, methacrylate groups were introduced to HA backbones for free radical polymerization. Methacrylated HA (MeHA) was prepared through the reaction of HA with methacrylic anhydride as reported previously [6]. Briefly, 3 eq MA was added dropwise to aqueous 1 wt% HA solution on ice, adjusting pH to 8 for 6–8 h. After reacting overnight at 4 °C, another 3 eq MA was added to the reaction, followed by neutralization to pH ~7–7.5. Modification of MeHA was confirmed with ^{1}H-NMR as ~22% (Fig. 4.2). Following the previous guest–host modification, adamantane-MeHA (Ad-MeHA) and β-cyclodextrin-MeHA (CD-MeHA) could be obtained based on MeHA (Fig. 4.2).

4.1.3 Preparation of Bioinks

It has been well known that the ratio of guest to host groups would greatly affect the overall properties of the generated supramolecular hydrogels [7]. To better use the modifications, we applied a ratio of 1:1 for adamantane to β-cyclodextrin when calculating the amounts of each precursor component based on the following equation:

$$\frac{m_{\text{Ad}}}{M_{\text{Ad}}} \cdot \text{mod}_{\text{Ad}} = \frac{m_{\text{CD}}}{M_{\text{CD}}} \cdot \text{mod}_{\text{CD}} \tag{4.1}$$

where m_{Ad} and m_{CD} represent the mass of guest (Ad-HA or Ad-MeHA) and host (CD-HA or CD-MeHA) components, M_{Ad} and M_{CD} represent the unit molecular weight of guest and host precursors, while mod_{Ad} and mod_{CD} represent the modification degree of adamantane and β-cyclodextrin, respectively.

All HA macromers were prepared in PBS buffer. To allow for photo-polymerization, 0.05 wt% photo-initiator Irgacure 2959 ((4-(2-hydroxyethoxy)phenyl-(2-propyl)ketone, I2959) was included for methacrylated HA
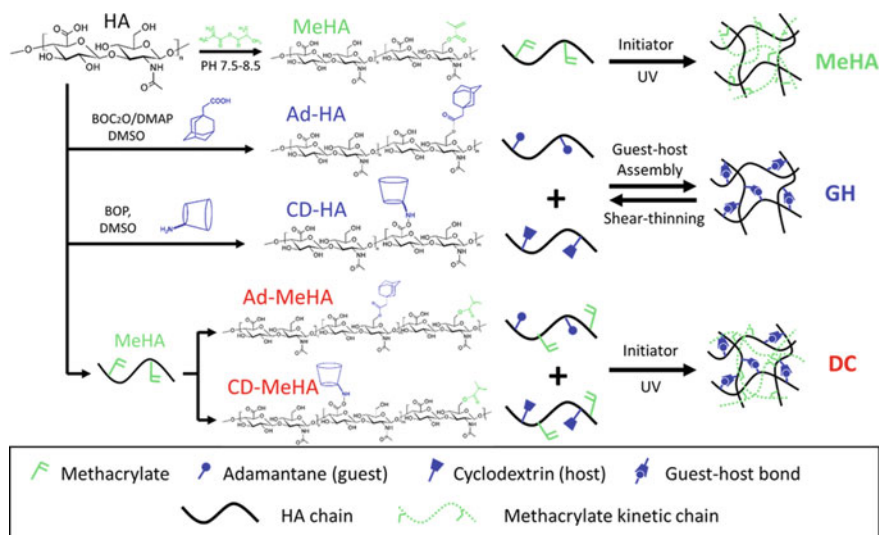
Fig. 4.3 Schematic of synthesis and hydrogel formation processes of three types of formulations, MeHA, GH, and DC. Reproduced, with permission from [2]

macromer (MeHA, Ad-MeHA, and CD-MeHA) solutions. For guest–host-based mixture formulations (Ad-HA/CD-HA and Ad-MeHA/CD-MeHA), individual macromer solutions were prepared and mixed completely following Eq. (4.1). Three hydrogel groups (Fig. 4.3) were studied, namely MeHA (photo-crosslinking, MeHA), Ad-HA/CD-HA (guest–host, GH), and Ad-MeHA/CD-MeHA (dual-crosslinking, DC), the macromer concentrations of which varied from 5 to 20 wt%. For those experiments involving cell culture, the macromer powders were sterilized with a germicidal light for 30 min.

4.1.4   Rheological Characterization

We first assessed the relaxation behavior of different formulations by placing the vials containing hydrogels on their side (Fig. 4.4). As a control, low-viscosity, unpolymerized MeHA flowed immediately, whereas GH hydrogels with only guest–host bonds relaxed gradually over several hours. Specifically, GH hydrogel composited with HA modified with 20–25% adamantane and β-cyclodextrin was observed to maintain their shape quite well for up to 10 min. After photo-polymerization, DC hydrogel kept its shape for up to one month as polymerized MeHA did. This rapid covalent crosslinking with UV irradiation allows printed filaments to be further stabilized against forces that could otherwise cause dispersion or collapse of the hydrogel over time.
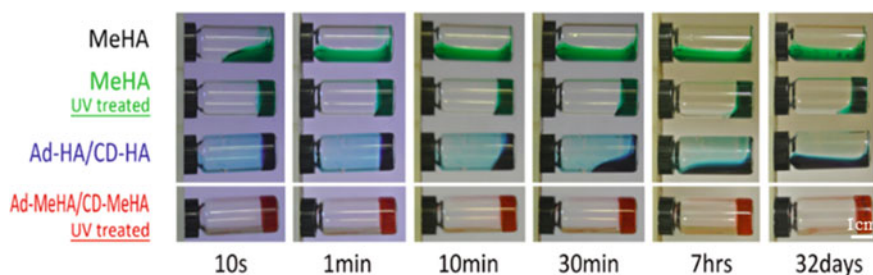
Fig. 4.4 Images of various hydrogels (all at 5 wt%) in vials on their side for up to one month. Reproduced, with permission from [2]

Furthermore, rheological measurements were performed at 25 °C on an AR2000 rheometer (TA Instruments) using a cone-plate geometry. The responses to shear were examined using continuous flow tests with a linearly ramped shear rate from 1 to 100 s^{-1}. Responses to increasing strain were measured using oscillatory strain sweeps from 0.01 to 500% at 10 Hz, while the frequency dependence was measured using oscillatory frequency sweeps from 0.01 to 100 Hz at 0.2% strain. Shear recovery experiments were performed to test the material responses to the application and removal of shear, where oscillatory time sweeps were conducted (10 Hz) with alternating strains of 250/0.5% every 2 min. To measure the response to photopolymerization, in situ polymerization was performed with UV light (15 mW/cm^2, 320–390 nm) for 5 min via a UV-curing stage during oscillatory time sweeps at 1 Hz and strain 0.5%.

Time sweeps of modified HA macromer solutions showed that at frequency of 10 Hz and strain of 0.5%, the shear moduli of MeHA, Ad-HA, and CD-HA solutions were low (<50 Pa), and the storage component (G') was generally lower than the loss component (G''), reflecting properties of viscous solutions. Significantly higher G' and G'' values (∼1000 Pa) were observed for Ad-HA and CD-HA mixture (GH), with G' higher than G'', indicative of gelation by supramolecular crosslinking (Fig. 4.5a). Furthermore, for GH materials, G'' surpassed G' beyond the linear viscoelastic region (LVR) at high strains in oscillatory strain sweeps (Fig. 4.5b), indicating shear yielding, which is essential for material extrusion. The oscillatory frequency sweeps also showed that the GH materials underwent a conversion from sol to gel with increasing frequency in a concentration-dependent manner, indicating that fluid-like settling of GH hydrogels may occur over long-time scales and it was slowed by increased polymer concentration (Fig. 4.5c).

The continuous flow experiments show that the viscosity of GH materials decreased with increasing shear rate under different concentrations, demonstrating shear thinning, with viscosity under high shear similar to that of an uncrosslinked MeHA solution (Fig. 4.6a). The viscosity of MeHA was lower than that of GH materials and remained constant as a function of shear rate (Fig. 4.6a). When tested under alternating low/high strains, the DC hydrogels went from gel to sol in response to strain prior to photo-crosslinking (Fig. 4.6b). Furthermore, the thinning responses to
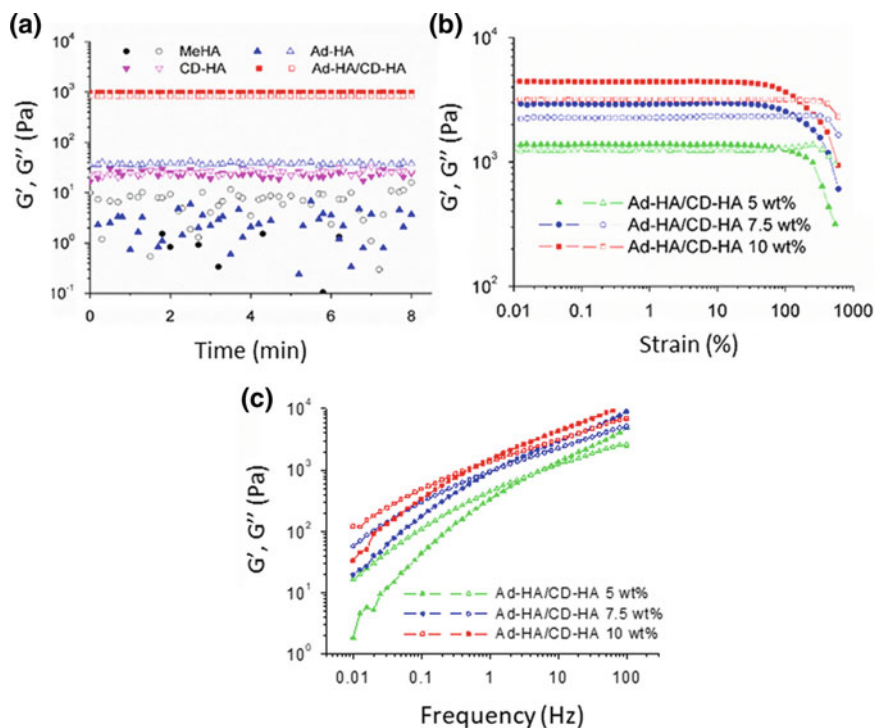
Fig. 4.5 Oscillatory **a** time sweeps (strain 0.5% and frequency 10 Hz), **b** strain sweeps (frequency 10 Hz), and **c** frequency sweeps (strain 0.2%) of different modified HA macromers under different concentrations. 5 wt% macromers were used in (**a**). Reproduced, with permission from [2]

high strain and mechanical recoveries at low strain were demonstrated to be rapid and repeatable (Fig. 4.6b). Together with the shear-thinning properties, this rapid transition from gel to sol in response to the strain is believed to make the hydrogel material well-suited for microextrusion bioprinting. Specifically, the rapid recovery of mechanical properties after removal of shear, as during deposition of a gel filament, might allow for stabilization of the printed filaments immediately after extrusion. When exposing hydrogels containing methacrylates to light, rapid polymerization (<5 min) was observed with a multiple orders of magnitude increase in G' (Fig. 4.7).

4.1.5 3D Bioprinting Process Design

Toward application in 3D bioprinting, a process was developed that harnessed the shear-thinning and self-assembling behavior of the guest–host formulations and the stabilization afforded with photo-polymerization of the methacrylate groups.

Fig. 4.6 **a** Continuous flow tests of MeHA, GH, and DC materials at a shear rate range (1–100 1/s) equivalent to those experienced during printing, showing shear-thinning behavior with viscosities of GH and DC assemblies approaching that of the MeHA solution at high shear rates. **b** Time sweeps of the 5 wt% DC hydrogels prior to light irradiation under cyclic strains of 250% (high, shaded area) and 0.5% (low, unshaded area) at 10 Hz. Reproduced, with permission from [2]
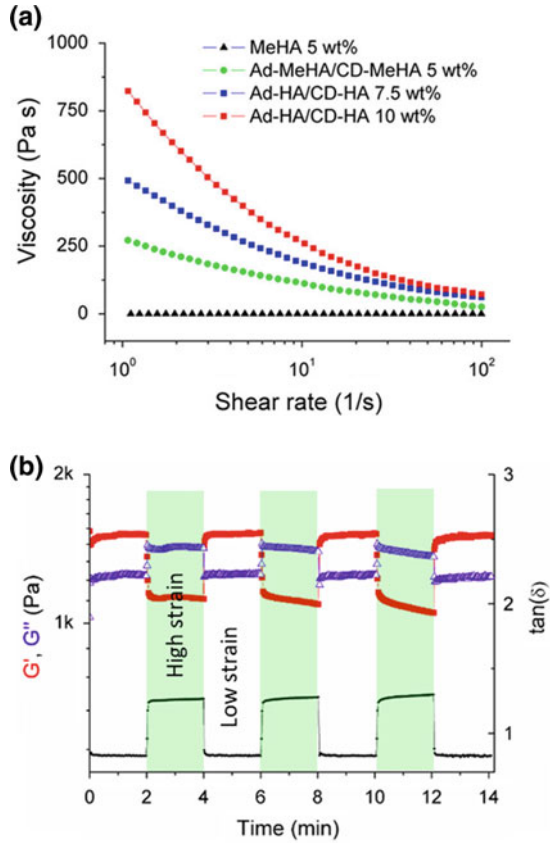
Fig. 4.7 Time sweep of photo-crosslinking with UV exposure (15 mW/cm^2 for 5 min as indicated by shaded area), G' (closed symbols), and G'' (open symbols). Reproduced, with permission from [2]
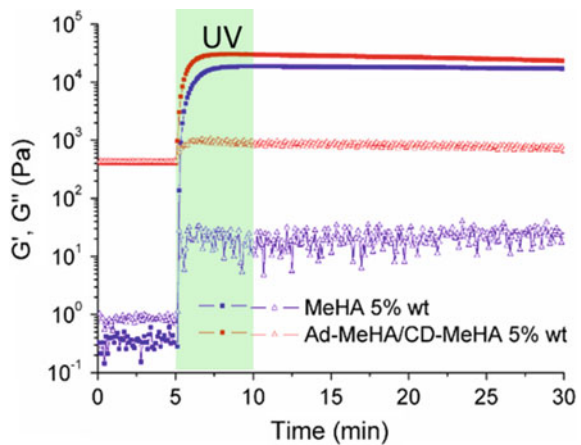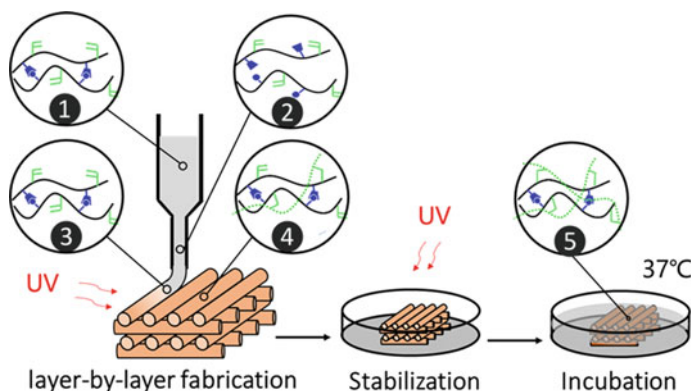
Fig. 4.8 Schematic of 3D layer-by-layer fabrication, structure stabilization, and incubation processes for DC hydrogels. The incorporated steps include: (1) supramolecular hydrogel self-assembly with guest–host bonds within the cartridge; (2) guest–host bonds disruption when extruded through the narrow needle, due to shear; (3) rapid self-healing of the guest–host bonds and supramolecular hydrogel when shear is removed and the material is deposited; (4) UV treatment to photo-crosslink methacrylates within the printed hydrogels; and (5) further stabilization to enforce the polymerized network. Reproduced, with permission from [2]

The general process is outlined in Fig. 4.8 with stepwise inserts. The process involves a shear-thinning and self-healing guest–host hydrogel (e.g., Ad-MeHA/CD-MeHA mixture) loaded into a cartilage for extrusion, the disassembly of the gel at the interface between the gel and needle with shear, and the self-healing of the gel upon extrusion onto a substrate. In the presence of photo-initiator and light exposure, covalent crosslinks were subsequently introduced to stabilize the printed structures. Control hydrogel groups that incorporated only the MeHA macromer (no guest–host assembly) or only the Ad-HA and CD-HA (no covalent crosslinking) were also investigated.

The 3DP was performed using a modified FDM 3D printer (Revolution XL, Quintessential Universal Building Device), where the melting nozzle was replaced with a customized one capable of loading syringes. Open-source softwares were used for both slicing (Slic3r) and printing control (Repetier).

4.2   Printability and Stability

4.2.1   Gel Filament Generation

As stated previously, the formation and maintenance of gel filament lay the basis for building up 3D constructs. Here, we extruded the bioink through a needle to assess its extrusion behavior and thus the filament formation. For low-viscosity formulation, 5 wt% MeHA, for example, the materials came out from the needle drop by drop
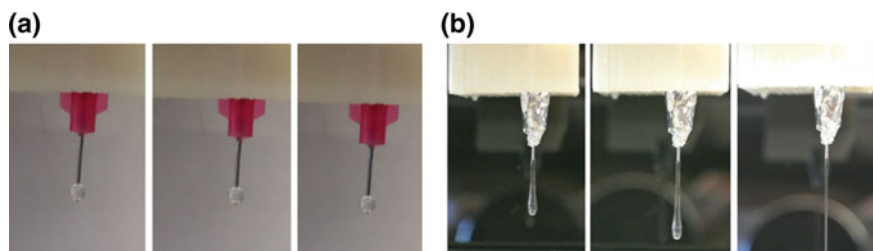
Fig. 4.9 Extrusion status of **a** 5 wt% MeHA and **b** 5 wt% DC hydrogels using a 25-G needle. Reproduced, with permission from [2]

Fig. 4.10 Consistency of filament and extrusion force during printing. **a** Image of the printed filament from the 5 wt% GH ink under constant extrusion rate and needle translation speed, and **b** force measured at the piston during extrusion of the GH or DC inks. Reproduced, with permission from [2]
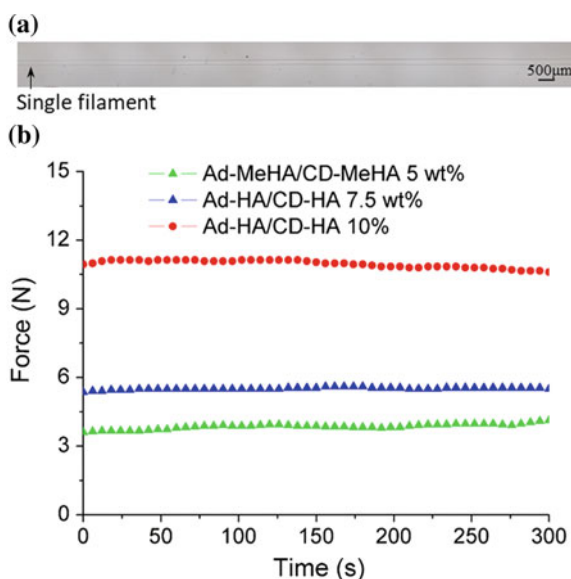
(Fig. 4.9a), which match the rheological characterization. After adding the guest–host chemistry, 5 wt% DC bioink was able to hang on the tip of the needle and continuously generate standard filament (Fig. 4.9b). Furthermore, by depositing the DC bioink on a flatbed, we obtained a straight uniform filament (Fig. 4.10). To better assess the extrusion stability, we measured the extrusion force by introducing a force sensor between the extruder and piston. As shown in Fig. 4.10, the higher of the bioink concentration, the higher of the required force; the force increased from ~4 to ~11 N when raising the concentration from 5 to 10 wt%. More importantly, the applied forces were fairly stable for both GH and DC bioinks, indicating the smooth extrusion.

Ideally, the printed filament should present as a standard circular cylinder; however, collapse and deformation might happen due to the bioink relaxation induced by gravity. To assess the ability of shape maintenance for some bioink, here we seek to characterize the deformation of filaments. Basically, we assumed the actual filament

to present an oval cross-sectional geometry, which should have an equal area to the ideal circular cross section, given the conservation of extrusion volume. Here, we defined a deformation viable m as follows:

$$m = \frac{b}{a} = \frac{4A_c}{\pi a^2} \tag{4.2}$$

where a and b are the width and height of the actual filament, respectively, while A_c is the cross-sectional area. The m value for an ideal filament would be 1, which is also a limit for actual cases. Therefore, the bigger of the m value, the closer of the filament to an ideal case and the better filament maintenance is indicated.

To assess the difference in filament maintenance, we print different types of bioinks into parallel lines on the printing bed, using the same parameters (extrusion flux 0.22 ml/h, needle gauge G25, nozzle moving speed 2 mm/s), which would induce an ideal filament with diameter of 200 µm (Fig. 4.11a). From the quantification of filament width and estimation of m value, we found that the MeHA bioinks deserved significantly lower m than GH and DC groups (Fig. 4.11b). The m value for 5% MeHA was ~0.11, while those for 5% GH and 5% DC are similarly ~0.37. The higher of the bioink concentration, the bigger of m value. In particular, 10 wt% GH hydrogels were observed to exhibit an n value closest to 1, which meant that the filament cross-sectional outline was nearly circular. These results indicate that the guest–host formulation would significantly enhance the filament shape maintenance and increasing the concentration would also add to the effects.

Apart from bioink concentration, many other parameters would affect the filament size, such as UV light intensity, extrusion flux, needle size, and printing speed. When applying UV light in situ right after the extrusion of 5 or 10 wt% MeHA, we found that the filament size was significantly smaller, which indicated better gel maintenance (Fig. 4.12a). However, even with UV treatment, all the MeHA groups ranging from 5 to 20 wt% still presented flatter gel filament compared with 5 wt% DC bioink. Thus, although UV irradiation during printing increased circularity for methacrylated macromers, the rapid reassembly of the supramolecular bonds post printing was needed to maintain a cross section that approached ideal circularity.

Using the GH ink, the filament size was investigated with changes in printing parameters. The results showed that the filament size increased with the increase of extrusion flux and that, generally, a smaller needle (increased gauge (G)) resulted in smaller filaments (Fig. 4.12b). Under fixed extrusion flux and needle gauge, the filament size decreased as the needle's speed increased, and the relationship curve was well-fit (R^2 of 0.99) by a power law (Fig. 4.12c). However, when the needle moving speed was too high, the filament was not continuous. In general, the filament size can, therefore, be controlled and as needed ranging from 100 to 500 µm through modulation of these parameters. Although the filament size could be varied within a single printed construct, this capability was not explored here. The ability to print thinner filaments from larger diameter needles by tuning needle speed might, for example, offer the ability to increase print resolution while minimizing shear forces experienced by an ink.
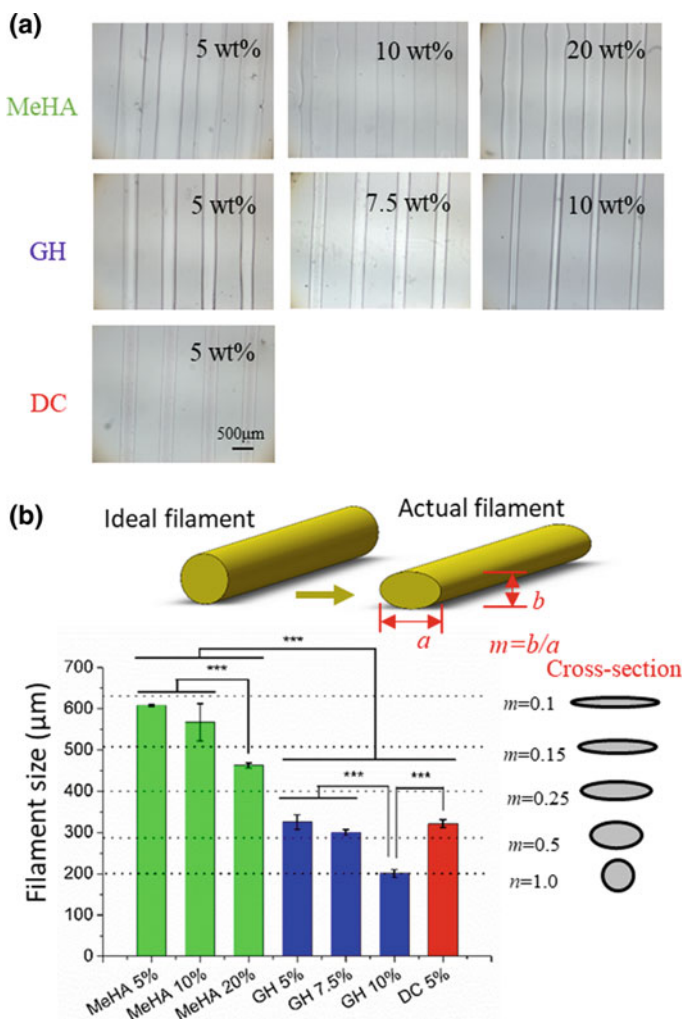
Fig. 4.11 Characterization of printed filaments. **a** Visualization and **b** quantification of filament sizes for MeHA, GH, and DC hydrogels under the same printing parameter configuration (extrusion flux of 0.22 ml/h, 25-G needle, moving speed of 2 mm/s) at varying concentrations. Reproduced, with permission from [2]

4.2.1.1 3D Structure Fabrication

The benefits of the dual supramolecular–covalent crosslinking system in stabilizing printed filaments were clearly observed as layers of a 3D construct were deposited upon one another (Fig. 4.13). Different layers of lattice structures were printed in a layer-by-layer fashion using various ink formulations to evaluate their printability, where MeHA and DC groups received simultaneous UV irradiation during printing.
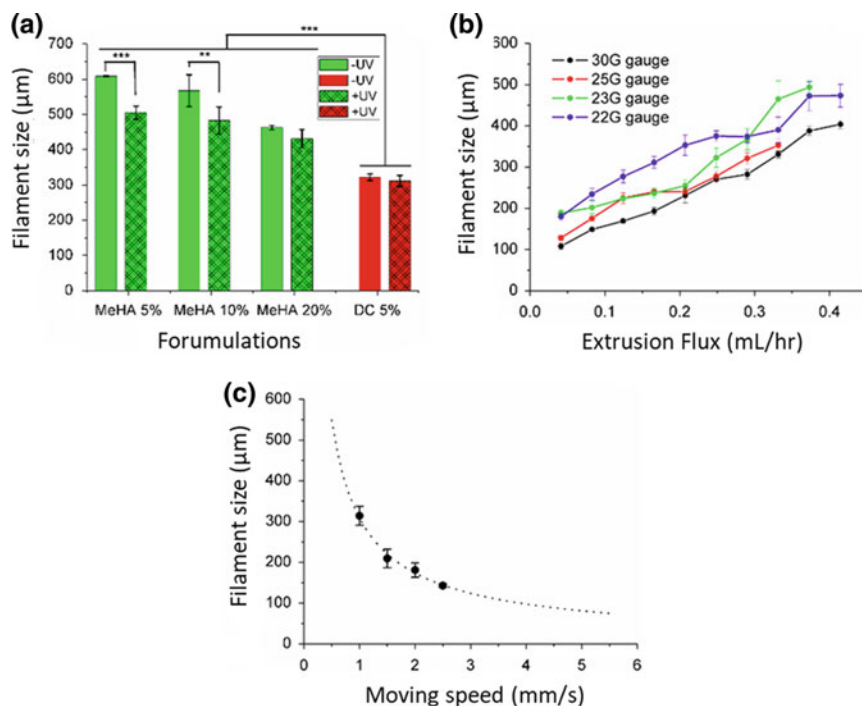
Fig. 4.12 **a** Filament sizes with UV exposure (15 mW/cm^2) during printing ($\sim$50 s) for MeHA and DC hydrogels. **b** Filament sizes with variations in extrusion flux and needle gauge with a fixed moving speed (1.5 mm/s). **c** Filament sizes with variations in moving speed under fixed extrusion flux (0.14 mL/h) and needle gauge (25G). 5 wt% GH hydrogels were used in (**b**, **c**). Reproduced, with permission from [2]
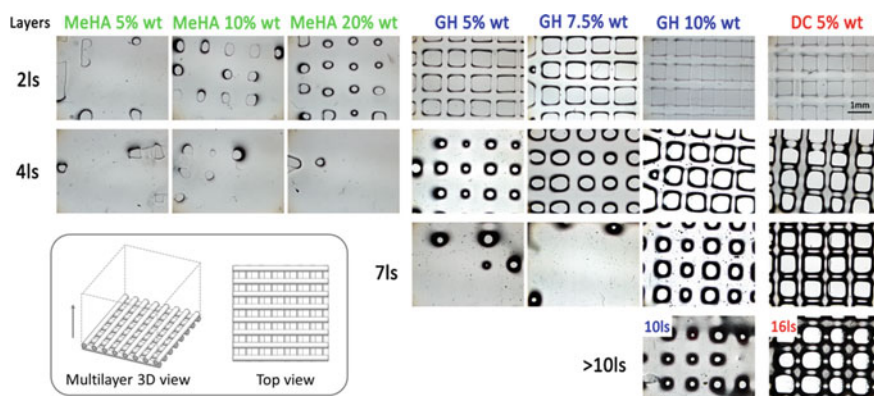
Fig. 4.13 Printing of 3D structures. Phase images of printed lattice structures (CAD model shown as inset) with different layers for MeHA, GH, and DC hydrogels, where MeHA and DC groups were treated with 15 mW/cm^2 UV simultaneously. The number of layers (ls) printed (left) and hydrogel concentration (top) are indicated. Reproduced, with permission from [2]

As shown in Fig. 4.13, the MeHA ink, stabilized only by UV-induced crosslinking, did not gel fast enough to avoid flow and coalescence. This ink could not deliver a clear lattice structure even with only two printed layers, and all of the filaments had coalesced when four layers had been printed.

When using GH inks, more layers could be deposited while maintaining a clear lattice pattern compared with the MeHA ink, although relaxation and coalescence of printed filaments were ultimately observed as layers were deposited. Increasing the concentration of the GH ink contributed to better performance when compared to lower concentrations. Specifically, GH-5 wt% and GH-7.5 wt% groups coalesced after only seven layers had been deposited. While a lattice structure was identified in a ten-layer construct fabricated from the GH-10 wt% ink, the filaments were still obviously fused together, with increasingly small void spaces between the filaments in the lattice.

When using the DC ink at a concentration of 5 wt%, a standard multilayered structure (up to sixteen layers) was possible (Fig. 4.13). Thus, the combination of the guest–host assembly and the secondary photo-crosslinking was needed to preserve the printed structures in multilayer scaffolds. Structures stabilized by supramolecular interactions formed well-spaced filaments that were stable temporally, as evidenced by the two-layer prints of the GH and DC groups. However, the covalent crosslinking mechanism was necessary to stabilize printed structures against relaxation of the supramolecular network and resulting flow of material that was observed in all of the GH groups as layers printed. The DC ink yielded stable structures that maintained spatial fidelity to the computer model for as many layers as were printed.

Printing with the DC ink allowed the rapid fabrication of many structures, including stable tubes and hydrogel sheets (Figs. 4.14 and 4.15). This indicates the potential for this ink material to be used as a substrate for the creation of engineered tissue constructs. It should be noted that the potential exists—and has been previously demonstrated in HA hydrogels—for the crosslinks used here to have designed degradation profiles, where crosslinks are susceptible to hydrolysis or enzymatic degradation, including crosslinks formed by the guest–host assembly.
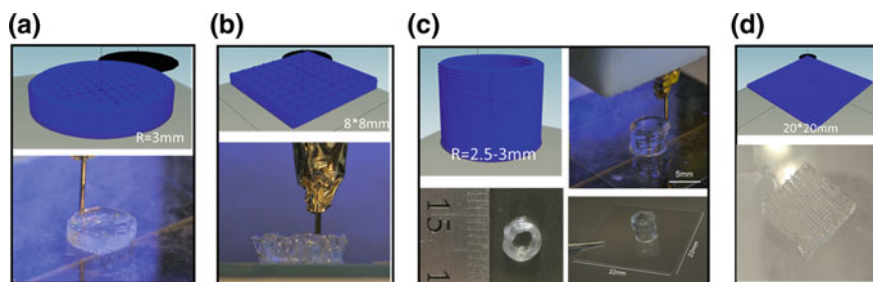
Fig. 4.14 Representative images of 3D-printed constructs using 5 wt% DC hydrogel, **a** cylinder, **b** cubic, **c** tube, and **d** sheet. Reproduced, with permission from [2]
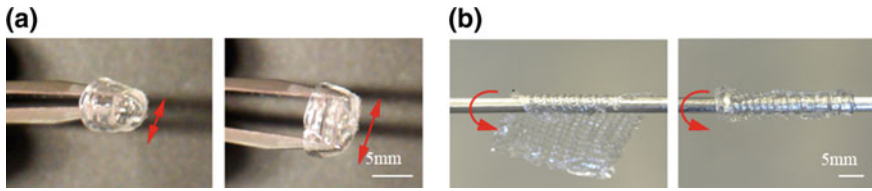
Fig. 4.15 Mechanical properties of 3D-printed **a** tube and **b** sheet structure with stretching and folding demonstrations, respectively. Reproduced, with permission from [2]

4.2.2   Structure Stabilization

Various post-stabilization protocols were investigated to further enhance the stability of the printed structures (Table 4.1). When structures were treated with UV light for 5 min under ambient air and subsequently placed into PBS—the first stabilization protocol, SP-1—changes in the structure were observed over time (Fig. 4.16). It is well known that the conditions for free radical-induced polymerizations are critical to the formation of covalent bonds throughout the hydrogel [8]. Specifically, oxygen competitively reacts with the radicals generated by the photo-initiator (I2959) that are needed to propagate the polymerization. In this case, light exposure in ambient air might not have induced complete crosslinking throughout the structures, which com-

Table 4.1 Parameter configurations for post-stabilization protocols. Reproduced, with permission from [2]

Post-stabilization	In air (min)	In PBS (min)	0.05 wt% I2959 in PBS (min)
SP-1	5.0	–	–
SP-2	2.5	2.5	–
SP-3	2.5	–	2.5
SP-4	–	–	5.0
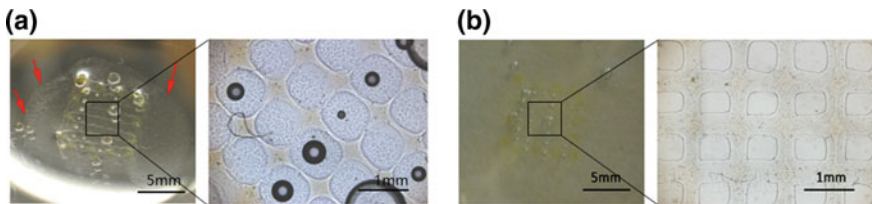
Fig. 4.16 Representative images of printed lattice structure after post-stabilization process **a** without (SP-1) and **b** with (SP-3) additional initiator. 5 wt% DC hydrogel was used

promised stability and led to erosion (Fig. 4.16). The similar results were observed
in structures treated with UV light first in the air and then after immersion in PBS for
2.5 min each (SP-2); however, any remaining initiator may have diffused from the
structure prior to the second round of light exposure, limiting any added stabilization.

When 0.05 wt% of the photo-initiator was included in the PBS during the second
2.5-min irradiation (SP-3), the lattice structure was observed to have clear edges
even up to one-month incubation. The fourth protocol (SP-4)—immersion in PBS
containing 0.05 wt% I2959 for the whole 5-min irradiation—also supported the
structure for one month. However, the filament sizes with this protocol (SP-4) were
significantly larger than that with SP-3. This was likely a result from relaxation of the
network or hydrogel swelling prior to the light irradiation. Thus, the SP-3 protocol is
believed to the best way to maintain printed bioink structure. The optical difference
between SP-1 and SP-3 could be easily identified in Fig. 4.17, where SP-3 group
present clear and standard lattice structure, while SP-1 presents expanded holes
and exude. Once covalently crosslinked, printed structures were stable over time,
with filament sizes (Fig. 4.18a) and mechanical properties (Fig. 4.18b) changing
little over a one-month incubation period. Specifically, from day 1 to day 30, the
compression modulus decreased from 15.7 ± 1.5 to 12.0 ± 0.6 kPa and from $20.8
\pm 2.0$ to 16.7 ± 1.9 kPa for samples printed with macromer concentrations of 5 and
7.5%, respectively (Fig. 4.18b). Furthermore, the optical images of a tubular structure
showed the excellent maintenance of structural integrity over time (Fig. 4.19).
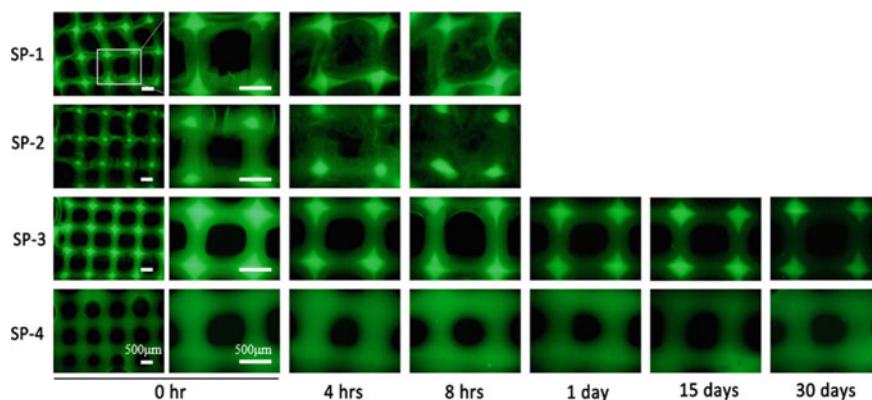
Fig. 4.17 Fluorescent microscope images of printed lattice structure up to one month during incu-
bation under different post-stabilization processes. 5 wt% DC hydrogel was used. Reproduced, with
permission from [2]
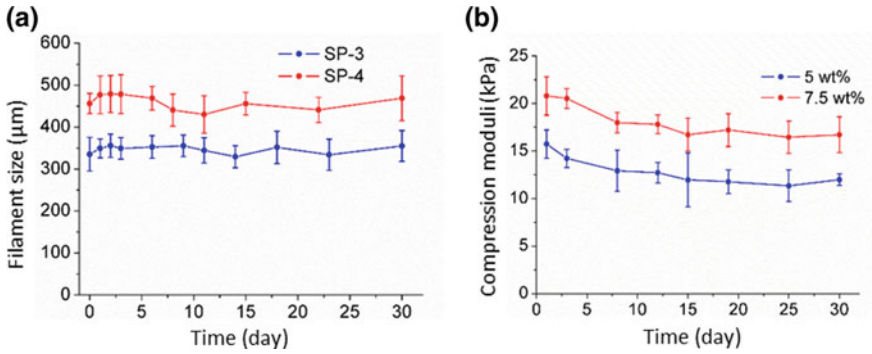
Fig. 4.18 **a** Quantified filament size of printed lattice structure after post-stabilization (SP-3 and SP-4) during one-month incubation. **b** Compression moduli of printed lattice structure under different concentrations (5 and 7.5 wt%) during one-month incubation. Reproduced, with permission from [2]
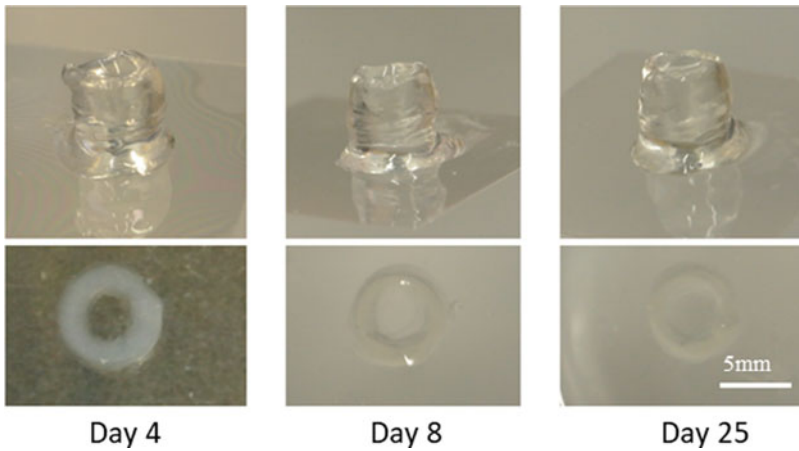

Fig. 4.19 Representative images of printed tubular structure (5 wt% DC) during incubation in PBS at 37 °C. Reproduced, with permission from [2]

4.3　Cytocompatibility

4.3.1　Cell Seeding

We firstly explored seeding NIH 3T3 cells on the printed DC scaffold by dripping dense cell suspension onto it. After one-day incubation, few cells attached on the scaffold, maintaining their viability very well (Fig. 4.20). To have a better cell adhesion, we modified the surface of the scaffold by incubating it in 2 mM peptide (GCGY*RGD*SPG) in TEOA (0.2 M) buffer at pH 8.0 overnight. This peptide contains an RGD sequence for cell adhesion and a cysteine residue which can conjugate
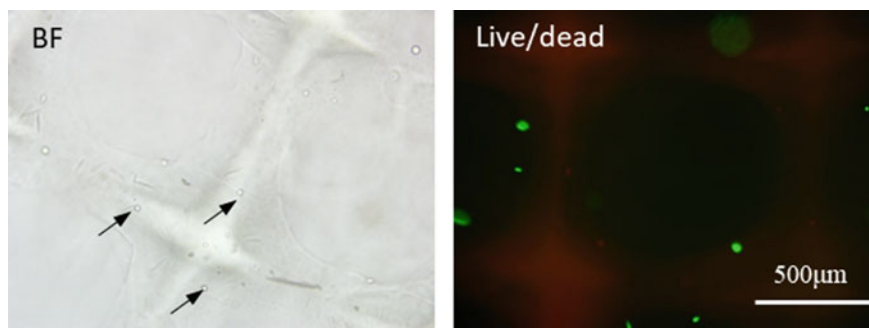
Fig. 4.20 Bright field and fluorescent images (LIVE/DEAD^{TM} staining at day 1) of printed lattice scaffolds (5 wt% DC) seeded with 3T3 cells
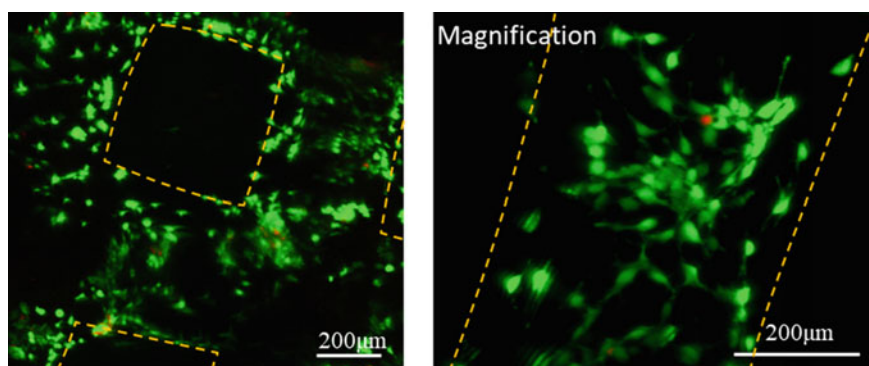
Fig. 4.21 Fluorescent images ((LIVE/DEAD^{TM} staining at day 5) of printed lattice scaffolds seeded with 3T3 cells, where the scaffolds (5 wt% DC) were modified with RGD peptides. Reproduced, with permission from [2]

with free methacrylate groups through Michael addition reaction. After modification, the scaffolds were washed with PBS and sterilized with UV irradiation. After seeding cells, we clearly observed the significantly enhanced cell attachment at day 5 (Fig. 4.21). Cells turned to be elongated and connected, which indicated the successful conjugation of RGD peptide.

4.3.2 Direct Cell Printing

For direct cell printing, we gently mixed cell suspension with sterile inks as indicated before and perform the usual 3D printing procedure. Specifically, we mixed cells with low-viscosity Ad-MeHA formulation first to better protect cells and then add in CD-MeHA formulation at the desired ratio. To better assess the effects of parameters on

cell viability, we monitored the cell viability at different stages (Fig. 4.22). The cells maintained high cell viability (>95%) before printing, which means the bioink preparation process was quite biocompatible. After printing, the cell viability decreased to ~70%, which might be induced by the UV treatment and extrusion shear force.

Here, we investigated the effects of UV irradiation on NIH 3T3 cells on 2D plastic. Under 2.5-min UV irradiation with varying intensities ranging from 2 to 20 mW/cm^2, similar cell viability was observed (Fig. 4.23). When controlling the intensity at 10 mW/cm^2, longer treatment (5 and 7.5 min) would induce slightly more dead cells (Fig. 4.24). It should be noted that the UV irradiation might induce further effects on cells, including DNA damage and phenotype change.

It is commonly agreed that shear force is one of the main reasons for cell damage in microextrusion bioprinting. This is confirmed in our studies when applying different
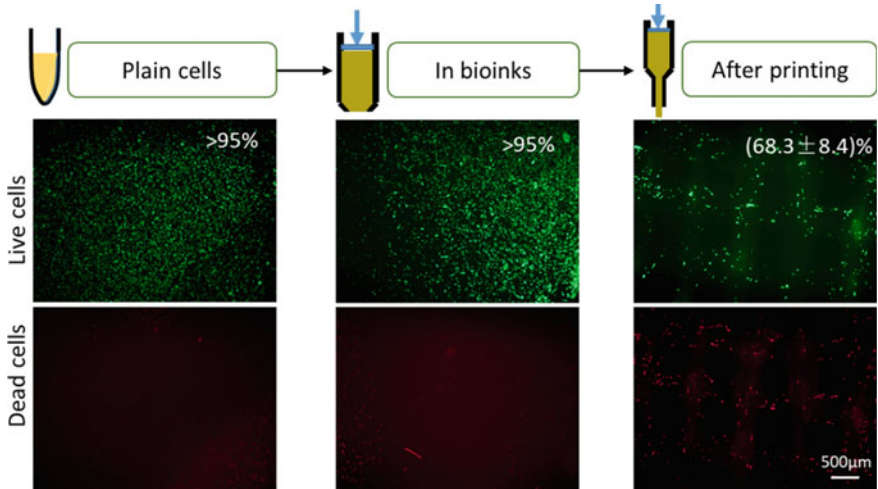
Fig. 4.22 3T3 cell viability at different stages from plain cell suspension, cell–hydrogel mixture to post-printing using 5 wt% DC bioink
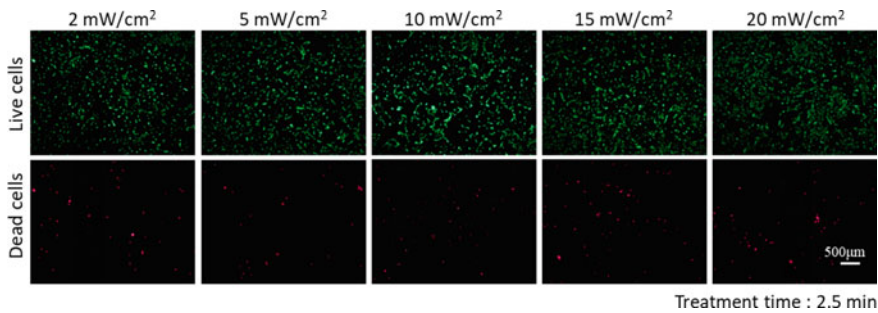
Fig. 4.23 Effect of UV intensity on 3T3 cell viability in 2D culture
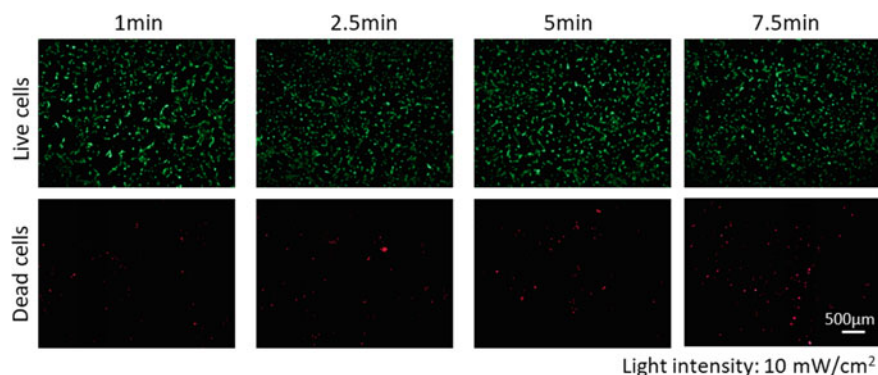
Fig. 4.24 Effect of UV treatment time on 3T3 cell viability in 2D culture

parameter configurations that would induce varied shear stress in the printing NIH 3T3 cells; maximum shear stress of ~1 kPa ends with ~75% viable cells while that of ~10 kPa ends with ~40% viability. The high stress is mainly induced by the high viscosity of the guest–host formulation, though a shear-thinning behavior might counteract the effects.

References

1. Rodell CB, Kaminski AL, Burdick JA (2013) Rational design of network properties in guest-host assembled and shear-thinning hyaluronic acid hydrogels. Biomacromolecules 14(11):4125–4134
2. Ouyang L, Highley CB, Rodell CB, Sun W, Burdick JA (2016) 3D printing of shear-thinning hyaluronic acid hydrogels with secondary cross-linking. ACS Biomater Sci Eng 2(10):1743–1751
3. Burdick JA, Prestwich GD (2011) Hyaluronic acid hydrogels for biomedical applications. Adv Mater 23(12):H41–H56
4. Highley CB, Prestwich GD, Burdick JA (2016) Recent advances in hyaluronic acid hydrogels for biomedical applications. Curr Opin Biotechnol 40:35–40
5. Rodell CB, MacArthur JW, Dorsey SM, Wade RJ, Wang LL, Woo YJ, Burdick JA (2015) Shear-thinning supramolecular hydrogels with secondary autonomous covalent crosslinking to modulate viscoelastic properties in vivo. Adv Func Mater 25(4):636–644
6. Bian L, Guvendiren M, Mauck RL, Burdick JA (2013) Hydrogels that mimic developmentally relevant matrix and N-cadherin interactions enhance MSC chondrogenesis. Proc Natl Acad Sci U S A 110(25):10117–10122
7. Gramlich WM, Kim IL, Burdick JA (2013) Synthesis and orthogonal photopatterning of hyaluronic acid hydrogels with thiol-norbornene chemistry. Biomaterials 34(38):9803–9811
8. Lim KS, Schon BS, Mekhileri NV, Brown GCJ, Chia CM, Prabakar S, Hooper GJ, Woodfield TBF (2016) New visible-light photoinitiating system for improved print fidelity in gelatin-based bioinks. ACS Biomater Sci Eng 2(10):1752–1762

Chapter 5
3D Bioprinting of Thermal-Sensitive Bioink

In this chapter, we aim to explore the property of a common thermal-sensitive bioink and its effects on structure printability and embryonic stem cells (ESCs) viability. Despite progress in bioinks development, the effect of bioink properties on the formation of 3D construct and cell damage during the extrusion process are poorly characterized [1, 2]. Moreover, the parameter optimization based on specific cell type might not be applicable to other types of cells, especially those with high sensibilities, such as ESCs. In this study, we systematically study the construct printability and cell viability in a temperature-controlled bioprinting process by using gelatin-alginate hybrid materials. A novel method is established to determine suitable conditions that could achieve both good printability and high cell viability. The rheological properties of the bioinks are evaluated to determine the gelation properties under different gelatin concentrations, testing temperatures and time. The printability of a lattice construct is characterized by using a semi-quantified method. The LIVE/DEAD^TM assay show that ESCs viability increased with the increase of printing temperature increased and decrease of gelatin concentration. Furthermore, a fitting exponential relationship was obtained between cell viability and induced shear stress. By defining the proper printability and acceptable viability range, a conjunction parameters region is obtained to guide the parameter choosing. This study will provide insight into the fine-tuning of 3D bioprinting process regarding the integrity of printed construct and incorporated cells, especially for easily damaged cells like ESCs.

Parts of this chapter have been published in Biofabrication [3, 4].

5.1 Bioink Preparation and Characterization

5.1.1 Preparation of Gelatin-Based Bioink

Gelatin undergoes a reversible gelation process in response to temperature; gelatin aqueous formulation with commonly used concentrations (e.g., 5–20 wt%) turns to

be a solution at 37 °C and form a gel when cooling down (e.g., <20 °C) [5]. Given this, a secondary crosslinking or component are usually introduced to preserve a stable structure under physiological condition. Here we use a hybrid bioink formulation containing gelatin and alginate, where the alginate could be ionically crosslinked in the presence of divalent cation (e.g., Ca^{2+}) (Fig. 5.1).

Each component was fully dissolved in water to prepare the stock solution, followed by a cyclic heating process for three times (at 70 °C for 30 min each time) for sterilization. The stock solutions (20 wt% gelatin and 2 wt% alginate) were stored at 4 °C until use. After warming up at 37 °C for 30 min, the two hydrogel stocks were mixed first and placed back to 37 °C to avoid any gelation, which was followed by adding the cell suspension gently in a certain ratio to get desired final concentration for each component. The stepwise mixing process was meant to protect cells better considering that the fast gelation of the bioinks might add to the difficulty of blending and thus induce higher cell damage. When directly mixing three components without any incubation in between, the cell viability (~93%) was slightly lower than that with incubation (~97%) (Fig. 5.2). This means the proposed bioink preparation protocol would maintain a higher cell viability.
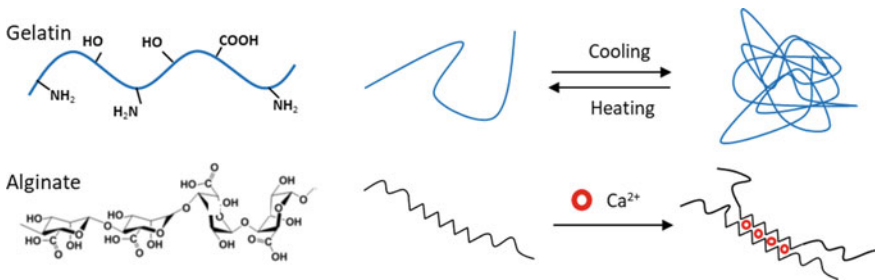
**Fig. 5.1** Schematic of the gelation mechanism of gelatin and alginate
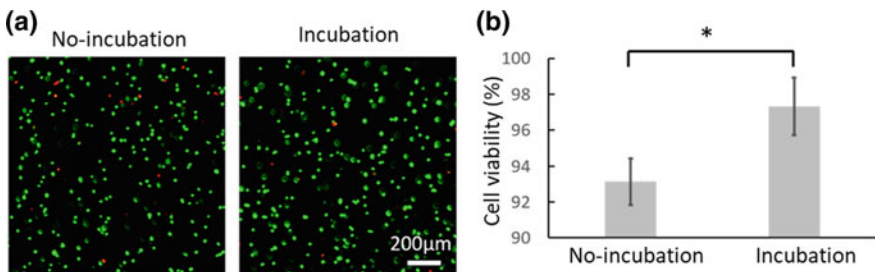
Fig. 5.2 The effect of incubation on mESCs viability when added to a bioink containing 7.5 wt% gelatin and 1 wt% alginate. Reproduced, with permission from [3]

## 5.1.2 Rheological Characterization

To clarify the response of each component to temperature, we performed an oscillatory temperature sweep test (cooling at 5 °C/min) for 7.5 wt% Gelatin (7.5% Gel), 1 wt% Alginate (1% Alg) and their mixture 7.5% Gel + 1% Alg. The viscosity of 1% alginate solution was fairly stable under different temperatures, while 7.5% Gel and 7.5% Gel + 1% Alg presented similar viscosity profile that the viscosity started to change dramatically between 20 and 25 °C (Fig. 5.3a). This demonstrated that gelatin was the core component that played as a thermal-sensitive role.

It should be noted that the rheological profile might differ between the cooling and heating process considering the different kinetics of gelation and melting. As we can see in Fig. 5.3b, the melting temperature (~33 °C) was higher than the gelation temperature (~24 °C) under the same temperate change ratio. This might also indicate the importance of the cooling or heating history the ink experiences. When performing a flow time sweep test starting from 37 °C, we found that, for different formulations, the storage and loss moduli both increased with time and turned to reach a plateau at some point (Fig. 5.4). The lower of the testing temperature, the faster it reached a gelation point, where G' surpassed G''. For example, it took about 1 min for 7.5% Gel + 1% Alg to form a gel at 22.5 °C, while it took ~15 min when setting at 27.5 °C. These results demonstrated that the time-dependence of gelatin-based bioink and would correspondingly affect the outcome of bioprinting.

To better understand the time-dependency, we define a gelation time (t_{gel}) as the time G' crosses G'', where the viscosity is defined as gelation viscosity (η_{gel}) (Fig. 5.5a). When setting at different temperatures, t_{gel} linearly corresponded to $1/T$ in logarithmic coordinate, which confirmed that lower temperature induced faster
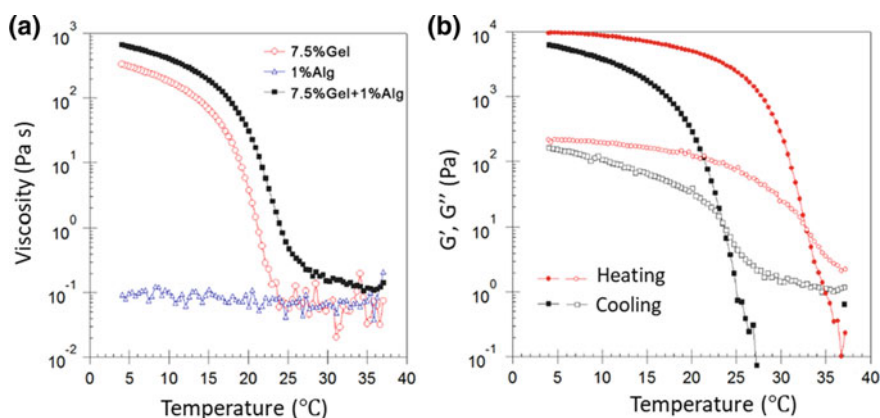
Fig. 5.3 **a** Viscosity profile under temperature sweeps (cooling at 5 °C/min) for 7.5% Gel, 1% Alg and 7.5% Gel + 1% Alg. **b** Storage and loss moduli responding to cooling and heating process for 7.5% Gel + 1% Alg inks. Strain 0.1% and frequency 1.5 Hz were used. Reproduced, with permission from [3]
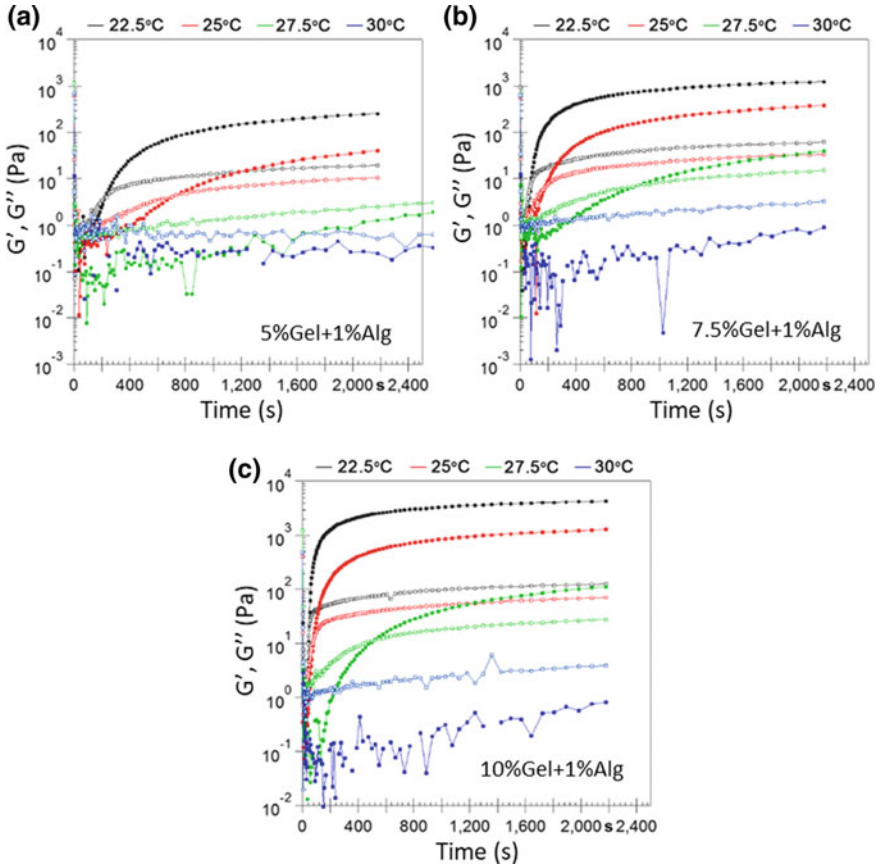
Fig. 5.4 Oscillatory time sweeps for **a** 5% Gel + 1% Alg, **b** 7.5% Gel + 1% Alg and **c** 10% Gel + 1% Alg under different temperatures. Strain 0.1% and frequency 1.5 Hz were used. Reproduced, with permission from [3]
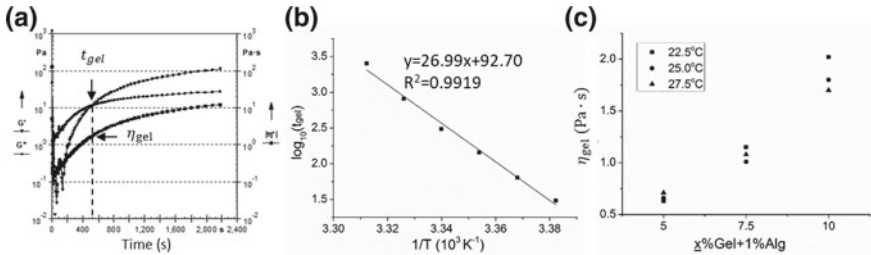
Fig. 5.5 **a** Determination of gelation time (t_{gel}) and gelation viscosity (η_{gel}) in an oscillatory time sweep test. **b** The relationship between t_{gel} and temperature (T). **c** The relationship between η_{gel} and gelatin concentration. Reproduced, with permission from [3]

gelation (Fig. 5.5b). This also meant that the temperature-dependent gelation property of gelatin-alginate bioink could be represented by an Arrhenius equation [6].

$$\ln\!\left(t_{\text{gel}}\right) = A + \frac{E_{\text{a}}}{RT} \tag{5.1}$$

where A is a constant, R is the ideal gas constant (8.314 J K^{-1} mol^{-1} of monomeric units), and T is the measurement temperature (K). According to Eq. (5.1), the activation energies (E_{a}) of 5% Gel + 1% Alg, 7.5% Gel + 1% Alg and 10% Gel + 1% Alg were 424.3, 353.5 and 350.6 kJ/mol, respectively. We also examined the relationship between bioink concentration and gelation viscosity, as shown in Fig. 5.5c. Interestingly, although the gelation kinetics varied with testing temperature, the η_{gel} remained at the same level when bioink concentration was constant, suggesting that the η_{gel} could act as an intrinsic property parameter representing bioink rheology. The gelation viscosity increased from 0.57 ± 0.04 to 1.84 ± 0.16 Pa·s when gelatin concentration increased from 5 to 10 wt% (Fig. 5.5c).

To assess the effect of cells on the bioink rheology, we added different densities of mESCs in the gelatin-alginate bioink. Generally, low cell density (1–2×10^6 cells/ml) did not significantly affect the viscosity, while high cell density ($>5 \times 10^6$ cells/ml) was likely to reduce the viscosity, regardless of the temperature (Fig. 5.6). This is probably because of the retention of crosslinking kinetics induced by encapsulated cells.
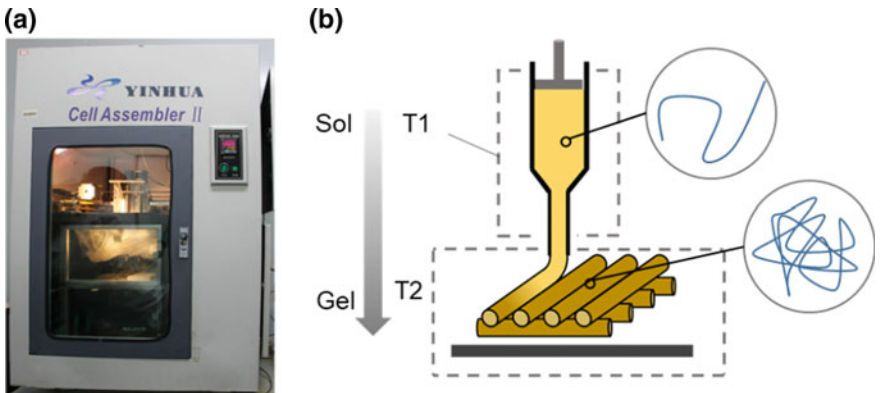
5.1.3 3D Bioprinting Process Design

The bioprinting of gelatin-alginate bioink is performed based on a highly incorporated 3D bioprinter (Cell Assembler, Tsinghua University), which allows for temperature control both in the nozzle the printing area (Fig. 5.7a). Basically, the nozzle is controlled at a specific temperature that allows for smooth extrusion, while the printing area is set at a lower temperature for quick gelation (Fig. 5.7b). To better optimize the bioprinting process, we followed a study route as shown in Fig. 5.8, where the rheological characterization and bioprinting practice were performed in parallel. After gentle mixing of all components, the bioink was incubated in the incubator at 37 °C for 30 min before going to the rheometer and the printer. The rheometer was set at an initial temperature of 37 °C to make sure the ink stayed in a consistent solution status, while the testing temperature for time sweep was set at a range of temperatures, including 22.5, 25.0, 27.5 and 30.0 °C. Correspondingly, the printer nozzle was set at the same temperature configurations after immediately loading the bioink from 37 °C incubator. The printing area was set at 22.5 °C as constant. After printing, the printed construct was placed in 1% CaCl$_2$ solution for 3 min for ionic crosslinking, followed by 37 °C incubation.
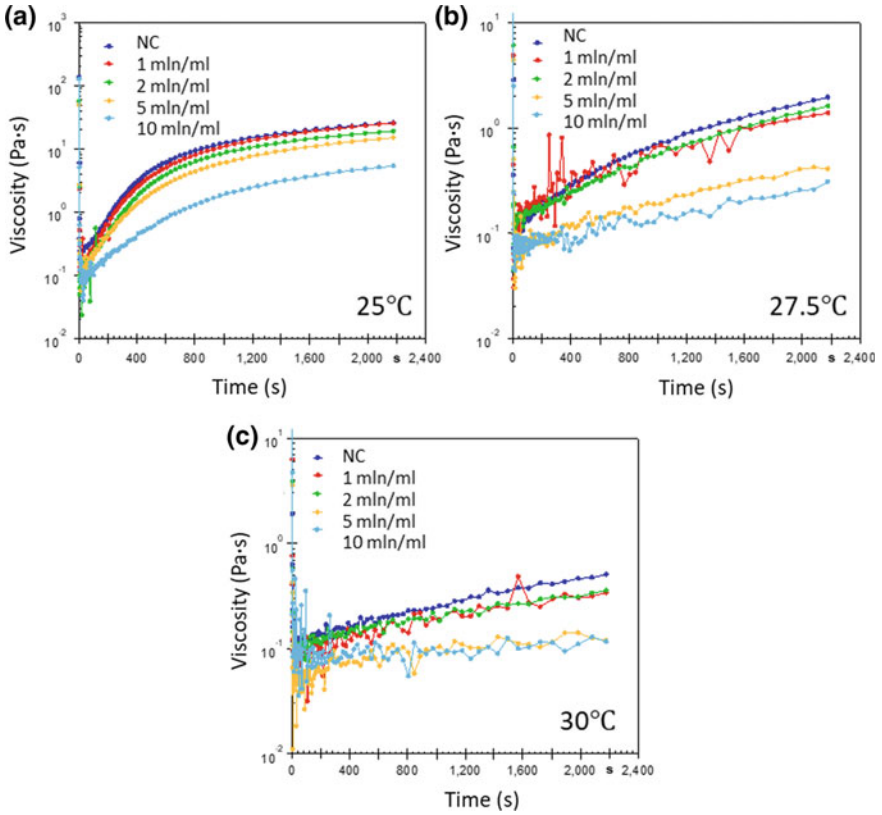
Fig. 5.6 Continuous flow test of inks embedded with different densities of mESCs under different temperatures. mln/ml = 10^6 cells/ml. Reproduced, with permission from [3]

Fig. 5.7 a The 3D bioprinter (cell assembler) with temperature-controlled nozzle and printing chamber. **b** The schematic of the bioprinting process with temperature controls, driving the sol-gel transition during extrusion
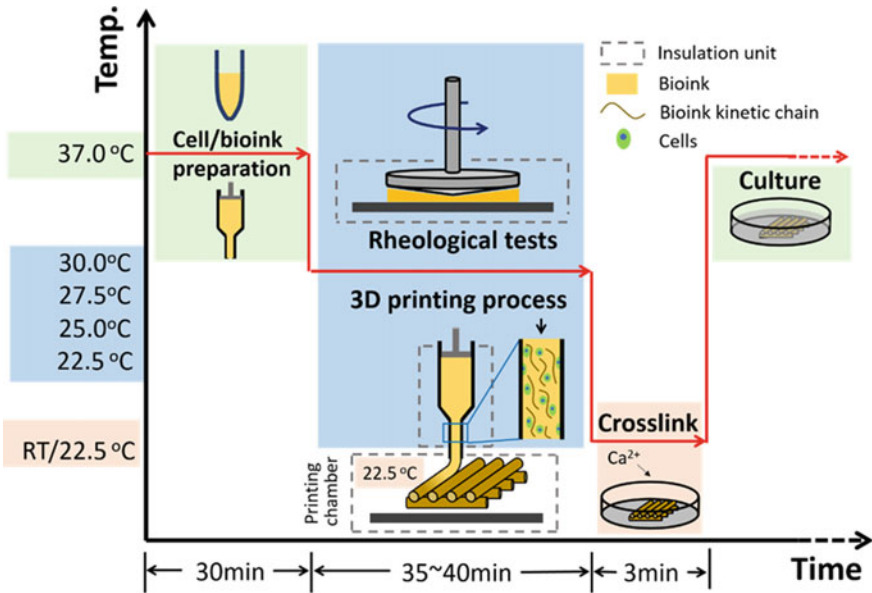
Fig. 5.8 Schematic of study route with rheological characterization and 3D printing process in parallel. Reproduced, with permission from [3]

5.2   Printability and Stability

5.2.1   Gel Filament Generation

There are generally three types of extrusion status corresponding to the gelation degree of the bioink, which includes under-, proper-, over-gelation (Fig. 5.9). Under-gelation indicates a sol property, and the bioink turns to hang on the needle tip as a liquid drop. Over-gelation would result in gel fracture and end with irregular gel filament. Proper-gelation means an in-between status, where the bioink can be extruded into a smooth, standard gel filament. It is desired to present a proper-gelation status during printing.

5.2.1.1   3D Structure Fabrication

To assess the 3D printability, we printed the inks into a lattice structure. Ideally, the alternatively deposited filament layers would form standard rectangular pores as stated in Chap. 3. Here, we capture the microscope images of printed structures (2 layers) at different time points. Based on the method described in Sect. 3.4.3 and corresponding image analysis, we could obtain the Pr values under different conditions. Basically, lower temperature and higher gelatin concentration would
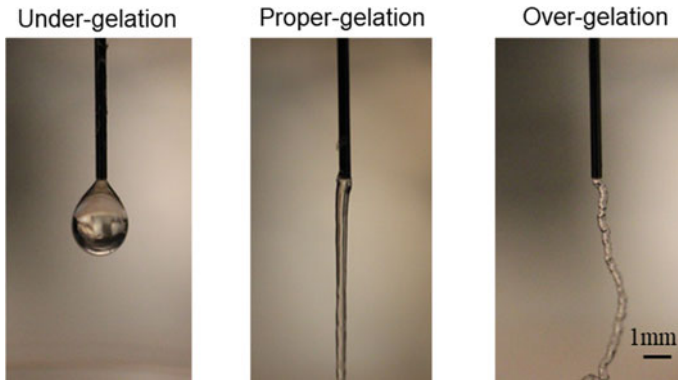
Fig. 5.9 Representative images of ink extrusion, indicating three different gelation status. Reproduced, with permission from [3]

result in higher Pr value (Fig. 5.10). It is noted that the structure turns to be uniform and wrinkled when it presents too higher Pr (e.g., >1.1), while that with too low Pr (e.g., <0.9) turns to be indistinguishable between layers although the overall pattern looks uniform. The structures with Pr value around 1 present uniform and standard pores as designed. Thus, we define a threshold for desired Pr value between 0.9 and 1.1, which will be used to filter the conditions regarding 3D printability.

The printability profile during a time frame of 40 min printing can be found in Fig. 5.11 under different conditions. For 5% Gel + 1% Alg bioink, the Pr value was relatively consistent with time, and 25 °C of nozzle temperature was likely to induce proper Pr within the rage of 0.9–1.1, while higher nozzle temperatures (27.5 and 30 °C) would result in lower Pr (<0.9) (Fig. 5.11a). Referring to the 7.5% Gel + 1% Alg bioink, 27.5 and 30 °C were proper printing temperatures during the whole holding process, while 25 °C would result in over-gelation condition after 10 min (Fig. 5.11b). These results suggested that when the printing temperature was set at 25 °C for the 7.5% Gel + 1% Alg bioink, the printing process must be completed within 10 min to avoid over-gelation. Moreover, this time window is impractical when many constructs, or a construct with large volume, must be printed. As to the 10% Gel + 1% Alg bioink, the Pr increased over time at different printing temperatures. When the printing temperature was 25 and 27.5 °C, the Pr was higher than 1.1 regardless of time, suggesting an over-gelation condition (Fig. 5.11c). Such printability profiles could act as guidelines for parameters optimization.

Based on the printability profile, there are three parameter configurations that would deliver consistently proper printability during 40 min printing: 5% Gel + 1% Alg at 25 °C, 7.5% Gel +1% Alg at 27.5 and 30 °C. Here we used 7.5% Gel + 1% Alg bioink as an example and printed constructs at 30 °C (Fig. 5.12). Well-defined 2D pattern and 3D lattice structures were presented with good integrity. The SEM images of freeze-dried lattice structure clearly indicated the multi-scale pores generated by the printing pattern and hydrogel itself, ranging from hundreds to several microns (Fig. 5.13).
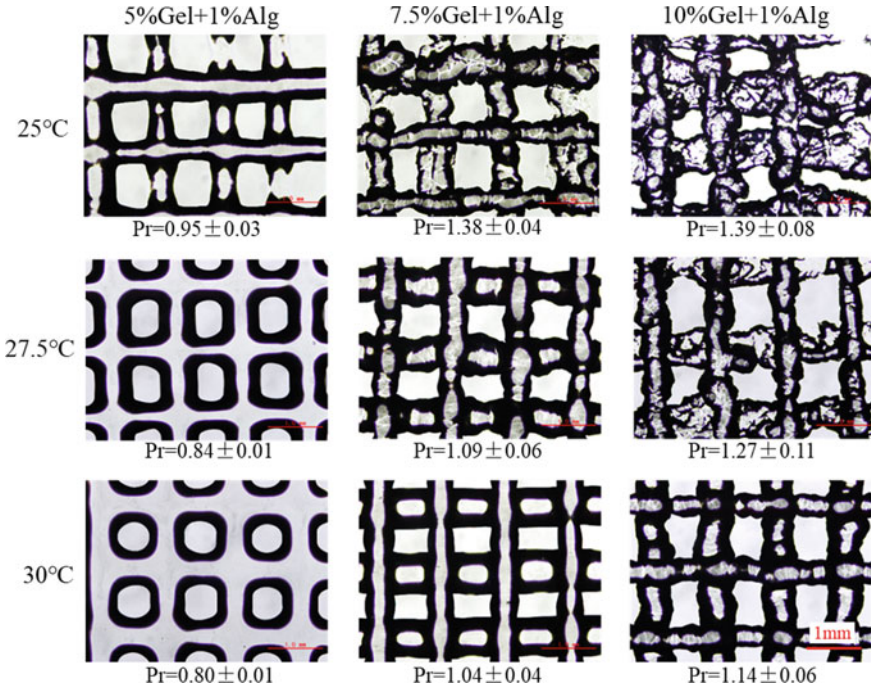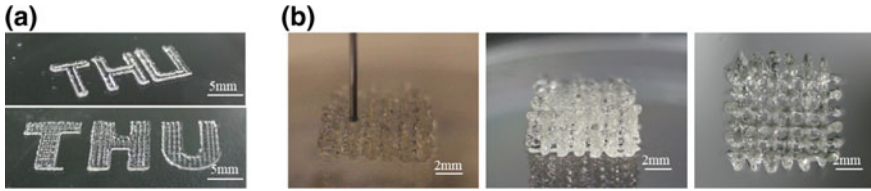
Fig. 5.10 Representative images of 3D printed lattice structure (2 layers) at 30 min under different parameter configurations. The quantified Pr values are indicated below the corresponding figure. Reproduced, with permission from [3]
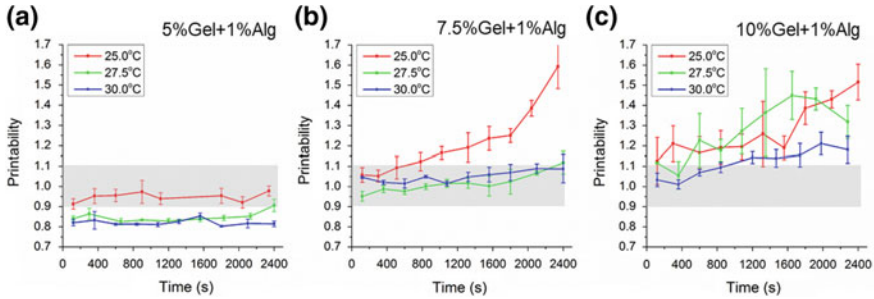

Fig. 5.11 Printability profile with time under different nozzle temperatures for **a** 5% Gel + 1% Alg, **b** 7.5% Gel +1% Alg and **c** 10% Gel +1% Alg. Reproduced, with permission from [3]

The previous optimization clearly clarifies the relationship between printability and individual parameter, while it is still unknown how the relationship is determined. Given this, we seek to explore the gelation parameters that would directly affect the printability. During the extrusion process, bioinks experienced the temperature change from nozzle (printing temperature) to chamber (room temperature of 22.5 °C

Fig. 5.12 Representative images of printed **a** "THU" logo and **b** 3D lattice structure using 7.5% Gel + 1% Alg bioink at 30 °C. Reproduced, with permission from [3]
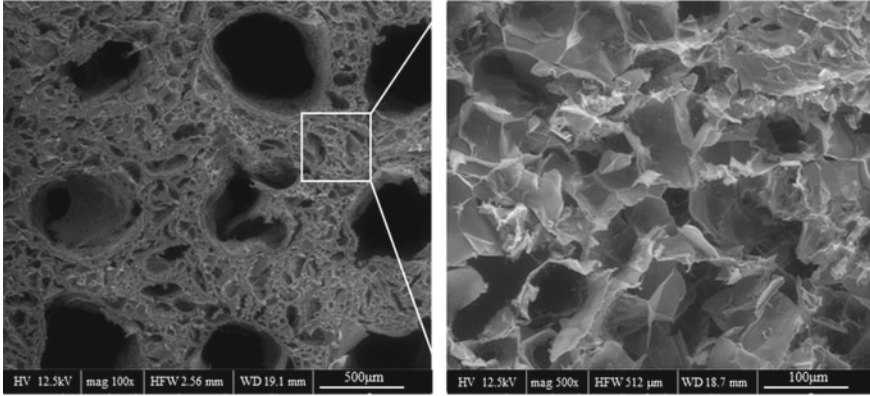

Fig. 5.13 SEM images of a freeze-dried lattice structure printed from 7.5% Gel + 1% Alg bioink at 30 °C. Reproduced, with permission from [4]

in this study). The kinetics of bioink gelation through the temperature cycle were studied (Fig. 5.14a). The bioink responded quickly to the decrease of temperature and initiated gelation from a sol-like status. However, it would take a certain time for the bioink to reach gelation point, where G' surpass G''. Here we define this time as Δt_{gel} (Fig. 5.14b). Figure 5.14c showed the relationship between printability and the ratio $\Delta t_{gel}/\Delta t_{layer}$, where Δt_{layer} is the time for printing each layer. The results indicated that when the ratio $\Delta t_{gel}/\Delta t_{layer}$ was less than 1, the Pr value was above 0.9. This means that under-gelation would occur when the next layer is initiated before the previous ink form a proper gel. Thus, $\Delta t_{gel}/\Delta t_{layer}$ would be a key reference that should be considered before printing.

5.2.2 Structure Stability

The structure was further maintained by the ionic crosslinking of alginate, while the gelatin was likely to diffuse out at 37 °C because of the reversible sol-gel transition. When incubating an acellular construct (10 × 10 × 3 mm) at 37 °C, the struc-
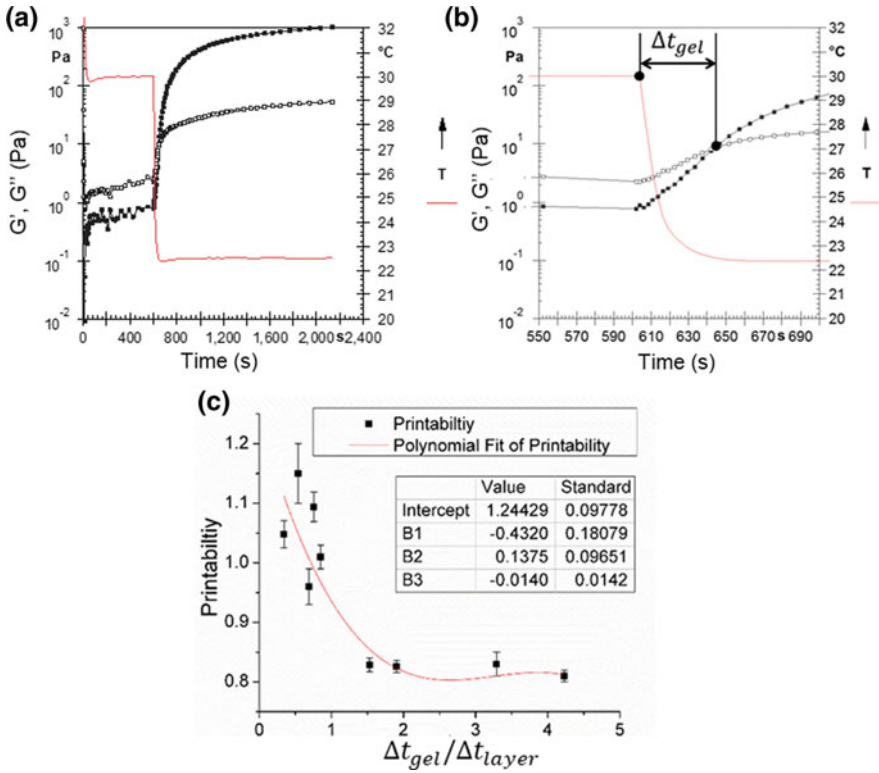
Fig. 5.14 **a**, **b** Determination of gelation time (Δt_{gel}) under a sharp temperature transition condition for 7.5% Gel + 1% Alg bioink. **c** The relationship between printability and $\Delta t_{gel}/\Delta t_{layer}$, where Δt_{layer} indicates the time for printing each layer. Reproduced, with permission from [3]

tural integrity was well maintained for up to one week (Fig. 5.15a), after which a yield loading of 5 N was measured. In contrast, the cell-laden constructs (containing 1×10^6/ml C2C12 cells) collapsed significantly and lost the lattice pattern during culture (Fig. 5.15b). This probably means the faster degradation of Ca^{2+}-Alginate network in the presence of cells. A compression test was performed on the cell-laden constructs to better characterize the mechanical properties. Generally, the constructs compromised in the mechanical properties with culture time: at day 0, the yield stress was ~20 kPa, while that at day 1 was only ~4 kPa (Fig. 5.16). It should be noted that adding additional Ca^{2+} during culture would enhance the structure integrity and mechanical properties [7].
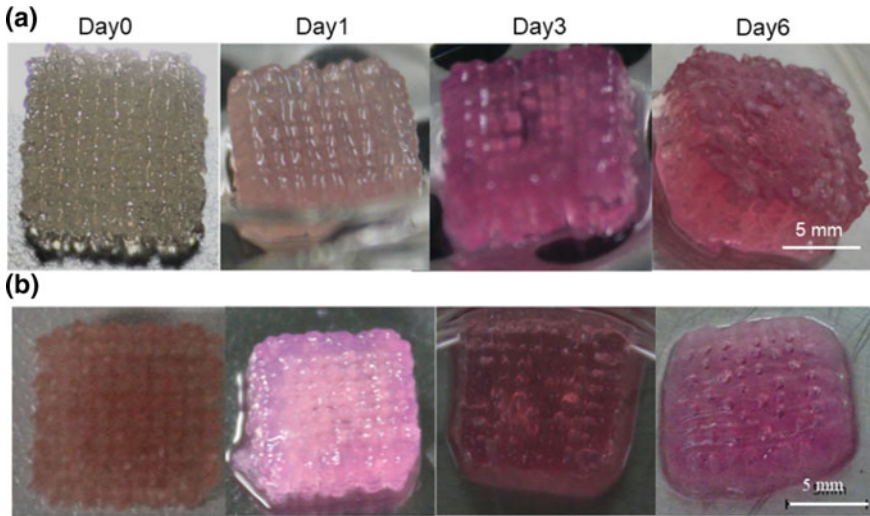
Fig. 5.15 Structure integrity of **a** acellular constructs and **b** C2C12-encapsulated constructs during one-week culture. 7.5% Gel + 1% Alg bioink was used. Reproduced, with permission from [4]

5.3 Cytocompatibility

5.3.1 Cell Viability of Different Cells

As commonly used biomaterials in biomedical applications, gelatin and alginate enjoy excellent biocompatibility. However, the bioprinting process might introduce some factors that could compromise the cell viability as described in Chap. 3. Though the gelatin/alginate bioinks have been applied in the bioprinting of cancer cells, fibroblasts and endothelial cells [8–10], there is little knowledge on the difference among varied cell types. To address this question, here we applied the same printing parameters (7.5% Gel + 1% Alg, 22.5 °C) in printing Hela, C2C12 and mESCs and performed the LIVE/DEAD^{TM} staining (Fig. 5.17). Hela cells preserved high cell viability of ~90%, while the other two cell types presented much more dead cells, especially for the mESCs (viability ~15%). These results clearly demonstrated the different tolerance against printing process for different cells. This also means that the optimized parameters based on robust cell type (e.g., cancer cells) might not fit other cells (e.g., embryonic stem cells). Here we will use the mESCs as the model cells for cell viability study.
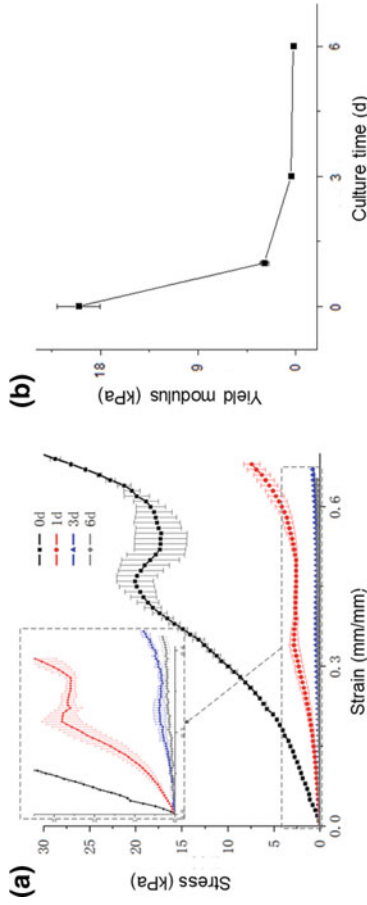
Fig. 5.16 a The stress-strain curves and **b** yield stress of cell-laden constructs (7.5% Gel + 1% Alg) at different time points. Reproduced, with permission from [4]
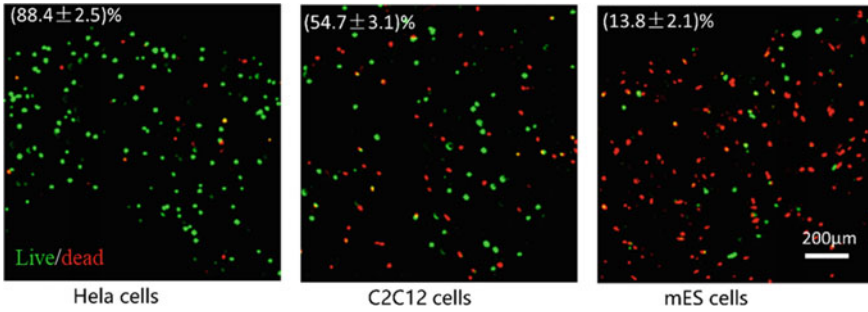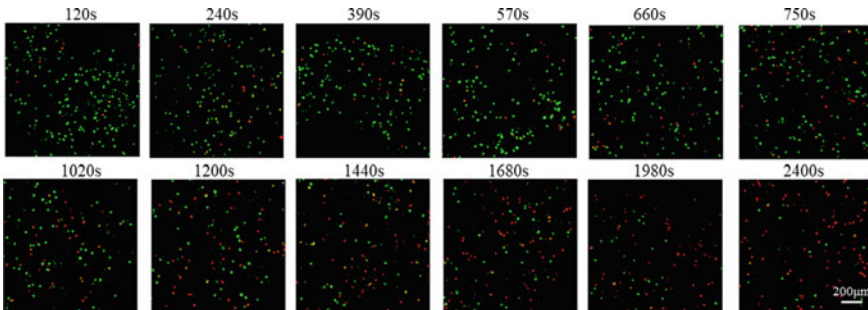
Fig. 5.17 Representative LIVE/DEAD^{TM} staining images of Hela, C2C12 and mES cells after printing with the same parameters using 7.5% Gel + 1% Alg bioink. Reproduced, with permission from [3]

5.3.2   Effect of Printing Parameters

Similar to the 3D printability study, here we monitor the cell viability at different time points. When printing 7.5% Gel + 1% Alg bioink at 22.5 °C, dead cells were found to increase over time (Fig. 5.18). By quantifying the cell viability under different conditions, we could obtain the viability profiles as shown in Fig. 5.19. Generally, cell viability decreases over time, and this would be compounded with lower temperature and higher bioink concentration. Three parameter configurations were found to yield consistently high cell viability (>90%) throughout a 40-min printing process: 5% Gel + 1% Alg, 30 °C; 5% Gel + 1% Alg, 27.5 °C; 7.5% Gel + 1% Alg, 30 °C.


Fig. 5.18 Representative LIVE/DEAD^{TM} staining images of mESCs post printing at different time points. Printing was performed using 7.5% Gel + 1% Alg bioink at 22.5 °C. Reproduced, with permission from [3]
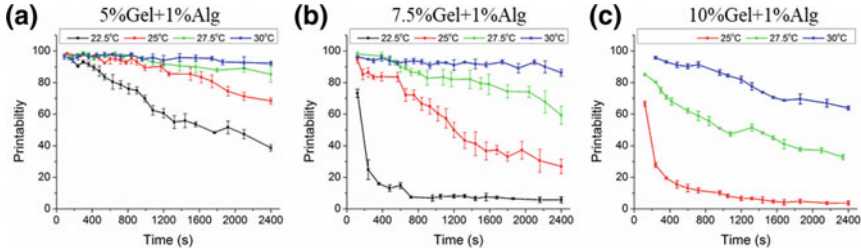
Fig. 5.19 Quantified cell viability profile with time under different bioink concentration and temperature configurations. Reproduced, with permission from [3]

5.3.3 Effect of Shear Stress

It is widely believed that shear stress on cells during extrusion would result in major cell damage [11]. Any factors that could contribute to the viscosity would result in higher shear stress, taking polymer concentration and temperature for examples. Based on the described method in Chap. 3, we estimated the maximum shear stress on cells and plot all the data points under comprehensive conditions (bioink concentrations, temperature, and time) in one figure (Fig. 5.20). It indicated a clear trend that cell viability decreased with shear stress following an exponential fitting curve. To obtain a cell viability of >90%, the maximum shear stress should be controlled under ~100 Pa.
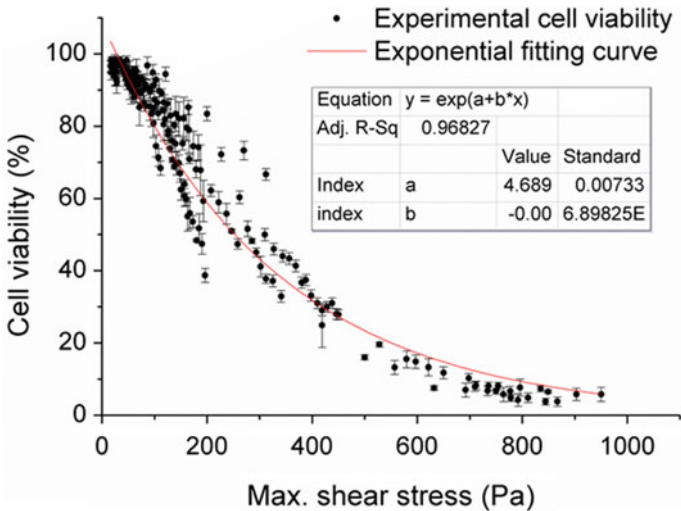

Fig. 5.20 The change of cell viability with maximum shear stress. Data were obtained from comprehensive conditions. Reproduced, with permission from [3]

Such curve revels the importance of shear stress control and could be used as a reference for parameter optimization. It should be noted that this curve would be cell-dependent and might only apply to the cells (mESCs) studied.

## 5.4 Conjunction of Structure Printability and Cell Viability

Both printability and viability are influenced by the three parameters considered, namely printing temperature, gelatin concentration and printing time, as stated above. We further studied the conjunction of printability and viability based on these original parameters. Figure 5.21a showed that higher gelatin concentration and lower printing temperature contributed to higher Pr value. For cell viability, however, lower gelatin concentration and higher printing temperature contributed to higher cell viability (Fig. 5.21b). At a certain time point (10 min), a correspondingly suitable region of gelatin concentration and printing temperature was generated to achieve suitable printability, where the Pr was in the range of 0.9–1.1 (Fig. 5.21c). Similarly, a suitable region of printing temperature and gelatin concentration was obtained when the minimum value of cell viability was set at 90% (Fig. 5.21d).
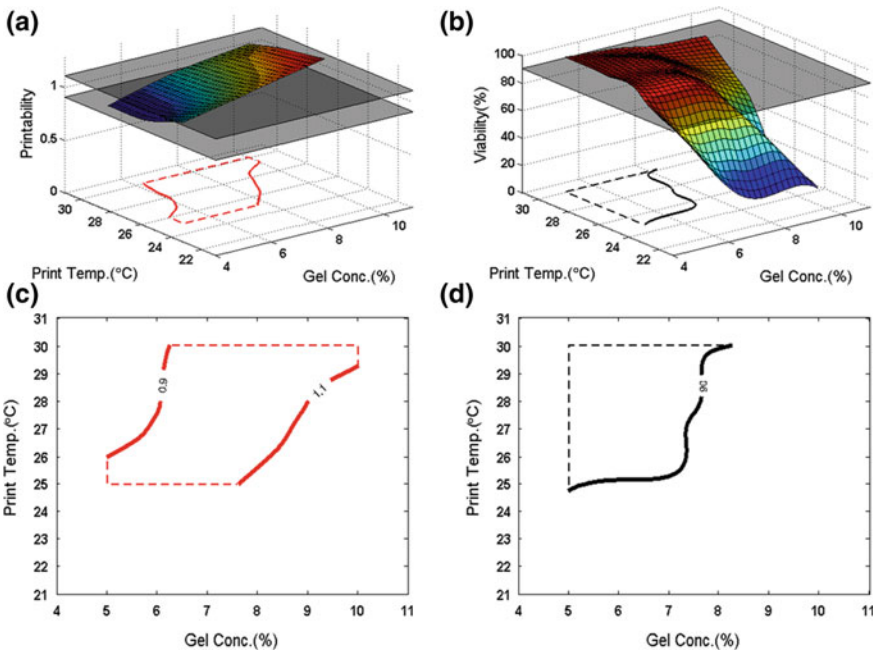
Fig. 5.21 Profile of **a** printability and **b** cell viability and **c**, **d** the optimization of parameter regions. Time point: 10 min. Reproduced, with permission from [3]
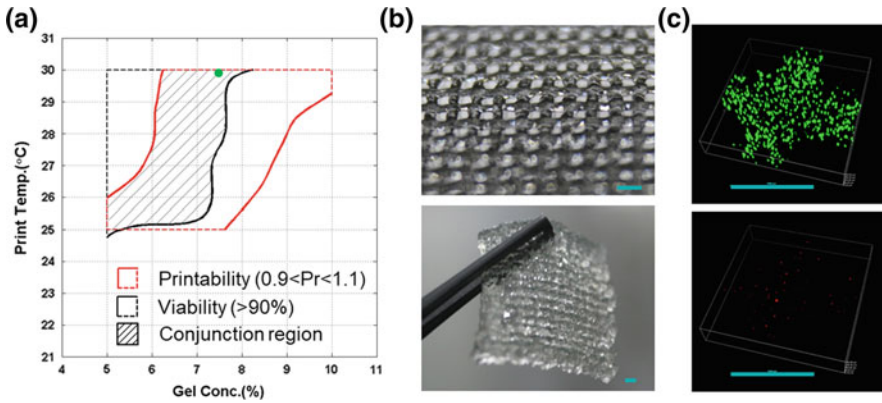
Fig. 5.22 **a** Conjunction of regions optimized for printability and viability. **b** Representative images of printed lattice structure and **c** LIVE/DEAD^{TM} staining images using the optimized parameters: 7.5% Gel + 1% Alg at 30 °C. Reproduced, with permission from [3]
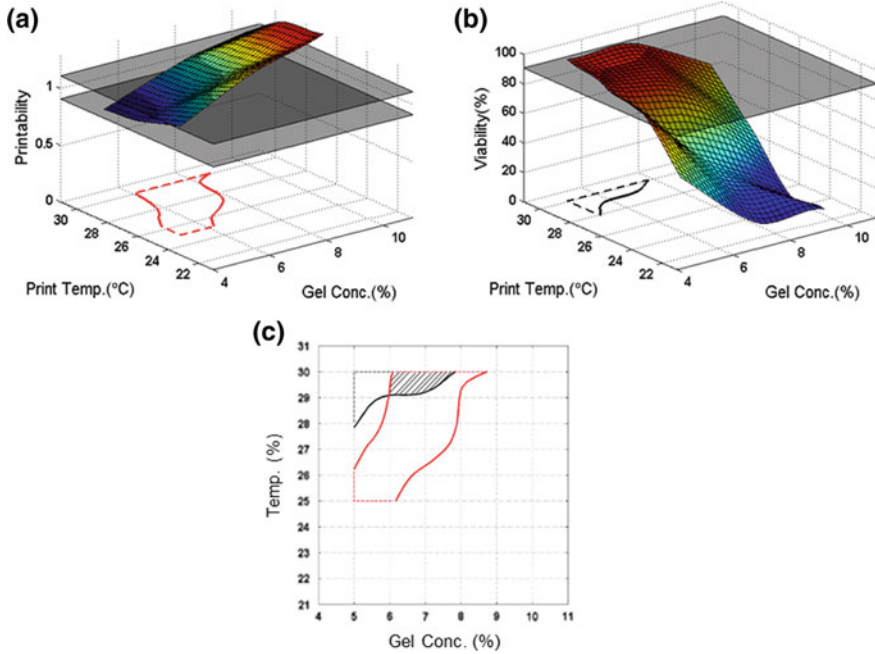
Fig. 5.23 Profile of printability and cell viability and the optimization of suitable regions. Time point: 30 min. Reproduced, with permission from [3]

Through combining these two regions generated for printability and cell viability, respectively, a conjunction region was obtained at the overlapped section (Fig. 5.22a). When applying a gelatin concentration of 7.5% and a printing temperature of 30 °C, which was within the conjunction region, standard multilayered structure (Fig. 5.22b) and very high cell viability (>95%) (Fig. 5.22c) were obtained. Specifically, it was demonstrated that the cell-laden construct showed high shape fidelity and clear contours and that mESCs were uniformly distributed in the hydrogel filaments.

It should be noted that the conjunction region varies with printing time. Figure 5.23 showed the chosen region at 30 min for printability, viability, and their conjunction, which was smaller than that at 10 min. Thus, 7.5% Gel + 1% Alg bioink at 30 °C should be a suitable parameter configuration for the consistent outcome during a bioprinting process up to 30 min. All these results together illustrate the time-dependency of gelatin-based bioinks in terms of both structural printability and cell visbility, which has never been discussed before.

References

1. Zhao Y, Li Y, Mao S, Sun W, Yao R (2015) The influence of printing parameters on cell survival rate and printability in microextrusion-based 3D cell printing technology. Biofabrication 7(4):045002
2. Pati F, Gantelius J, Svahn HA (2016) 3D bioprinting of tissue/organ models. Angew Chem Int Ed Engl 55(15):4650–4665
3. Ouyang L, Yao R, Zhao Y, Sun W (2016) Effect of bioink properties on printability and cell viability for 3D bioplotting of embryonic stem cells. Biofabrication 8(3):035020
4. Zhang T, Yan KC, Ouyang LL, Sun W (2013) Mechanical characterization of bioprinted in vitro soft tissue models. Biofabrication 5(4):045010
5. Nickerson MT, Patel J, Heyd DV, Rousseau D, Paulson AT (2006) Kinetic and mechanistic considerations in the gelation of genipin-crosslinked gelatin. Int J Biol Macromol 39(4–5):298–302
6. Fatimi A, Tassin JF, Turczyn R, Axelos MA, Weiss P (2009) Gelation studies of a cellulose-based biohydrogel: the influence of pH, temperature and sterilization. Acta Biomater 5(9):3423–3432
7. Wu Z, Su X, Xu Y, Kong B, Sun W, Mi S (2016) Bioprinting three-dimensional cell-laden tissue constructs with controllable degradation. Sci Rep 6:24474
8. Yan Y, Wang X, Pan Y, Liu H, Cheng J, Xiong Z, Lin F, Wu R, Zhang R, Lu Q (2005) Fabrication of viable tissue-engineered constructs with 3D cell-assembly technique. Biomaterials 26(29):5864–5871
9. Yao R, Zhang RJ, Yan YN, Wang XH (2009) In vitro angiogenesis of 3D tissue engineered adipose tissue. J Bioact Compat Pol 24(1):5–24
10. Zhao Y, Yao R, Ouyang L, Ding H, Zhang T, Zhang K, Cheng S, Sun W (2014) Three-dimensional printing of Hela cells for cervical tumor model in vitro. Biofabrication 6(3):035001
11. Nair K, Gandhi M, Khalil S, Yan KC, Marcolongo M, Barbee K, Sun W (2009) Characterization of cell viability during bioprinting processes. Biotechnol J 4(8):1168–1177

Chapter 6
3D Bioprinting of Non-viscous Bioink

As studied previously, bioinks are normally required to preserve certain viscosity to maintain the shape post-extrusion. Despite advances in bioink design, viscous bioinks can induce shear forces on cells during printing and compromise viability, and bioink design criteria toward printability severely limit material options and desired biochemical and biophysical properties. Thus, the balance between physical printability and biological functionality remains a challenge, for 3D bioprinting and new printing strategies are needed.

Photo-crosslinkable hydrogels have great potential as bioinks. These materials have been developed over the past few decades to encompass a wide range of properties, and they have been of significant interest for their applicability in cell encapsulation and tissue formation [1, 2]. Despite the plethora of photo-crosslinkable hydrogels under development in the biomaterials field, their application to bioprinting is hindered through their generally low initial viscosity and challenges in polymerizing fast enough to maintain printed structures [1]. To overcome this limitation, photo-crosslinkable hydrogels have been combined with polymers that gel through other mechanisms, such as with supramolecular assembly (Chap. 4), temperature, or exposure to ions [3–5]. This is not ideal, as it alters the material environment for cells. To address these challenges in printing photo-crosslinkable materials, here we present a generalizable bioprinting method to enable 3D printing of hydrogel structures from photosensitive precursors. In this approach, we introduce the light through a photo-permeable capillary (e.g., silicon tubing, glass) to crosslink the hydrogel immediately prior to leaving the needle and before deposition, which we termed in situ crosslinking. Advantages to this approach are (i) that it does not include any viscosity modulation or copolymerization with other polymers, (ii) that it can be generalized to different photo-crosslinkable hydrogel formulations, (iii) that it permits the encapsulation of viable cells, and (iv) that it can be used to print heterogeneous and complex structures.

Parts of this chapter have been published in *Advanced Materials* [6].

6.1 Strategy Optimization

6.1.1 Crosslinking Mechanisms

Methacrylated hyaluronic acid (MeHA) is used as an example of non-viscous photo-crosslinkable bioink. 5 wt% MeHA formulation presents typically low viscosity (~70 mPa s) and shear modulus (<1 Pa) with higher loss component (G'') than storage one (G') (Fig. 6.1). Under UV irradiation, both G' and G'' start to increase dramatically in the presence of photo-initiator (0.05 wt% I2959) and G' surpasses G'' within 1 min, both reaching the plateau within 5 min.

It is commonly believed that low-viscosity formulation would compromise the gel shape maintenance during printing. To process such bioinks, two crosslinking strategies are usually used: (1) pre-crosslink the formulation before printing to enhance viscosity; (2) post-crosslink the ink right after extrusion to achieve immediate gelation (Fig. 6.2a, b). Both strategies will be tested with the MeHA bioink. Moreover, we develop an entirely new strategy, in situ crosslinking, to address the possible challenges facing the previous two approaches (Fig. 6.2c).

For pre-crosslinking, the bioink is treated with 10 mW/cm^2 UV light for 10–30 s before loading to the cartridge. Generally, the longer of the UV irradiation, the higher of the shear modulus (Fig. 6.3). After 10-s irradiation, G' and G'' mixed with each other around 10 Pa without significant difference. With 20- or 30-s irradiation, the shear moduli increased significantly and G' was consistently higher than G'', indicating the gel formation (Fig. 6.3). We tested the direct printing of these pre-treated inks and found that 10-s irradiation ended up with liquid-like ink, while 20- or 30-s irradiation resulted in irregular gel filament (Fig. 6.4a). These results match quite well with the rheology: Pre-treatment of UV light for 20 s or longer would result in gel formation, which in return induce the irregular gel filament because of gel fracture during extrusion. Furthermore, the embedded cell viability with 20- and 30-s treatment was ~75 and ~50%, respectively, which are significantly lower than that with 10-s treatment (~90%) (Fig. 6.4b). The massive cell death might be caused by a combination of UV irradiation and shear stress induced by extruding viscous bioinks. Taken these, we found it was challenging to find an optimized pre-


Fig. 6.1 Rheological response of 5 wt% MeHA ink to UV light in the presence of a photo-initiator. The shaded area indicates UV irradiation. Reproduced, with permission from [6]
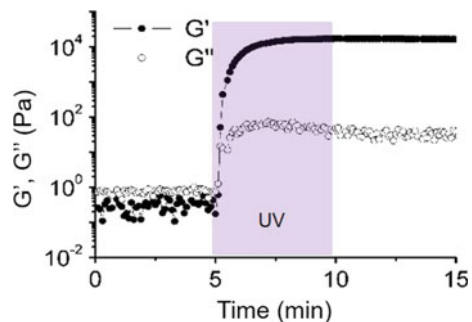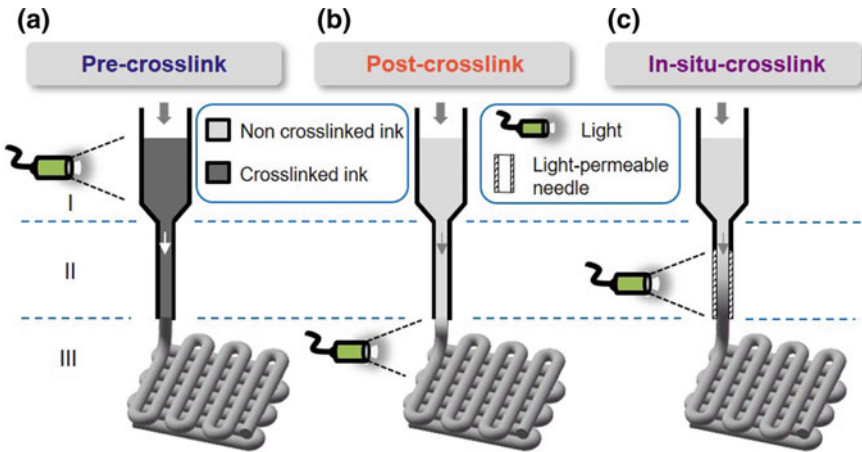
Fig. 6.2 Schematic of different crosslinking strategies for microextrusion bioprinting. **a** Pre-crosslink and **b** post-crosslink are usually used in literature, while **c** in situ crosslink is introduced in this study. Reproduced, with permission from [6]


Fig. 6.3 Oscillatory time sweeps of 5 wt% MeHA bioink with pre-treatment of UV irradiation (10 mW/cm^2) for 10, 20, and 30 s. Reproduced, with permission from [6]
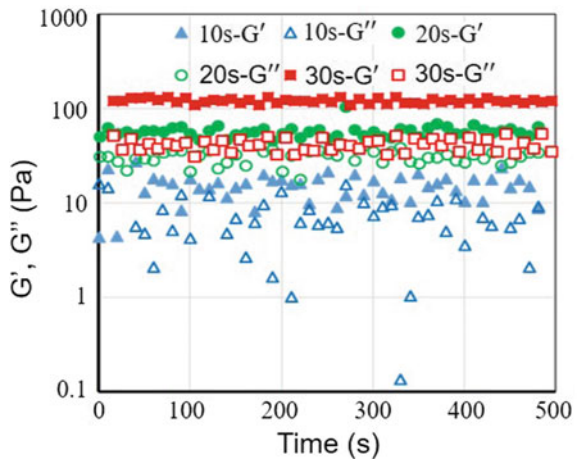
crosslinking condition that would both induce standard gel filament and maintain acceptable cell viability. Moreover, the possibly heterogeneous crosslinking network, which might affect the overall mechanical properties and cellular microenvironment in the final product, would be another concern with pre-crosslinking strategy.

As to post-crosslinking strategy, it has been demonstrated in Chap. 4 that MeHA formulation, even with up to 20 wt%, cannot be printed with good structure fidelity when immediately treating with UV light after extrusion. The main reason for this is that the bioink cannot be properly crosslinked before flowing away once extruded: It takes at least seconds for the bioink to form relatively strong crosslinked network
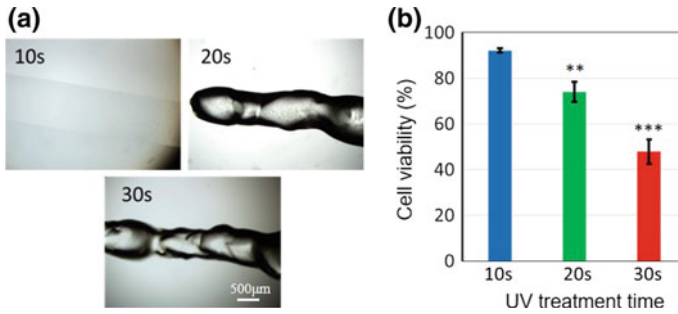
Fig. 6.4 **a** Representative images of printed filaments and **b** embedded cell viability with 5 wt% MeHA bioink pre-treated with different UV irradiation. Reproduced, with permission from [6]
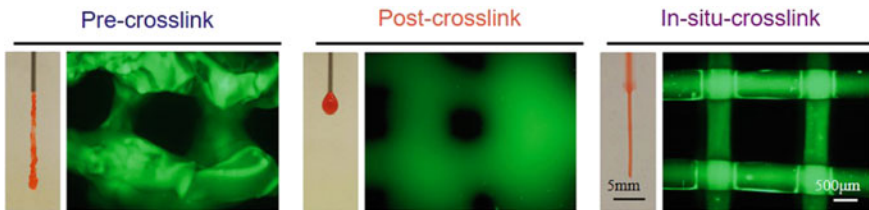

Fig. 6.5 Comparison of extrusion status and printed lattice structure via different crosslinking strategies. 5 wt% MeHA was used. Reproduced, with permission from [6]

(Fig. 6.1). Moreover, the oxygen inhibition for free radical polymerization with methacrylate groups might add to the collapse of the extruded inks.

To address these problems, we propose an in situ crosslinking strategy (Fig. 6.2c), where light is introduced through a light-permeable needle while bioinks synchronously go through it. We expect to see proper gelation of bioink before it comes out of the needle and thus gives rise to standard gel filaments for 3D construction. To illustrate this approach, we used silicone tubing as the special needle and applied UV light on the needle part. As a comparison, 5 wt% MeHA was printed into a lattice structure with all three strategies as shown in Fig. 6.5. Pre-crosslinking (30-s UV irradiation) resulted in ugly and non-uniform structure though gel filaments were demonstrated to be generated. Post-crosslinking ended up with a fused and deformed structure and the ink came out of the needle drop by drop. However, by applying the in situ crosslinking strategy, standard cylinder filaments are created and can be used to print uniform lattice structure with good integrity (Fig. 6.5). These results preliminarily illustrate the potential of the in situ crosslinking approach in maintaining good printability.

Furthermore, we tested the extrusion stability for different strategies (Fig. 6.6a). Generally, pre-crosslinking calls for the highest extrusion force (>2 N) while post-crosslinking calls for the lowest one (<1 N). Both post- and in situ crosslinking presents steady extrusion, while pre-crosslinking deserves a fluctuant extrusion pro-
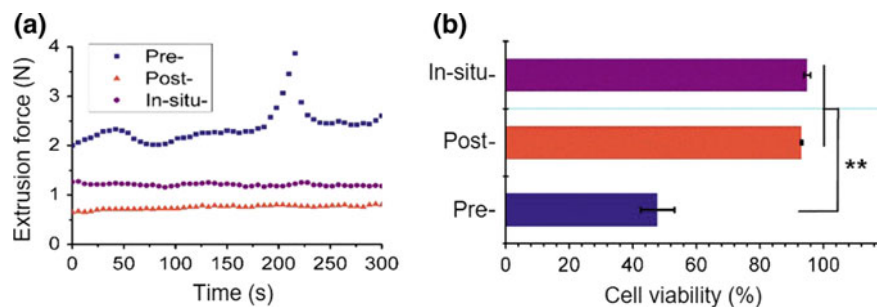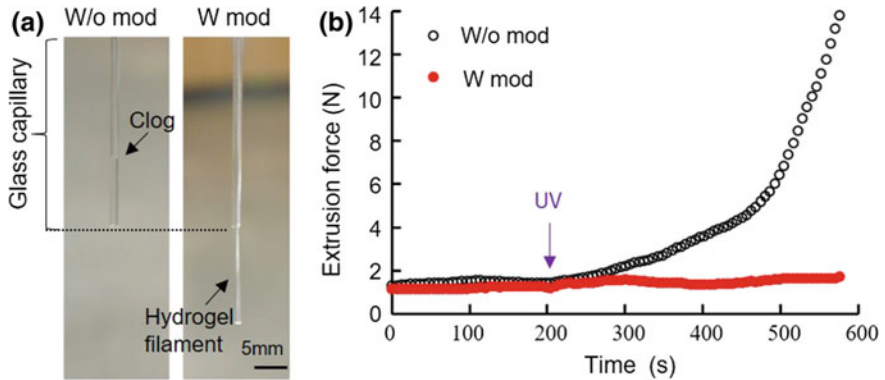
Fig. 6.6 **a** Extrusion force profiles and **b** embedded cell viability of different crosslinking strategies. 5 wt% MeHA is used. Reproduced, with permission from [6]

file. These results indicate the instability for extruding pre-crosslinking bioinks and confirm the smooth extrusion of in situ crosslinking approach. By embedding NIH 3T3 cells in the bioink formulation, we could compare the resulted cell damage among different strategies. Post- and in situ crosslinking preserve significantly higher cell viability (~90%) than pre-crosslinking does (~50%) (Fig. 6.6b). Taken all together, the in situ crosslinking strategy shows excellent potential in smooth extrusion, 3D printability, and living cells maintenance.
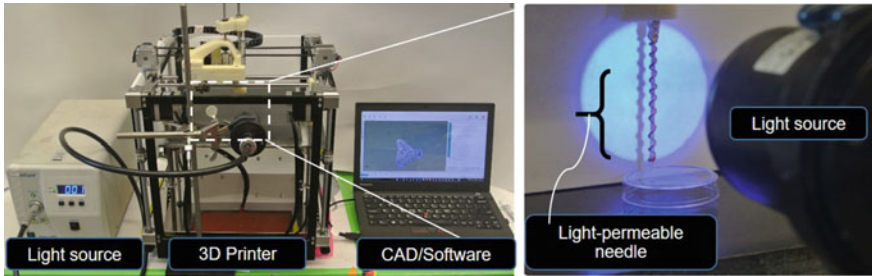
6.1.2 Light-Permeable Needle

There are two primary requirements for the modified needle: light-permeability and smooth resistance. Basically, a hydrophobic silicone tubing (Scientific Commodities) (~30 mm) with certain diameter was inserted into a standard disposable needle with a tight connection. A springlike copper holder was used to fix the tubing and to avoid any bending or deformation. Unless otherwise stated, such silicone tubing was used in the subsequent studies.

Alternatively, a typical glass capillary is possible to be used. It was found that unmodified glass capillary (Kimble Chase) would result in clog because of the strong resistance between the glass and formed gel inside (Fig. 6.7a). Moreover, the extrusion force was found to increase once the UV light was applied and to keep accumulating with time (Fig. 6.7b). Given this, we pre-treated the glass capillary with Rain-X for 10 min to modify the inner surface to be hydrophilic. By doing this, we obtained smooth gel filament generation, and the extrusion force was found to be steady during 10 min extrusion. These results demonstrated the feasibility of applying glass capillary in in situ crosslinking strategy after hydrophilic modification.

Fig. 6.7 **a** Representative images and **b** extrusion force profiles of extruding 5 wt% MeHA bioink through glass capillary with (W mod) or without (W/o mod) surface modification. Reproduced, with permission from [6]


Fig. 6.8 Printing setup with an in situ light source, 3D printer, and PC controller. The light source was introduced on the light-permeable needle during printing. Reproduced, with permission from [6]

6.1.3 Printing Setup

According to the designed in situ crosslinking strategy, here we built up a 3D printing setup based on a modified FDM 3D printer, which allowed for syringe loading and controlled extrusion. A UV light source (OmniCure S1500) was introduced to the modified needle via fiber optic (Fig. 6.8). The light was turned on once the printing started. The printing process was controlled by an open-source software (Repetier-Host) via G-code.

6.1.4 Printing Process

There are mainly three stages for the bioprinting process: in situ crosslinking for structure deposition, post-stabilization, and construct culturing (Fig. 6.9). By using the in situ crosslinking setup, non-viscous bioinks could be easily extruded through
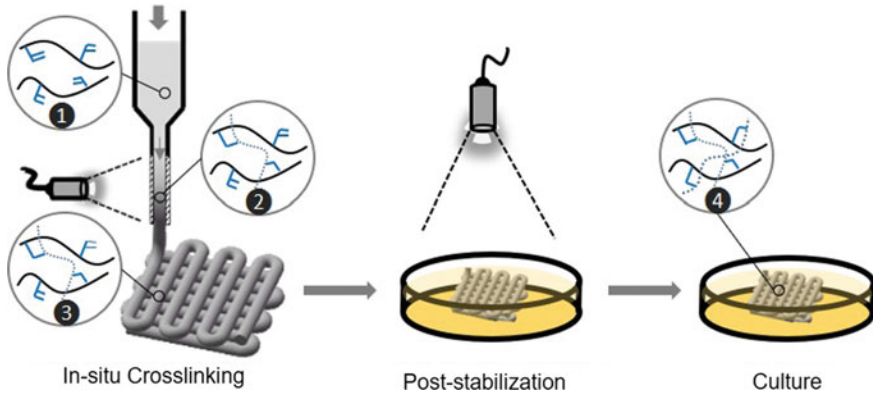
Fig. 6.9 Schematic of bioprinting process with in situ crosslinking strategy during extrusion. Reproduced, with permission from [6]

the modified needle and perform partial crosslinking simultaneously. Standard gel filaments are expected to be generated and deposited in a layer-by-layer fashion. After printing, the constructs are treated with additional UV irradiation for further stabilization, followed by culturing in cell incubator at 37 °C, 5% CO_2. Accordingly, the bioink would undergo different crosslinking status as shown in the inserts in Fig. 6.9: (1) non-crosslinked and non-viscous solution in the cartridge; (2) dynamic crosslinking in the needle; (3) partially crosslinked gel on the printing bed; (4) fully crosslinked gel in the incubator.

6.2 3D Printability and Stability

6.2.1 Gel Filament Generation

In addition to the preliminary illustration before, we seek to further study the filament generation. The smooth extrusion of filaments was firstly demonstrated: The filament length was highly linear to the extrusion time under steady extrusion (Fig. 6.10). To assess the effect of UV intensity on filaments, we designed a simple model of two lines with 2 mm distance (Fig. 6.11). No gel filaments were created with intensity lower than 1 mW/cm^2, where the deposited bioinks fused with each other. Under 5-mW/cm^2 irradiation, wave-shaped thin filaments were generated surrounded by liquid-like materials, which are likely to be uncrosslinked or less-crosslinked bioinks. The reason for the wave shape might be the mismatch between filament generation speed and printing speed. When using 10–20 mW/cm^2, standard filaments could be generated (Fig. 6.11), the size of which slightly increased with the intensity. Moreover, no more liquid-like bioinks were found around the filament when using high intensity (e.g., 20 mW/cm^2). This result meant that the crosslinking degree of the filaments could be controlled by changing the light intensity.
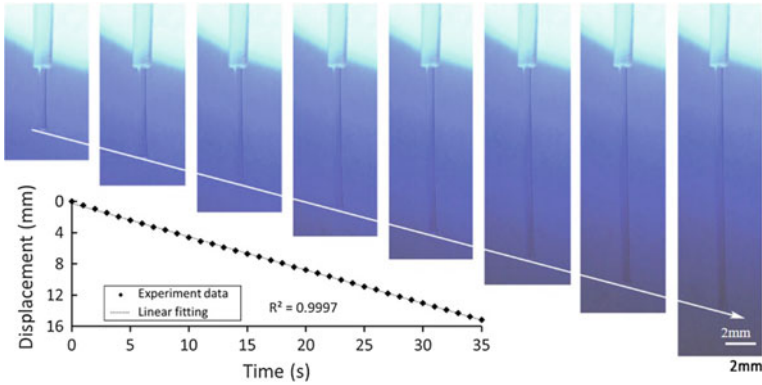
Fig. 6.10 Filament (5 wt% MeHA) generation through silicone tubing with in situ crosslinking. The insert figure indicated the displacement change with extrusion time. Reproduced, with permission from [6]
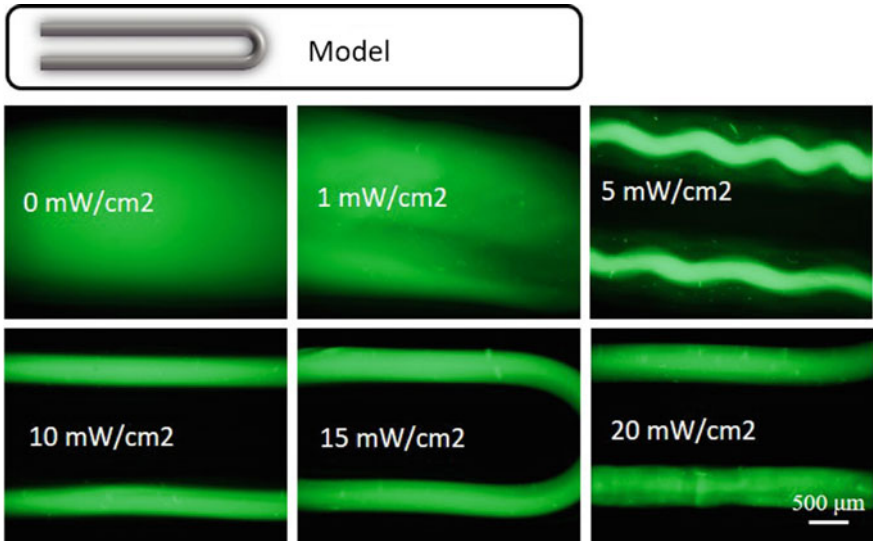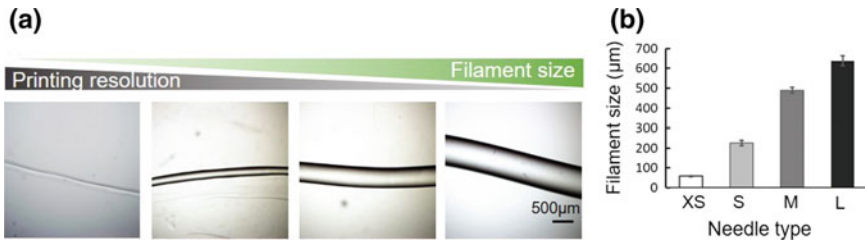

Fig. 6.11 Microscopy images of printed filaments (5 wt% MeHA) via in situ crosslinking with different UV intensity. Reproduced, with permission from [6]

The extrusion force measurement was performed to assess the extrusion stationarity: The force with 15 and 20 mW/cm^2 (~1.5 N) was higher than that with 1–10 mW/cm^2 (1.2–1.4 N) (Fig. 6.12). All the force profiles were relatively steady under different conditions, which illustrated smooth extrusion.

It is commonly believed that filament size is critical for printing resolution. In normal microextrusion printing of hydrogel materials, the filament size is comprehensively determined by the needle size, extrusion flux, and printing speed. In the case of in situ crosslinking approach, bioinks are pre-shaped in the needle and the
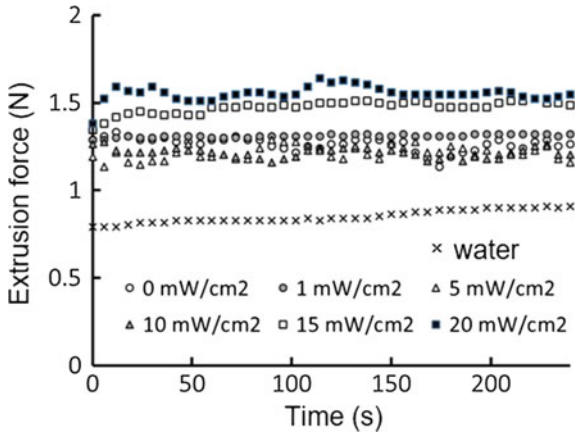
Fig. 6.12 Extrusion force profiles for extruding 5 wt% MeHA via in situ crosslinking with different UV intensities. Pure water was used as the control. Reproduced, with permission from [6]


Fig. 6.13 a Representative microscopy images **b** and quantified diameter of extruded filaments (5 wt% MeHA) using light-permeable needle with varied sizes. Reproduced, with permission from [6]

filament size is mainly determined by the needle size. Here, we demonstrated that filaments with varied diameters from 60 to 600 μm could be printed by using different needles (Fig. 6.13). This is possible because the in situ approach allows for non-viscous ink printing, while it is usually challenging to extrude viscous formulation through a small needle (e.g., diameter <100 μm). This meant that the proposed approach might allow for better printing resolution than conventional approaches.

6.2.2 3D Structure Fabrication

We seek to explore two types of the additive manufacturing process based on the in situ crosslinking strategy. The bioink deposition will be performed either on a flat platform or on a rotating surface.
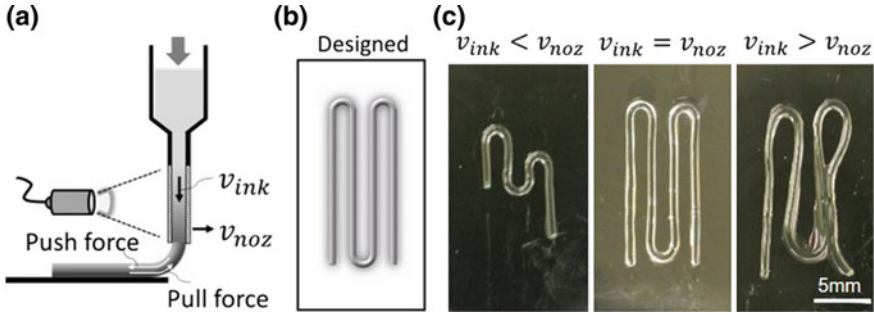
Fig. 6.14 **a** Schematic of typical printing on a flat platform, the push and pull forces between the deposited and to-be-deposited inks are indicated. **b** Schematic of a designed parallel line model and **c** representative images of printed structure with different configurations of v_{ink} and v_{noz}. Reproduced, with permission from [6]

In the conventional 3D printing, inks are deposited on a flat platform layer by layer. The 2D pattern in each layer and switches between layers are generated with the nozzle-platform relative movement in $X-Y$ plane and Z coordinate, respectively. Considering that the bioinks are shaped before coming out of the needle, the bioink speed in the needle (v_{ink}) should match the nozzle speed (v_{noz}) to replicate the designed pattern (Fig. 6.14a) following the equation:

$$v_{\text{ink}} = v_{\text{noz}} \qquad\qquad\qquad (6.1)$$

We tested the printing based on a design with four parallel lines (Fig. 6.14b). When ink extrusion speed is lower than nozzle moving speed ($v_{\text{ink}} < v_{\text{noz}}$), the outcome structure was contractive and significantly shorter than the design, which indicated a pull force from the nozzle. When $v_{\text{ink}} > v_{\text{noz}}$, the printed structure was squeezed and still lose the structure fidelity, which might be caused by the push force from the nozzle. A perfect replicate can be achieved when using a speed match as Eq. (6.1) (Fig. 6.14c).

Based on the previous principle, we tried the 3D printing of different structures, including the typical porous lattice, tubular, and nose-like constructs (Fig. 6.15). The lattice structure (2-mm gap between lines) presented standard lattice pattern made of uniform filaments, and the anisotropic layers are distinguishable without collapse (Fig. 6.15a). The tubular structure (diameter 10 mm, height 10 mm) indicated the ability to fabricate self-standing thin walls without significant deformation (Fig. 6.15b). Moreover, the successful printing of a nose-like model (length 15 mm, width 15 mm) illustrated the capability of fabricating complex tissue-like structure (Fig. 6.15c).

Considering the pre-shaped filament in the needle, the in situ crosslinking approach can be incorporated in another printing way: depositing filaments on a rotating surface for tubular structure fabrication (Fig. 6.16a). Similar to conventional
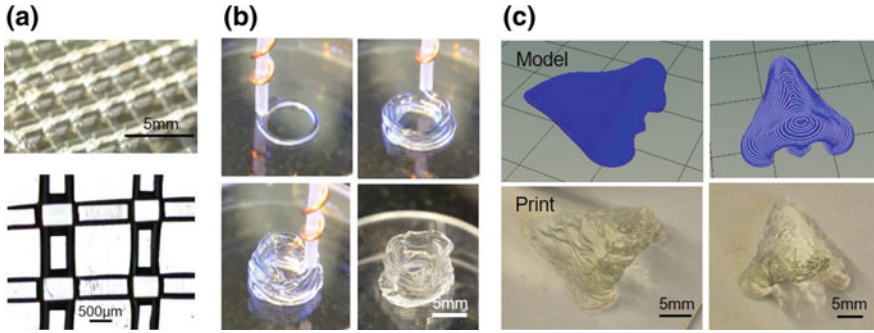
Fig. 6.15 Representative examples of 3D-printed **a** lattice, **b** tubular, and **c** nose-like constructs using 5 wt% MeHA. Reproduced, with permission from [6]
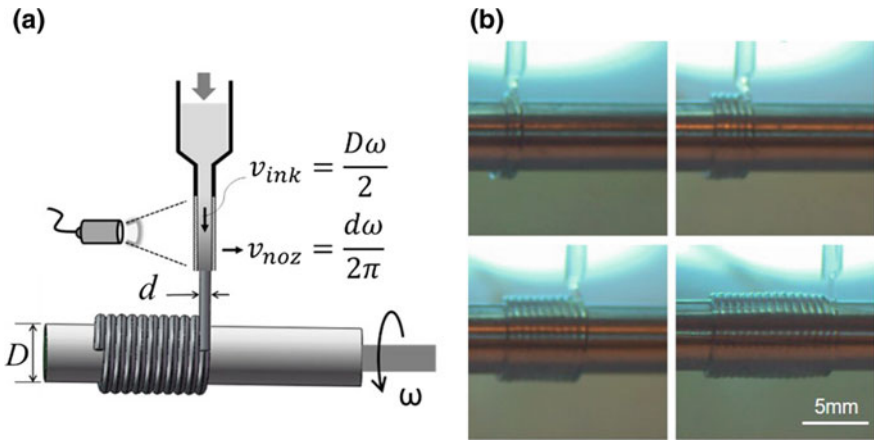
Fig. 6.16 **a** Schematic of printing on a rotating surface and **b** representative images of the printing process. Reproduced, with permission from [6]

printing, there is a requirement for speed match between v_{ink} and v_{noz} following the equations below, respectively:

$$v_{\text{ink}} = \frac{D\omega}{2} \qquad (6.2)$$

$$v_{\text{noz}} = \frac{d\omega}{2\pi} \qquad (6.3)$$

where D and ω are the diameter and angular velocity of the rotating collector, respectively, while d is the filament diameter. Basically, Eqs. (6.2) and (6.3) are to ensure tight deposition in circumference and axial directions, respectively (Fig. 6.16b). It should be noted that the diameter of the tubular structure is mainly determined by the
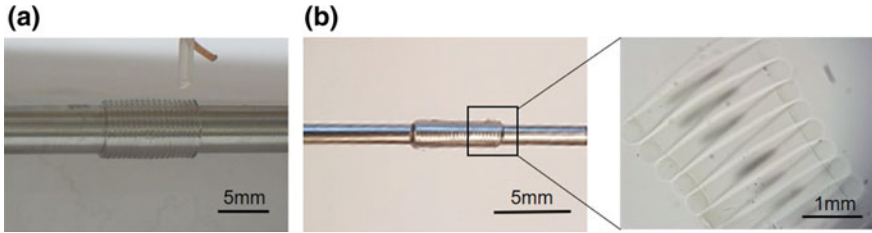
Fig. 6.17 Representative images of printed tubular structures with different diameters (**a**: 5 mm, **b**: 2 mm). Reproduced, with permission from [6]

rotator dimension rather than the printing parameters. We illustrated this by depositing gel filaments on rotators with diameters of 5 or 2 mm (Fig. 6.17). Both tubular structures were quite standard and the hollow feature can be confirmed under the microscope (Fig. 6.17b).

These two printing types enjoy different features. As a typically used method, printing on a flat surface allows for free-form fabrication is more suitable for complex structure fabrication. While printing on a rotating surface benefits the fabrication of a hollow tubular structure with perfect integrity and fidelity. It should be noted that the printing on a rotator is possible because the gel filaments are pre-formed in the needle. In the cases of pre-crosslinking or post-crosslinking strategies, the tubular structures might compromise in the fidelity because of irregular geometry and loss of bioinks.

6.2.3   Structure Stabilization

Co-adhesion between layers is one of the most important things regarding structure stability. Fully fusion between layers is not ideal for layer-by-layer fabrication (e.g., under-gelation status as discussed in Chaps. 4 and 5), while no-fusion might result in layer separation. In the in situ crosslinking strategy, the bioinks are designed to be partially crosslinked in the needle, leaving some uncrosslinked groups for interacting with adjacent layers.

To achieve this, the rheological response of bioink to UV light was used to guide the parameter optimization. Basically, the in situ crosslinking should be controlled to be over technical gelation point, where G' surpasses G'', and to be prior to gelation plateau in order to allow for filament generation and further stabilization, respectively. Taking MeHA as an example again, the G' and G'' of 0.5 wt% MeHA rarely changed after UV treatment, indicating the lack of polymers for gelation network formation (Fig. 6.18). Therefore, MeHA bioink with a concentration lower than 0.5 wt% was not considered for printing. Under concentrations ranging from 1 to 5 wt%, MeHA underwent similar shear modulus profile: Crosslinking started immediately
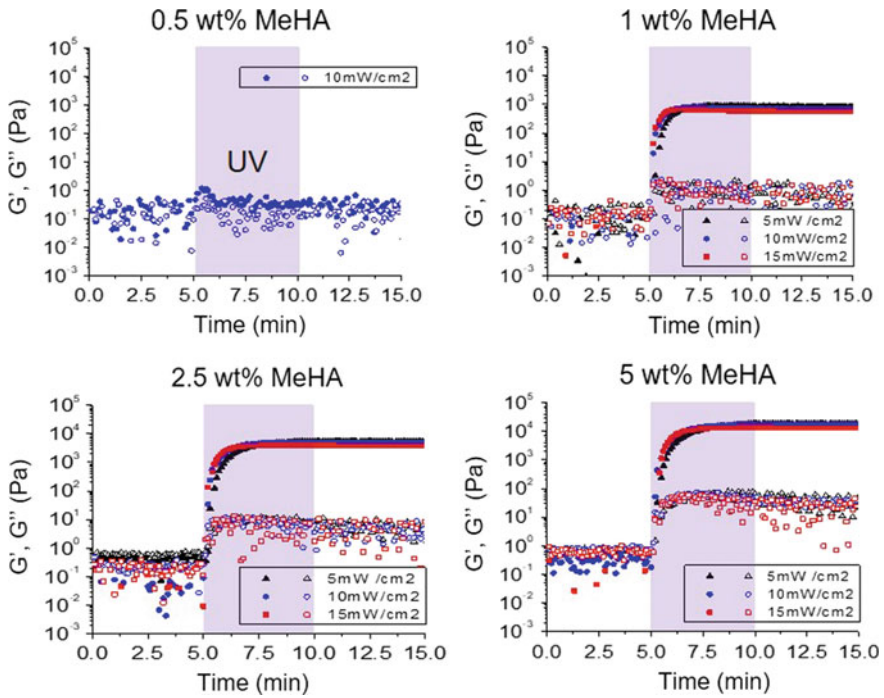
Fig. 6.18 Oscillatory time sweep of MeHA with different concentrations in the presence of UV irradiation (shaded). Reproduced, with permission from [6]

Fig. 6.19 Stabilization time of MeHA inks in the presence of UV irradiation under different light intensities and concentrations. Reproduced, with permission from [6]
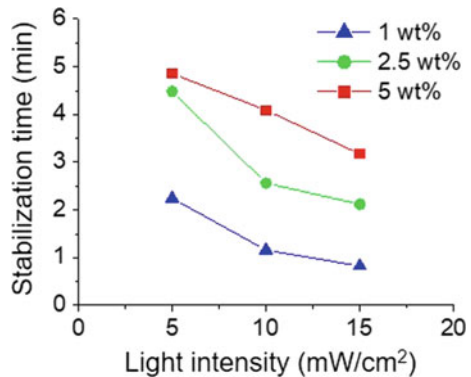
with UV irradiation and ended within 5 min. However, the time reaching stabilization varied with UV intensity, though it did not likely affect the final strength of the crosslinked bioink (Fig. 6.19). It was found that the crosslinking finished earlier with higher UV intensity; the stabilization time of 1 wt% MeHA under 15 mW/cm^2 was ~0.75 min, while that under 5 mW/cm^2 was ~2.25 min. Moreover, higher polymer
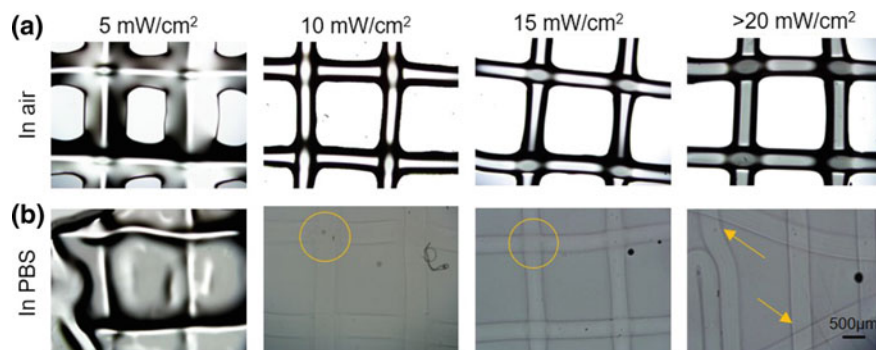
Fig. 6.20 Representative images of printed lattice structure under different light intensity. Reproduced, with permission from [6]
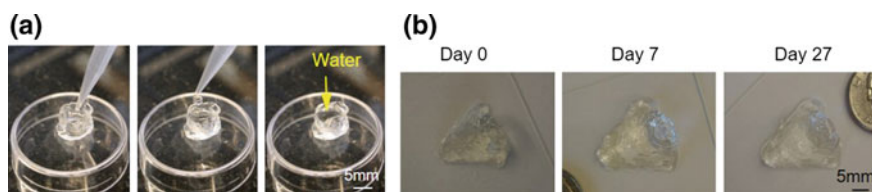
Fig. 6.21 **a** Representative images of a tubular structure, showing the capability of water maintenance. **b** Representative images of a nose-like structure at different time points, showing the structure stability. Reproduced, with permission from [6]

density seemed to induce longer stabilization process; under 10 mW/cm^2 treatment, it took ~1, ~2.5, and ~4 min to reach plateau for 1.0, 2.5, and 5.0 wt% MeHA, respectively.

We illustrated the optimization of parameters by printing 1 wt% MeHA into a two-layer lattice structure under different UV intensities. After printing, the structure under 5 mW/cm^2 UV turned to collapse with obvious liquid-like ink surrounding the thin filaments, while those under higher intensity (>10 mW/cm^2) presented more clear patterns with thicker filaments (Fig. 6.20a). Using the well-established post-stabilization method in Chap. 4, the printed constructs are immersed in initiator solution (0.05 wt% I2959) for post-irradiation for 2.5 min. After doing this, deformation and material fusion were observed with the structure under 5 mW/cm^2 UV, which indicated the inadequate crosslinking during printing. For the structure under >20 mW/cm^2 UV, filaments were found to departure from each other, which indicated poor co-adhesion between layers. Only 10 and 15 mW/cm^2 conditions could allow for structure maintenance with tight conjunctions (Fig. 6.20b). These results demonstrated that there was a window for optimal printing, where proper amount of unreacted groups are reserved for post-stabilization.

By using the optimized parameters and post-stabilization protocol, we tested the stability of other structures. The tubular structure was found to be watertight, which

demonstrates the excellent co-adhesion between layers (Fig. 6.21a). The nose-like structure maintained the integrity very well during one-month incubation at 37 °C (Fig. 6.21b). These results lay the basis for engineering tissue-like constructs.

6.3   Cytocompatibility

One of the advantages for the in situ crosslinking strategy is cell protection. This is due to the use of non-viscous bioinks, which would reduce the shear stress on cells during extrusion. Meanwhile, the in situ crosslinking process applies limited exposure to UV light compared with post-crosslinking strategy, where printed structures are usually exposed to the light during the whole printing process. We illustrated this by measuring the embedded cell viability of a series of samples printed at different time points (18 samples during 40 min with equal interval). It was found that all the tested samples preserved high cell viability (>90%), without significant difference (Fig. 6.22a, b). The normalized cell density was found to slightly decrease in the last few samples, but no significant difference was observed (Fig. 6.22c). This meant that uniform cell distribution in the bioink could be maintained within 40 min, with no concern for cell settling.

Moreover, the cell viability was confirmed to be consistently high (>90%) in filaments with diameters ranging from 200 to 700 μm (Fig. 6.23). A large proportion of living cells (~90%) were maintained in 3D constructs, including two-layer lattice and nose-like structure (Fig. 6.24). These results demonstrate the comprehensively good cytocompatibility of in situ crosslinking approach toward fabricating versatile cell-laden constructs.
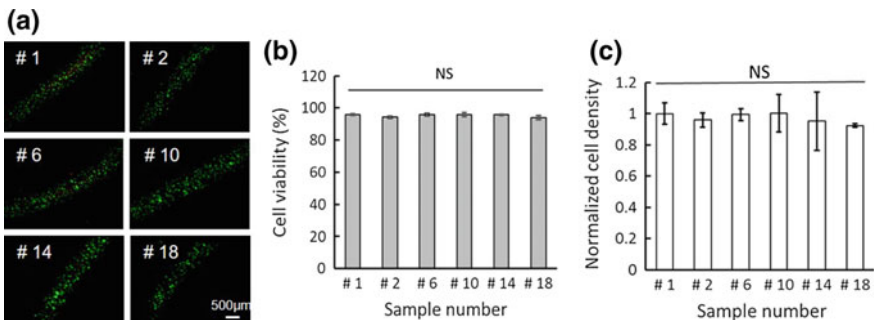
Fig. 6.22   a Representative LIVE/DEAD^{TM} staining images, **b** embedded cell viability, and **c** relatively embedded cell density of number-labelled samples in a sequence of printing. Reproduced, with permission from [6]
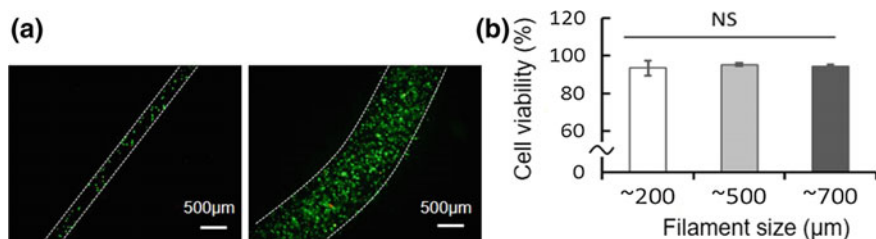
Fig. 6.23 **a** Representative images of LIVE/DEAD^{TM} staining and **b** quantified cell viability for filaments with different diameters. Reproduced, with permission from [6]
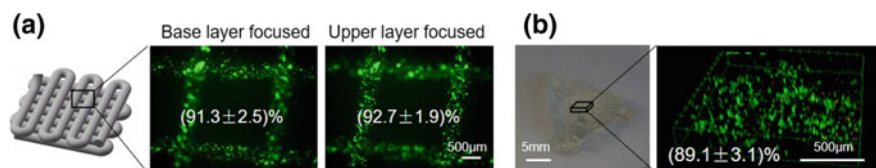

Fig. 6.24 LIVE/DEAD^{TM} staining images of 3D cell-laden **a** lattice and **b** nose-like structures. Reproduced, with permission from [6]

6.4   Generalization to Other Bioinks

As a class of biomaterials, photo-crosslinkable hydrogels usually undergo similar photo-responsivity. Given this, we seek to generalize the proposed approach to more photo-crosslinkable formulations.

6.4.1   Bioink Preparation

To illustrate the bioink generalization, we chose four representative bioinks, covering natural (HA, gelatin) and synthetic [polyethylene glycol (PEG)] sources (Fig. 6.25). As a commonly used photo-crosslinkable hydrogel, gelatin methacryloyl (GelMA) enjoys the good cytocompatibility as gelatin and could undergo covalent crosslinking in the presence of light and photo-initiator. Preserving a thermo-sensitively, GelMA has been used in 3D bioprinting in a temperature-controlled manner with relatively high concentration (e.g., >7 wt%) [7]. It fails to be printed in low-concentration formulation (e.g., 5 wt%). PEG diacrylate (PEGDA) is a typical synthetic formulation that also presents low viscosity at commonly used concentration and molecular weight (<20 wt%, <40 kDa). The crosslinking of MeHA, GelMA, and PEGDA relies on a free radical triggered chain-growth polymerization with methacrylate or acrylate groups. Apart from these inks, we seek to add a step-growth polymerization formulation based on norbornene-functionalized HA (NorHA) [8]. NorHA could undergo thiol-ene click reaction in the presence of dithiol linkers, photo-initiator, and light.
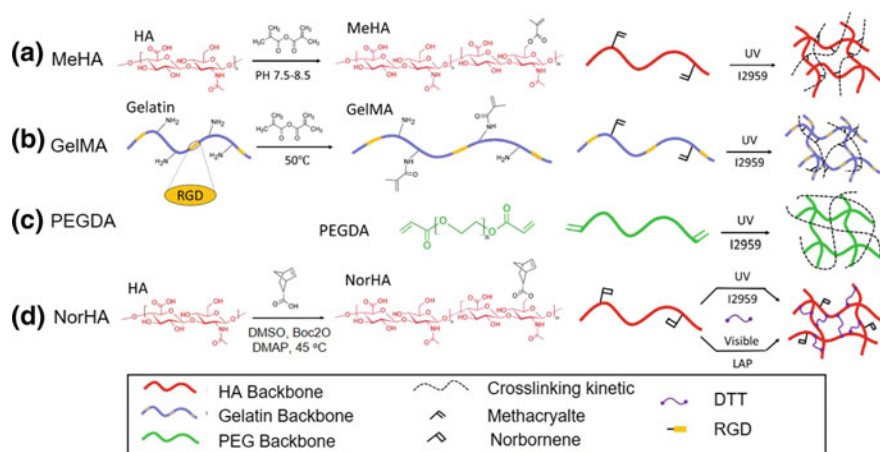
Fig. 6.25 Schematic of different ink modification and their photo-crosslinking kinetics. Reproduced, with permission from [6]

Such reaction is believed to be more controllable, where the ratio of thiol to ene can be tuned. Taking these together, the chosen bioinks should be good representatives regarding the materials sources and crosslinking types.

All the used bioink formulations are synthesized in the laboratory except PEGDA (Sigma). As the preparation of MeHA has been described in Chap. 4, here we clarify the synthesis of GelMA and NorHA as follows.

GelMA: GelMA was synthesized by conjugating methacrylate groups to gelatin backbones as described previously [9]. Briefly, gelatin was dissolved in PBS at 50 °C while stirring at a final concentration of 10 wt%. Methacrylic anhydride (MA) was added into the solution dropwise. After three-hour reaction at 50 °C, the mixture solution was centrifuged at 3500 g for 3 min and GelMA-containing supernatants were collected and diluted with four volumes of water. The GelMA solution was subsequently dialyzed (12–14 kDa tubing) against water at 40 °C for one week (water was changed twice a day), followed by pH adjustment to 7.4 using 1 M NaHCO$_3$ and filter sterilization using 0.2-μm disposable vacuum filtration. After freeze-drying, GelMA was stored at −20 °C before use. Modification of GelMA was confirmed with ^{1}H-NMR as ~50% (Fig. 6.26).

NorHA: Before NorHA synthesis, HA was first converted to its tetrabutylammonium salt (HA-TBA) to make it soluble in dimethyl sulfoxide (DMSO). HA-TBA was synthesized through adding Dowex 50 W proton exchange resin to an aqueous 2 wt% HA solution (3 g of resin per 1 g of HA) for a two-hour exchange reaction. The resin was removed by filtration and the filtrate was neutralized to pH ~ 7.02–7.05 with TBA-OH (6 mL of TBA-OH per 1 g of HA). After freezing at −80 °C and lyophilization for 4 days, HA-TBA was dissolved in DMSO together with 5-norbornene-2-carboxylic acid (Nor-COOH; a mixture of endo and exo isomers) and 4-dimethylaminopyridine (DMAP). Approximately 20 mL DMSO per
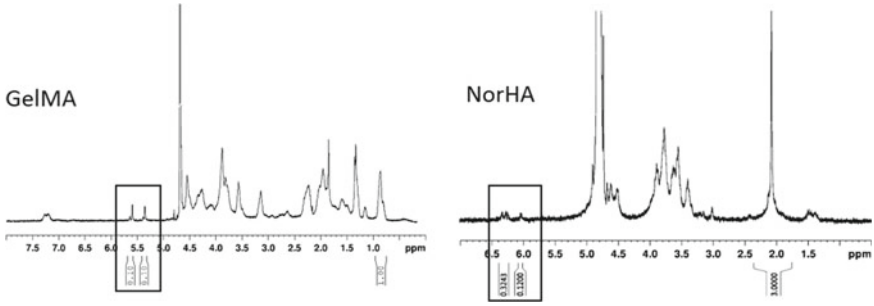
Fig. 6.26 ¹H-NMR spectrum of synthesized GelMA and NorHA materials. Reproduced, with permission from [6]

0.1 g HA-TBA was used, and reagents were dissolved at a ratio of 3 eq Nor-COOH and 1.5 eq DMAP per 1 eq HA-TBA disaccharide repeat unit. Di-tert-butyl dicarbonate (BOC2O) was then added (0.4 eq) and the reaction solution heated to 45 °C. The reaction was allowed to proceed for 24 h, followed by quenching with water, dialysis against water, precipitation against acetone (with 1 g NaCl added per 100 mL NorHA solution), further dialysis, and lyophilization to yield a purified product. Modification of NorHA was confirmed with ¹H-NMR spectra as ~22% (Fig. 6.26).

6.4.2   Rheological Characterization

All the tested bioink formulations contained 0.05 wt% photo-initiator, while the NorHA group included additional DL-dithiothreitol (DTT) as crosslinker. The ratio of thiol to norbornene (X_{DTT}) was designed to be 60% to achieve a fair crosslinking network as suggested in the literature [8]. Here, we compared the rheological response to UV light (10 mW/cm²) for four formulations, 2.5 wt% MeHA, 5 wt% GelMA, 5 wt% PEGDA, and 2 wt% NorHA (Fig. 6.27). Before UV treatment, all the formulations turn to be a solution ($G' < G''$, both smaller than 1 Pa) with low initial viscosity (<15 mPa s) (Table 6.1). The polymerization was initiated immediately with the light on and terminates within 5 min. All the tested bioinks ended up with a storage modulus around 5×10^3 Pa. The rheological similarity of these bioinks lays the basis for easy generalization.

More information about individual formulation used in the study is found in Table 6.1. For NorHA materials, we investigated the use of a visible light initiating system, lithium phenyl-2,4,6-trimethylbenzoylphosphinate (LAP) plus visible light (400–500 nm), in addition to the usually used I2959 plus UV light system. This will illustrate the versatility of the proposed approach in choosing different light systems. Moreover, MMP-degradable peptide was provided as an alternative crosslinker for engineering degradable crosslinking network.
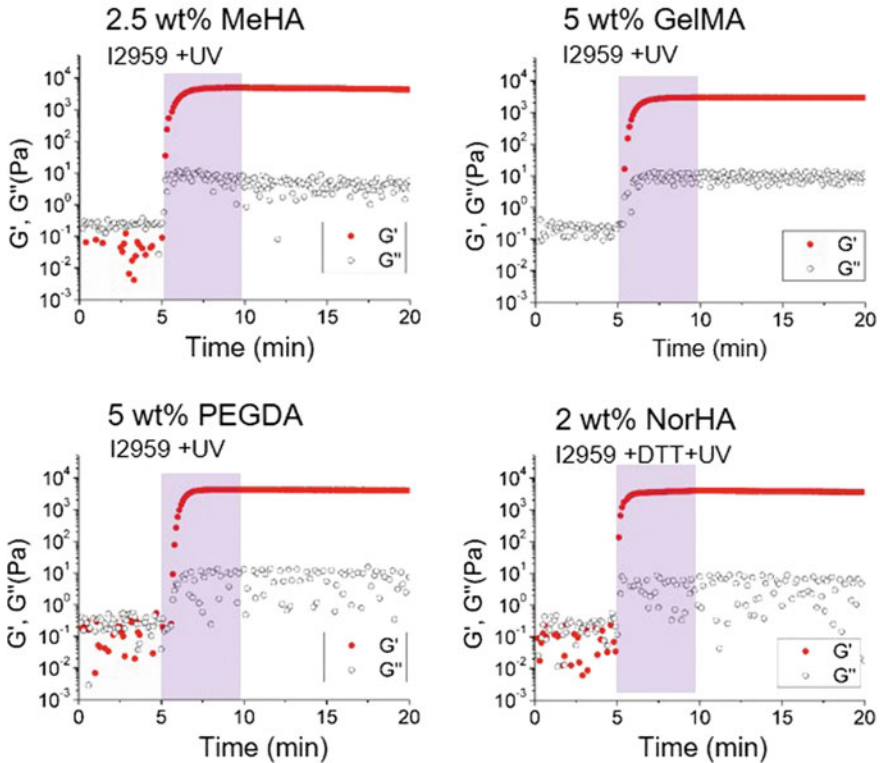
Fig. 6.27 Oscillatory time sweep of different formulations in the presence of UV irradiation (shaded). Reproduced, with permission from [6]

6.4.3 Printability and Cytocompatibility

Based on the similar rheological properties, the four representative bioinks were printed under the same printing parameters. All the formulations allow for the generation of regular gel filament with a standard circular cross section (Fig. 6.28). Meanwhile, they are proved to allow for the fabrication of a tubular structure with elasticity (Fig. 6.28).

The cytocompatibility of this general method was confirmed across all bioink formulations immediately and after one week of culture, including with another group of NorHA crosslinking with 0.05 wt% LAP and visible light (15 mW/cm^2) (Fig. 6.29a). For all five formulations—MeHA, GelMA, PEGDA, NorHA, and NorHA (LAP + Visible)—cells maintained high viability (~96%) after printing (day 0) without significant differences across groups (Fig. 6.29b). After one and seven days in culture, cell viabilities remained at greater than 87% across all groups. Cells in GelMA filaments were viable (~95%) in one-week cultures, which are likely attributed to

Table 6.1 Components, light intensity, and initial viscosity of different formulations. Reproduced, with permission from [6]

Formulation	Raw	Initiator	Crosslinker	RGD	Light source, intensity (mW/cm^2)	Initial viscosity (mPa s)
MeHA-5%	5 wt% MeHA	0.05 wt% I2959	–	–	UV, 0–20	73.4 ± 1.1
MeHA-2.5%	2.5 wt% MeHA	0.05 wt% I2959	–	–	UV, 10	15.1 ± 0.3
GelMA	5 wt% GelMA	0.05 wt% I2959	–	–	UV, 10	5.1 ± 0.7
PEGDA	5 wt% PEGDA	0.05 wt% I2959	–	–	UV, 10	2.5 ± 0.6
NorHA (DTT + I2959)	2 wt% NorHA	0.05 wt% I2959	$X_{DTT} = 0.6$	–	UV, 10	9.9 ± 0.5
NorHA (DTT + LAP)	2 wt% NorHA	0.05 wt% LAP	$X_{DTT} = 0.6$	–	Visible, 15	9.3 ± 0.3
NorHA (DTT + I2959 + RGD)	2 wt% NorHA	0.05 wt% I2959	$X_{DTT} = 0.6$	3 mM	UV, 10	8.9 ± 0.6
NorHA (MMP-deg + I2959 + RGD)	2 wt% NorHA	0.05 wt% I2959	$X_{MMP} = 0.6$	3 mM	UV, 10	8.9 ± 0.7

Note The initial viscosity was obtained under a shear rate of 10 s^{-1}
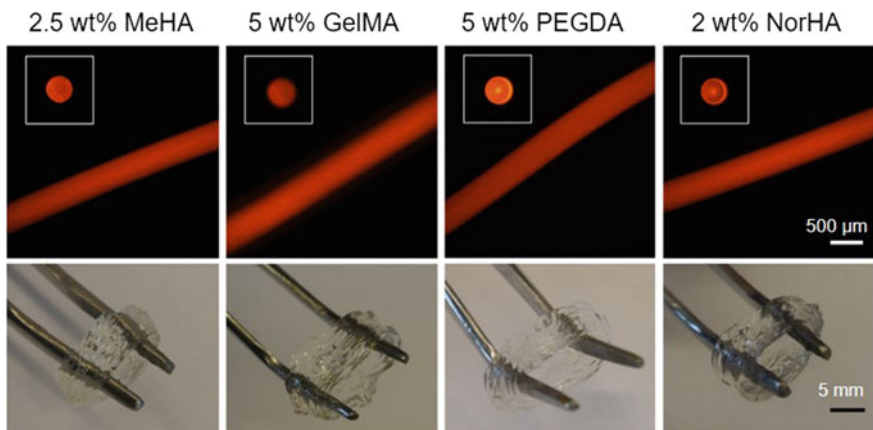
Fig. 6.28 Representative images of printed filaments (upper row, cross section as insert) and tubular structures by using different formulations. Reproduced, with permission from [6]
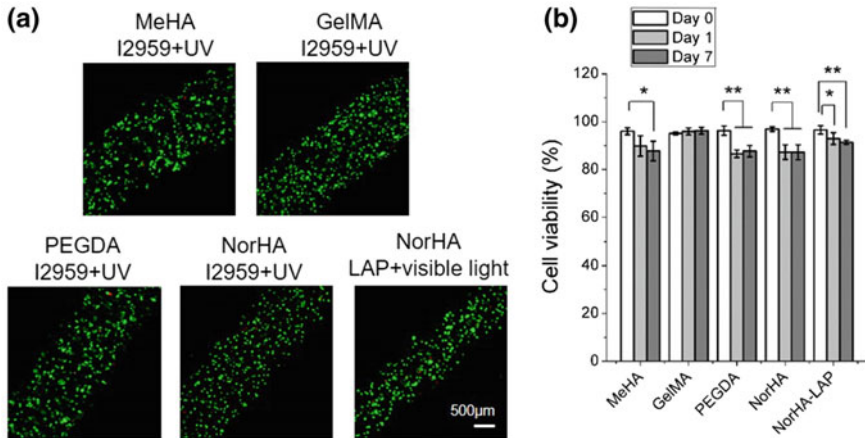
Fig. 6.29 a Representative LIVE/DEAD^{TM} staining images at day 0 and **b** quantified cell viability of cells in filaments using different formulations. Reproduced, with permission from [6]

the RGD sequences within gelatin for cell adhesion, as well as sequences that are degradable in the presence of proteases.

6.5 Complex Filament Generation

Beyond the printing of simple filaments from a range of materials and with viable cells, another advantage of the in situ crosslinking approach is the printing of complex heterogeneous filaments, such as with a coaxial nozzle (Fig. 6.30a). Through the separation of different bioinks in the core and shell needles during printing, it was possible to generate core–shell filaments from multiple inks or cell populations (Figs. 6.30b and 6.31a, b). Though core–shell filament-based constructs have been printed with alginate, collagen, and poly(ε-caprolactone) (PCL) [10, 11], photocrosslinkable hydrogels are seldom applied directly. Furthermore, by controlling
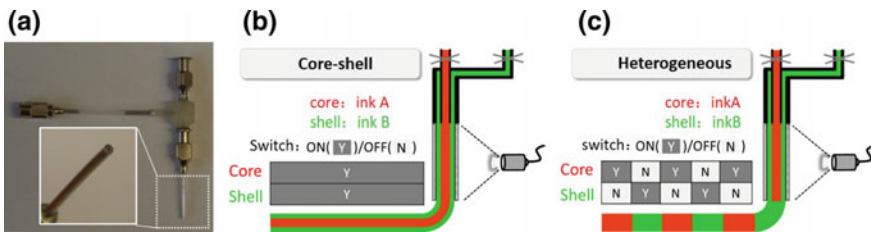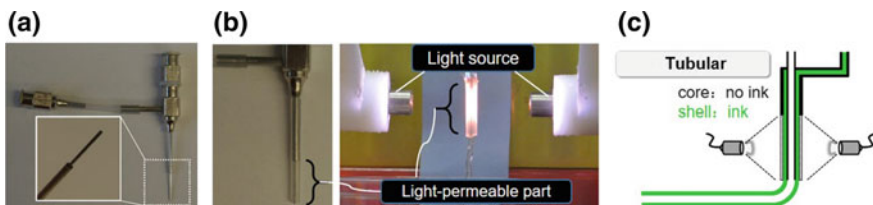

Fig. 6.30 a Images of core–shell needle and schematic of in situ crosslinking for generating **b** core–shell and **c** heterogeneous filaments. Reproduced, with permission from [6]
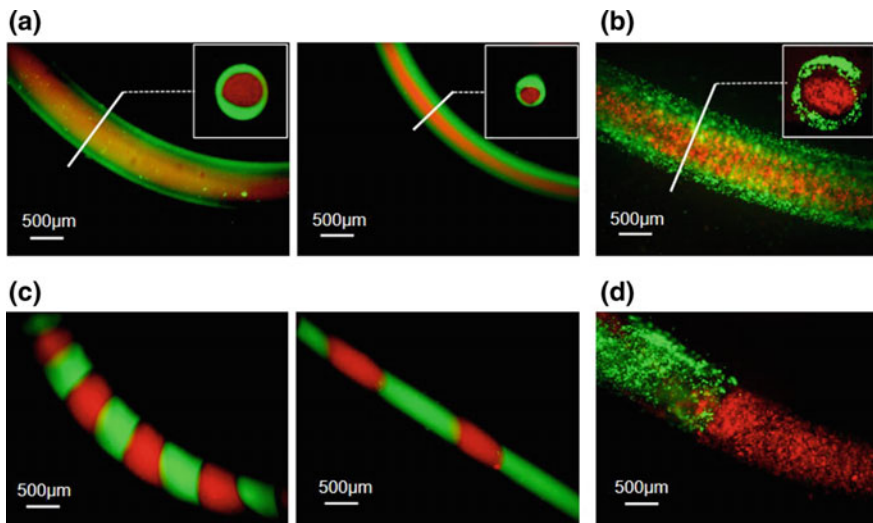
Fig. 6.31 Representative microscopy images of **a**, **c** acellular and **b**, **d** cell-laden filaments with either **a**, **b** core–shell structure or **c**, **d** heterogeneous distribution along filament. Reproduced, with permission from [6]

the on/off status of core and shell channels, heterogeneous filaments were printed with a programmable distribution of multiple inks or cell types along their lengths (Figs. 6.30c and 6.31c, d), which have only been possible previously with microfluidic printheads. Such multi-material filaments are useful in building complex structures, which is now possible with photo-crosslinkable bioinks.

As the last example, open-channel hydrogel tubes were printed using a coaxial nozzle with a longer core needle (Fig. 6.32a), so that irradiation of the shell occurred prior to the introduction of core material (Fig. 6.32b, c). This produced hollow filaments allowed for perfusion (Fig. 6.33a) and cell encapsulation (Fig. 6.33b), with the potential for vascular engineering. Although perfusable conduits of alginate have been reported, our approach again makes this possible with a wide range of materials. Finally, all the three types of complex filaments present distinct distribution of components (Fig. 6.34).

Fig. 6.32 a Images of core–shell needle with loner core part. **b** Assembly of in situ crosslinking setup with light-permeable tubing and bifurcated light source. Reproduced, with permission from [6]
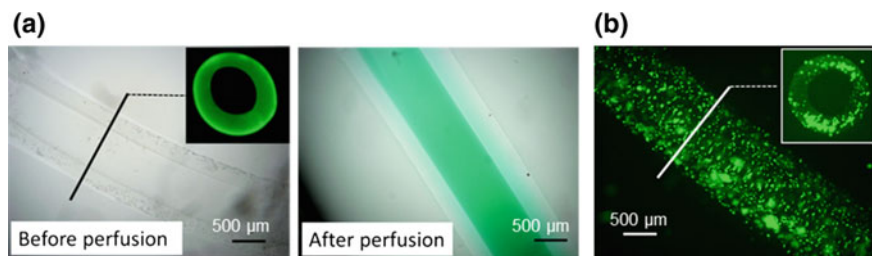
Fig. 6.33 Representative images of **a** acellular and **b** cell-laden tubular filaments with cross-sectional view as insert. Reproduced, with permission from [6]
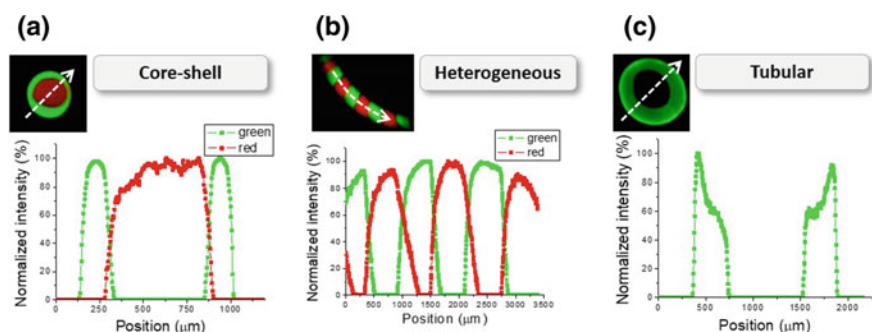
Fig. 6.34 Relative fluorescence intensity profiles with **a** core–shell, **b** heterogeneous and **c** tubular filaments, showing the corresponding distribution of inks. Reproduced, with permission from [6]

References

1. Pereira RF, Bártolo PJ (2015) 3D bioprinting of photocrosslinkable hydrogel constructs. J Appl Polym Sci 132(48):42458
2. Caliari SR, Burdick JA (2016) A practical guide to hydrogels for cell culture. Nat Methods 13(5):405–414
3. Ouyang L, Highley CB, Rodell CB, Sun W, Burdick JA (2016) 3D printing of shear-thinning hyaluronic acid hydrogels with secondary cross-linking. ACS Biomater Sci Eng 2(10):1743–1751
4. Kesti M, Muller M, Becher J, Schnabelrauch M, D'Este M, Eglin D, Zenobi-Wong M (2015) A versatile bioink for three-dimensional printing of cellular scaffolds based on thermally and photo-triggered tandem gelation. Acta Biomater 11:162–172
5. Hockaday LA, Kang KH, Colangelo NW, Cheung PY, Duan B, Malone E, Wu J, Girardi LN, Bonassar LJ, Lipson H, Chu CC, Butcher JT (2012) Rapid 3D printing of anatomically accurate and mechanically heterogeneous aortic valve hydrogel scaffolds. Biofabrication 4(3):035005
6. Ouyang L, Highley CB, Sun W, Burdick JA (2017) A generalizable strategy for the 3D bioprinting of hydrogels from nonviscous photo-crosslinkable inks. Adv Mater 29(8)
7. Yue K, Trujillo-de Santiago G, Alvarez MM, Tamayol A, Annabi N, Khademhosseini A (2015) Synthesis, properties, and biomedical applications of gelatin methacryloyl (GelMA) hydrogels. Biomaterials 73:254–271
8. Gramlich WM, Kim IL, Burdick JA (2013) Synthesis and orthogonal photopatterning of hyaluronic acid hydrogels with thiol-norbornene chemistry. Biomaterials 34(38):9803–9811

9. Loessner D, Meinert C, Kaemmerer E, Martine LC, Yue K, Levett PA, Klein TJ, Melchels FPW, Khademhosseini A, Hutmacher DW (2016) Functionalization, preparation and use of cell-laden gelatin methacryloyl-based hydrogels as modular tissue culture platforms. Nat Protoc 11(4):727–746

10. Kim G, Ahn S, Kim Y, Cho Y, Chun W (2011) Coaxial structured collagen-alginate scaffolds: fabrication, physical properties, and biomedical application for skin tissue regeneration. J Mater Chem 21(17):6165–6172

11. Colosi C, Shin SR, Manoharan V, Massa S, Costantini M, Barbetta A, Dokmeci MR, Dentini M, Khademhosseini A (2016) Microfluidic bioprinting of heterogeneous 3D tissue constructs using low-viscosity bioink. Adv Mater 28(4):677–684

Chapter 7
Biological Characterization and Applications

Chapters 4–6 introduce three bioprinting works using bioinks with different crosslinking mechanisms, mainly from the angles of structural printability and cell viability post-printing. This chapter will present further biological characterization and application based on the specific techniques studied before. Specifically, the printed construct using supramolecular bioinks in Chap. 4 exhibits excellent structure fidelity and mechanical properties and allows for cell adhesion, all of which indicate a promising tissue engineering scaffold. The work in Chap. 5 leads to a perfect balance between structural printability and cell viability by using the easy-accessed and biocompatible bioink, gelatin–alginate hybrid formulation. This technique will be used to further investigate the signal pathway activation and embryonic stem cells' behavior in 3D-bioprinted constructs. The technology developed in Chap. 6 highlights the use of non-viscous bioinks and flexibility in formulation types and building block complexity. Given this, this work will be used to explore the effects of different ink types and other materials cues on cell behavior, such as morphology.

Parts of this chapter have been published in *Biofabrication* [1, 2] and *Advanced Materials* [3].

7.1 Comparison of Different Technologies

Here we summarize the three technologies studied previously in Table 7.1, showing the key features of each one. Based on the theoretical analysis in Chap. 3, a two-step crosslinking process usually happens for microextrusion bioprinting process: Primary crosslinking helps to set the structure after deposition, and secondary crosslinking contributes to the structural stability. The technologies introduced here are mainly distinguished with the name after primary crosslinking mechanism as it is more related to the printability. Basically, we investigated the use of guest–host self-assembly (Chap. 4), thermo-sensitive gelation (Chap. 5), and photo-crosslinking (Chap. 6) formulations in maintaining printing integrity. The former two undergo

Table 7.1 Comparison of bioprinting technologies described in Chaps. 4–6

Features	Chapter 4	Chapter 5	Chapter 6
Primary crosslinking mechanism (printability)	Guest–host self-assembly	Thermo-sensitive gelation	Photo-crosslinking
Secondary crosslinking mechanism (stability)	Photo-crosslinking	Ionic gelation	Photo-crosslinking
Rheology	Viscous, shear-thinning	Viscous, temperature-controlled	Non-viscous
Printer set-up	Basic type	Temperature control	In situ light source
Printability	Good	Good	Good (expandable)
Degradation	Slow	Fast	Flexible
Mechanical properties	Good	Medium	Good
Cell viability	Cell seeding on top (~100%), cell printing (~70%)	Cell printing (>90%)	Cell printing (>90%)

reversible kinetics under shearing or heating stimuli; thus, the secondary crosslinking is expected to stabilize the structure further. The latter preserves covalent crosslinking networks from the primary step and achieves co-adhesion between gels in the secondary step, both with photo-crosslinking. Thus, we understand that primary crosslinking could be either reversible or non-reversible, while the secondary one is usually desired to be relatively stable (e.g., ionic or covalent crosslinking).

Based on different crosslinking mechanisms, Chaps. 4 and 5 bioinks usually present viscous status initially, while the Chap. 6 bioink could be non-viscous. Chap. 4 approach could be performed on a basic extrusion bioprinter, while Chaps. 5 and 6 approaches need temperature control and in situ light source, respectively. As to the printing outcome, all the three methods can deliver well-defined structures and Chap. 6 allows for generalization to other formulations. Based on a secondary photo-crosslinking, the degradation of printed structure with Chap. 4 approach is fairly slow, while that with Chap. 5 degrades faster due to the exchange of Ca^{2+} with other ions in the surrounding buffer. By using thiol-ene chemistry in the crosslinking network, Chap. 6 approach is more flexible with the degradation. As to the cytocompatibility, Chap. 4 allows for good cell attachment after surface modification but would induce some cell damage during the extrusion of viscous formulation, ending up with cell viability of ~70%. With optimized parameters, Chaps. 5 and 6 could both achieve fairly high cell viability (>90%).

In summary, Chap. 4 is suitable for fabricating acellular or cellular scaffolds with good mechanical properties, benefiting from a potential double network. Chap. 5 applies commercial biocompatible hydrogels as bioink, which might act as an easy

platform for 3D cell-encapsulation studies. With the ability of processing conventionally "unprintable" bioinks, Chap. 6 enjoys the flexibility in bioink types and printing ways.

7.2 Cell Activity and Proliferation

7.2.1 Long-Term Cell Activity

In addition to the cell viability post-printing as studied previously, here we seek to further characterize the cell activity during long-term culture (one week or more). Human embryonic kidney cells (293FT) will be used as a cell model for signal pathway activation, while mouse embryonic stem cells (mESCs) will be used for embryoid body formation, paving the way for tissue engineering application. When printing 293FT with gelatin–alginate bioinks, cell spheroids were generated, maintaining high cell viability (Fig. 7.1). Moreover, the spheroids were found to expand significantly with time, with the size of ~30 µm at day 2 and ~90 µm at day 5. This indicates the proliferation of 293FT cells in 3D-printed microenvironment, which can be confirmed by the full-view images (Fig. 7.2). Cell colonies' density was found to increase over time within two weeks, and somehow was low after four weeks. As the 3D hydrogel provides way more space for cell growing than 2D surface, 293FT cells keep proliferating until contact inhibition happens (e.g., at day 30), where cell aggregates became dark and turned to disassemble.

Similarly, mESCs also formed spheroid after printing with gelatin/alginate bioink. The spheroid grew up significantly during one-week culture with normal maintenance medium. Few dead cells were observed (Fig. 7.3). Similar to 293FT again, contact inhibition might happen when cell aggregates occupy most of the space and start to
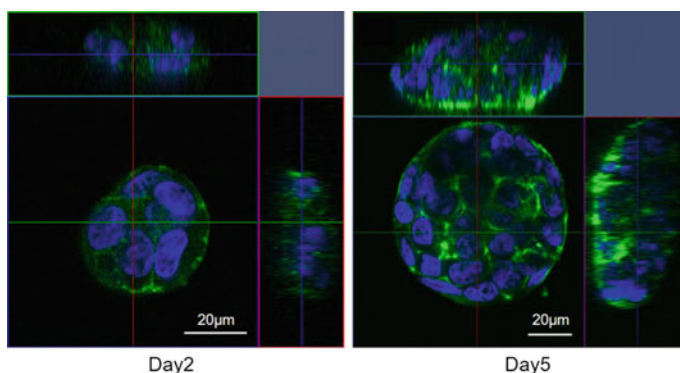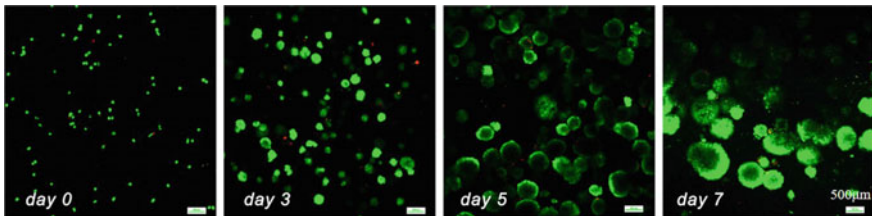

Fig. 7.1 Representative confocal images of 293FT cell spheroids at day 2 and day 5 in 7.5%Gel + 1%Alg bioink. Reproduced, with permission from [1]
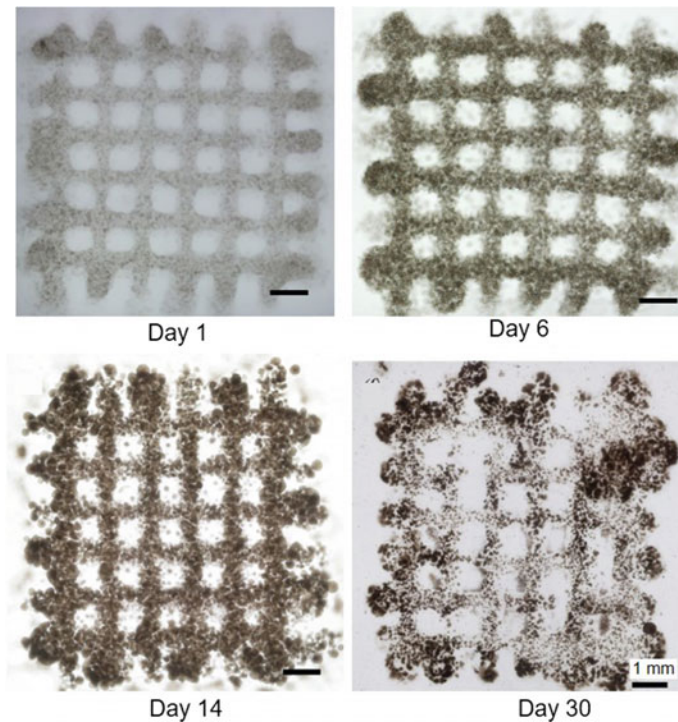
Fig. 7.2 Full-view microscope images of 293FT-laden lattice structure (7.5%Gel + 1%Alg bioink) during one-month culture. Reproduced, with permission from [1]

Fig. 7.3 LIVE/DEAD[TM] staining images of mESCs in printed constructs at different time points. Reproduced, with permission from [2]

fuse with each other. Moreover, cells in the center of big aggregates are believed to have limited access to nutrient and would thus induce cell death. Here we monitored the cell viability beyond one week and observed lots of dead cells at day 10, either in the aggregates or in the debris (Fig. 7.4a). To quantify the live and dead cell counts, we seek to collect and dissociate the embedded cell aggregates. Specifically, the cell-laden constructs were immersed in sodium citrate-EDTA buffer for 3 min, followed by mixing with a pipette to fully break the gel structure. After centrifugation, the
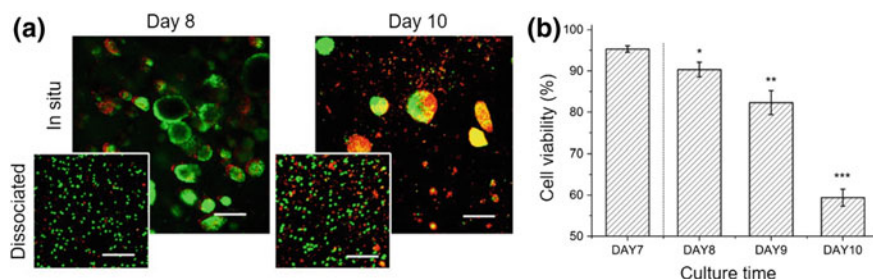
Fig. 7.4 a Representative LIVE/DEAD^{TM} staining images of in situ EBs in the printed structure and dissociated ESCs at day 8 and day 10. **b** Quantified cell viability determined by the staining of dissociated ES cells. Scale bars: 200 μm. Reproduced, with permission from [2]

precipitate, which mainly contained cell aggregates, was treated with cell dissociation buffer (StemPro Accutase) for 5 min to obtain single cell suspension. By counting living and dead cells, 90% cell viability was obtained at day 8 and only ~60% remained at day 10 with a significant difference from that at day 7 (Fig. 7.4b).

These results mean that mESCs growth in 3D-printed structure reaches the peak around day 7 under the initial density of 1×10^6 cells/ml. Long-term maintenance of mESCs in 3D without passaging might be challenging. However, it should be noted that the cell growth profile is also determined by the initial seeding density. Moreover, ESCs differentiation is supposed to be performed before reaching confluence.

7.2.2 Cell Proliferation in 3D

To better characterize the growth of cells in 3D-printed hydrogels, we seek to optimize the protocol of proliferation assay. A commercial assay kit, Cell Counting Kit-8 (CCK-8), was used for the quantification. Basically, the chemical (WST-8) in the kit solution will react with dehydrogenases in cells to give a yellow-colored product (formazan), which is soluble in the tissue culture medium. The cell counts can be estimated by detecting the absorbance of the culture medium based on a reference curve.

A protocol for cell proliferation assessment is provided by the manufacturer, which is, however, developed based on 2D culture or suspension culture. Specifically, working solution (1:10 ratio of CCK-8 stock to culture medium) is added to the 2D cells for incubation for 2 h at 37 °C. The supernatants are collected in 96-well plate (110 μl per well) for absorbance reading at 450 nm. This protocol has been proved to be reliable and repeatable in our study with 2D culture mESCs. However, this might need modification when transferring to a 3D culture system as in this study. When we incubated the 3D-printed cell-laden constructs with the working solution, lots of yellow products were visualized in the gels apart from the surrounding medium (3D in situ) (Fig. 7.5a). By digesting the gels and spinning down the cell debris, we
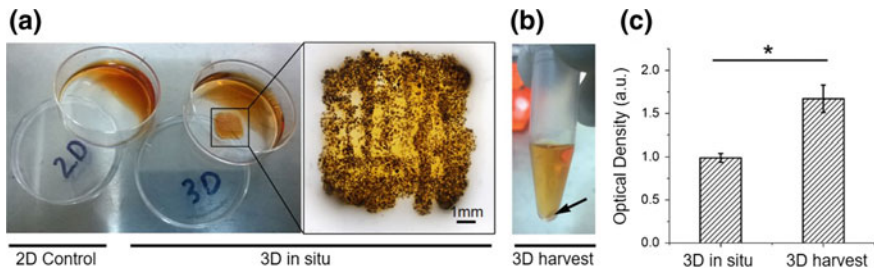
Fig. 7.5 a Optical images of 2D, 3D in situ, and 3D harvest groups after CCK-8 incubation.
b Comparison of optical density between 3D in situ and 3D harvest. Reproduced, with permission
from [2]

obtained darker supernatant (3D harvest) (Fig. 7.5b). This was also confirmed by
detecting the optical density (OD) of the medium prepared by these two protocols
(Fig. 7.5c), where the OD value in 3D harvest group was significantly higher than
(~1.7 times of) that in 3D in situ group. We believe that the in situ approach might
compromise the final results as the generated formazan might be trapped in the gel
and thus result in a reduced reading.

When using the unmodified in situ protocol, cell activities were higher than 2D
control at day 3 and day 5, while dropped down at day 7 (Fig. 7.6). However,
when assessing the proliferation using the harvest protocol, higher activities were
observed throughout the one-week culture. Moreover, the volume change of the
mESC spheroid (embryoid body, EB) also indicates a higher proliferation rate than
2D culture. These results confirmed that the usually used protocol based on 2D cul-
ture might not apply to 3D culture system and a harvesting protocol might help to
correct the results.

Fig. 7.6 Normalized growth
value under different
processing protocols.
Reproduced, with permission
from [2]
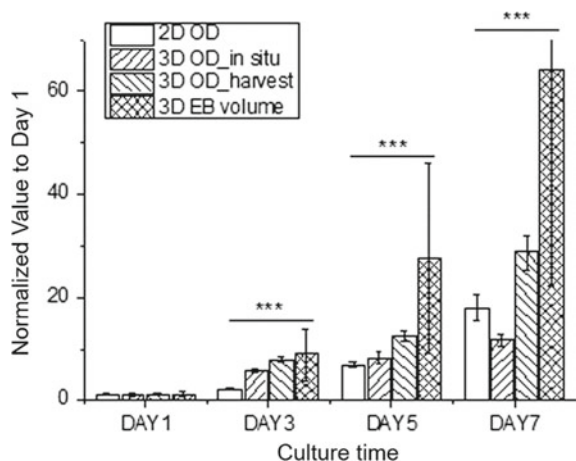
7.3 Signal Pathway Activation

To examine essential cellular functions of bioprinted cells grown in 3D structure, such as protein synthesis and response to cytokine signaling, we employed HEK 293FT cells that had been genetically engineered to express Wnt3a protein or carry a Wnt reporter. Wnt signaling pathway plays an important function during embryo development, tissue homeostasis, and human diseases such as cancer. Wnt3a, a member of the Wnt gene family, is a secreted cytokine that can activate the canonical Wnt/β-catenin pathway. Upon receptor binding, Wnt ligands can trigger a cascade of signaling events and lead to the activation of Wnt target genes. To mimic this process, Wnt reporter plasmid was engineered which contains multiple Wnt-responsive elements driving the expression of a red fluorescent protein gene mCherry. Upon activation of Wnt signaling, the reporter gene will express, indicating that the corresponding cellular pathway is functional. Using this system in our study will allow easy and accurate analysis of the typical cellular function of embryonic cells.

7.3.1 Cell Transfection

Recombinant Wnt3a plasmid CAG-Igk-Wnt3a-Flag-His-IRES-puro was constructed and transfected into HEK 293FT cells to establish Wnt3a-293FT cells. Wnt3a-293FT cells were maintained by selection using 0.5 μg/ml puromycin (Sigma, USA). For Wnt reporter-293FT, a piggyBac plasmid containing 7xTCF/Lef-binding sites driving mCherry gene and PGK promoter driving neomycin-resistant gene was transfected into normal HEK 293FT cells. Cells with no background mCherry expression showed strong red fluorescence in response to CT99021 (a GSK3 inhibitor and Wnt signaling pathway activator) treatment, which were selected by fluorescence-activated cell sorting (FACS) (BD, Aria II, USA). Both Wnt3a-293FT and Wnt reporter-293FT were cultured in the same medium as normal HEK293FT cells.

7.3.2 Protein Expression of Activator Cells

We first assessed the cell viability of Wnt3a-293FT, the activator cells, after printing with gelatin–alginate bioinks. Similar to normal 293FT cells, high cell viability (>90%) was achieved at day 0 and day 3, which probably meant ideal cell maintenance after transfection (Fig. 7.7). We further characterize the expression of Wnt3a protein from Wnt3a-293FT cells by using Western blot. Both the 2D- and 3D-cultured Wnt3a-293FT cells were seen with Wnt3a expression, while the normal 293FT control in 2D (con 2D) was blank (Fig. 7.8a). By normalizing the amount of Wnt3a to housekeeper GAPDH, we found a higher level of Wnt3a protein expression (0.42 ± 0.12) in 3D-printed constructs than that in 2D (0.28 ± 0.03) (Fig. 7.8b).
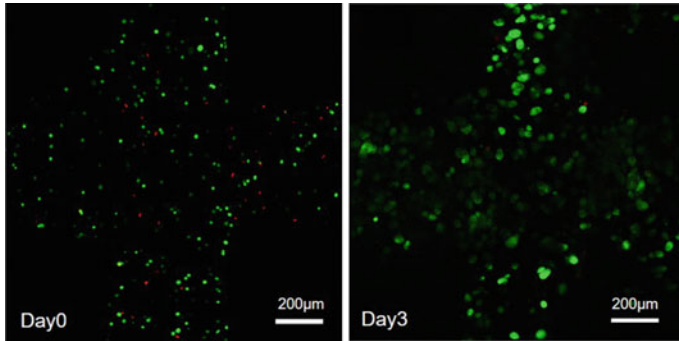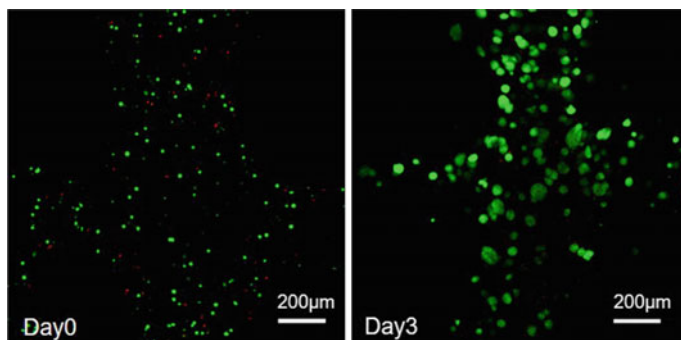
Fig. 7.7 LIVE/DEAD^{TM} staining images of Wnt3a-293FT cells in printed lattice structure (7.5%Gel + 1%Alg bioink). Reproduced, with permission from [1]
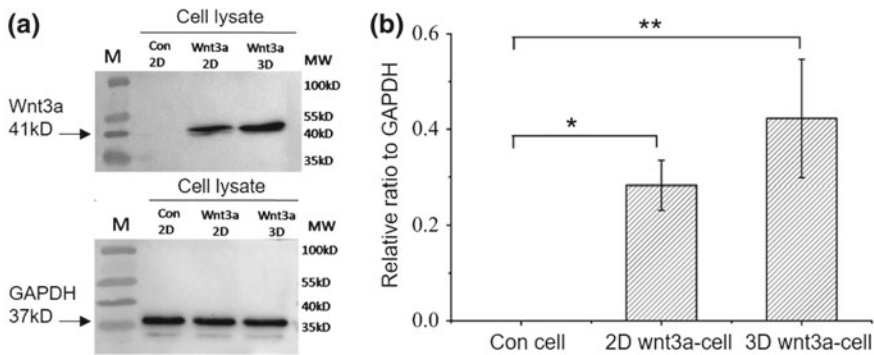

Fig. 7.8 Wnt3a protein expression assessed by Western blot. **a** Wnt3a and GAPDH band and **b** the relative ratio of Wnt3a protein to GAPDH for 2D normal 293FT, 2D Wnt3a-293FT, and 3D Wnt3a-293FT cells. Reproduced, with permission from [1]

7.3.3 Activation of Reporter Cells

The Wnt reporter-293FT cells presented similar cell viability after printing (Fig. 7.9). Without the treatment of activator CT99201, there is no fluorescence detecting, while almost all cells expressed mCherry-labeled protein after adding CT99201 in both 2D control and 3D-printed samples (Fig. 7.10). These results demonstrated the successful activation of reporter cells after 3D printing and would thus indicate the possibility of investigating the signal pathway in the 3D-bioprinted microenvironment. Taken all together, the 3D-bioprinted cells are proved to have a normal biological function, cell signaling activity, and gene transcription response.

Fig. 7.9 LIVE/DEAD^{TM} staining images of reporter-293FT cells in printed lattice structure (7.5%Gel + 1%Alg bioink). Reproduced, with permission from [1]
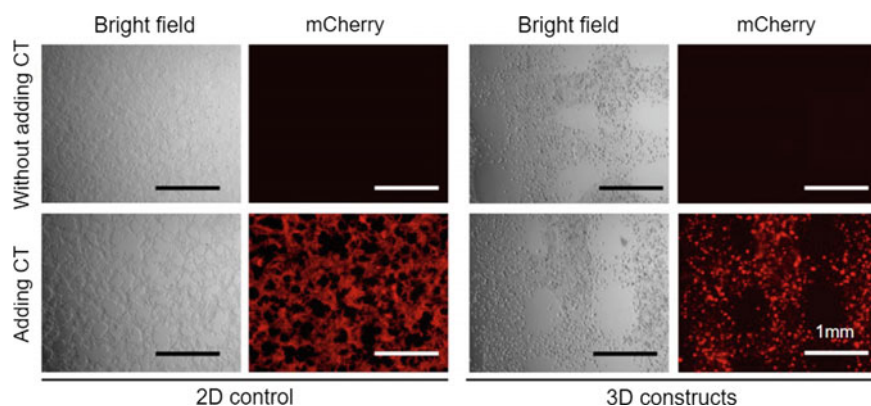
Fig. 7.10 Activating reporter-293FT in 2D and 3D at day 3 with or without adding CT99021 for 48 h. Reproduced, with permission from [1]

7.4 Embryoid Body Formation

With the capability of self-renewal and differentiating into all somatic cell types, embryonic stem cells (ESCs) hold great promise as an in vitro model system for studies in early embryonic development, as well as a robust cell source for applications in diagnostics, therapeutics, and drug screening. By mimicking some of the spatial and temporal aspects of in vivo development, 3D cellular spheroids termed embryoid body (EB) is a basic 3D model for ESCs' culture and differentiation studies. It was reported that the size and uniformity of EBs could vastly influence stem cell fate. As shown in previous results with bioprinting mESCs, we observed the EB formation in the 3D-printed constructs. Here we seek to further clarify the mechanism of EB generation.
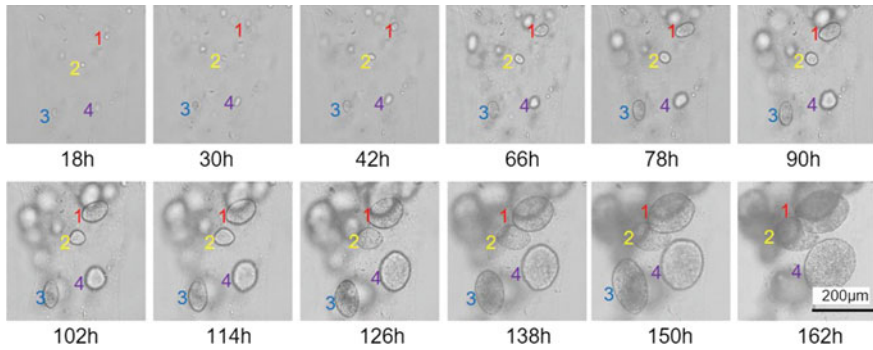
7.4.1 Embryoid Body Growth

Figure 7.11 clearly showed the growth of EBs with time under different initial cell seeding densities ranging from 0.5 to 2.0 $\times$ 10^6/ml. The higher of the initial cell density, the more area of the gel space was occupied by EBs. In all cases, EBs are distributed uniformly in the lattice structure which maintained good integrity for up to 7 days. Some free EBs were found in the pore area when applying a high cell seeding density (1 or 2 $\times$ 10^6/ml), which might be caused by the outgrowth of EBs toward medium when they reach the edges of the gel filament.

To better illustrate the growth kinetics of EBs in the gel, we performed live imaging of the same position in the construct for over one week (Fig. 7.12). By marking the individual single cell initially, we could monitor their morphology change with time. Significant growth of the cell spheroid was observed from the single cell at the initial position, reaching the diameter of ~150 at 162 h. Not much cell migration was indicated, which might mean the 3D immobilization caused by gels. It was noted that one of the tracked EBs (No. 3) was missing at 162 h, which we believe departed from the gel as it kept growing throughout the gel boundary. This confirmed the observation in Fig. 7.11, where some free EBs were found outside the filaments.
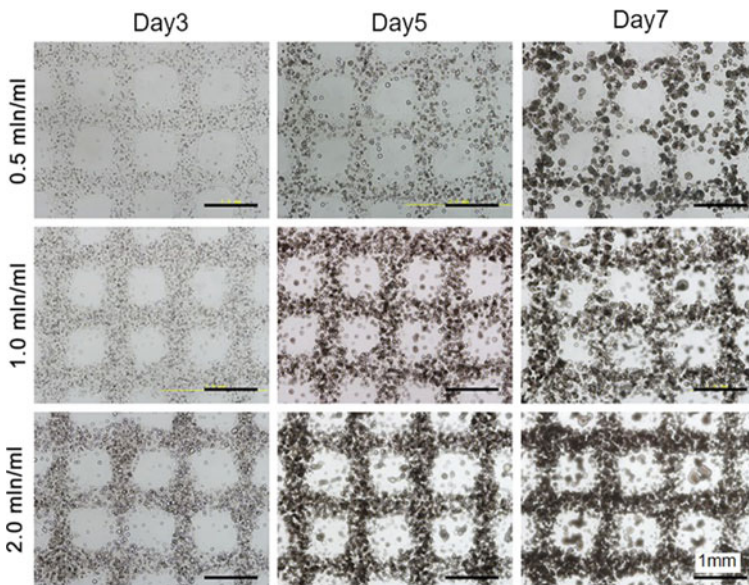
Fig. 7.11 Representative microscope images of lattice structures (7.5%Gel + 1%Alg bioink) initially embedded with varied densities of mESCs at different day 3, day 5, and day 7. mln/ml = 10^6/ml. Reproduced, with permission from [2]

Fig. 7.12 Live images of a local area in the printed lattice structure (7.5%Gel + 1%Alg bioink), showing the growth of individual EB with time. Reproduced, with permission from [2]

7.4.2   Morphology Characterization of Embryoid Body

The size and uniformity of EBs have attracted big attention as they would greatly affect the differentiation fate of ESCs. It has been reported that EBs with ~100 μm diameter are more active in expressing ectoderm markers, while those with ~500 μm diameter express more ectoderm and ectoderm markers [4, 5]. The uniformity of EBs is more related to the controllability of the differentiation, and irregular EBs are found to induce heterogeneous and random differentiation [4, 6, 7]. Therefore, we seek to assess these two features of EBs generated under different conditions.

After digesting the 3D-printed structures, EBs are collected and resuspended in PBS. Microscope images were taken immediately after replacing the suspension in a petri dish. By editing an image analysis code in MATLAB, EB profiles are extracted automatically as a closed geometry based on the phase contrast (~270 EBs are analyzed under each condition). The perimeter (L) and area (A) of the extracted geometry are subsequently obtained. Here we estimate the EB diameter (D) and circularity (C) using the following equations:

$$D = \sqrt{4A/\pi} \tag{7.1}$$

$$C = \frac{4\pi A}{L^2} \tag{7.2}$$

From the histogram of EB diameter fitted with a Gauss distribution curve, we found that EB size increased significantly from ~50 to ~110 μm when the construct was cultured from day 3 to day 7, with more concentrated distribution at earlier time point (e.g., day 3) (Figs. 7.13 and 7.14). Initial cell density (from 0.5 to 2.0 × 10^6/ml) had little influence on the average size of EBs at specific time point. However, increased cell density was likely to result in the reduction of the uniformity of EB size, especially at day 7: The EB diameter of 2.0 × 10^6/ml group at day 7 was vastly
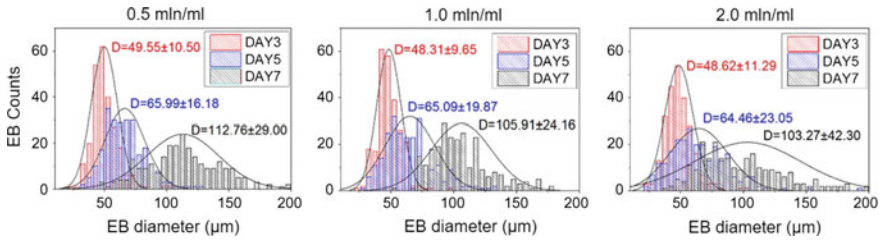
Fig. 7.13 Distribution of EB size with different initial concentration at day 3, day 5, and day 7. mln/ml = 10^6/ml. Reproduced, with permission from [2]

Fig. 7.14 Quantified EB diameter with different initial concentration at day 3, day 5, and day 7. Data are presented as mean ± SD. mln/ml = 10^6/ml. Reproduced, with permission from [2]
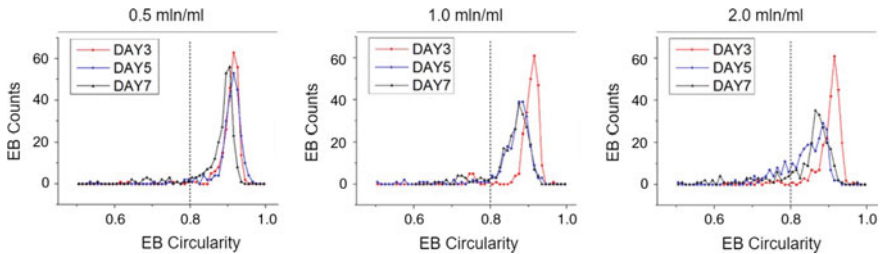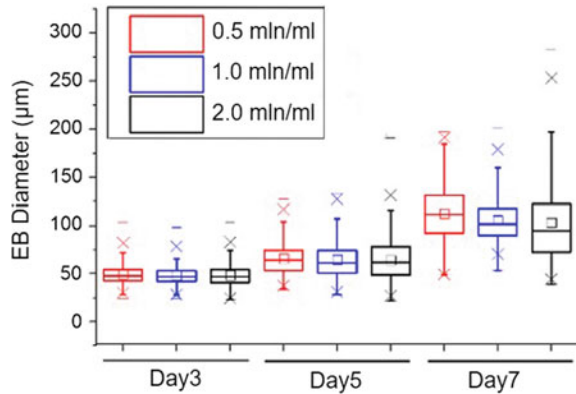

Fig. 7.15 Distribution of EB circularity with different initial concentration at day 3, day 5, and day 7. mln/ml = 10^6/ml. Reproduced, with permission from [2]

heterogeneous, with a deviation of 42.30 μm, which was much more than those of other two groups.

As to the circularity, we define a threshold beyond 0.8 to filter the EBs with fairly round geometry. The histogram of EB circularity clearly indicated that, under 0.5×10^6/ml initial cell density, most of the EBs retained a high circularity (with a median around 0.9) at different time points (Figs. 7.15 and 7.16). Increasing the initial cell density was likely to induce less concentrated EB circularity, especially at day 5 and

Fig. 7.16 Proportion of EBs with circularity >0.8 under different initial concentration at day 3, day 5, and day 7. mln/ml = 10^6/ml. Reproduced, with permission from [2]
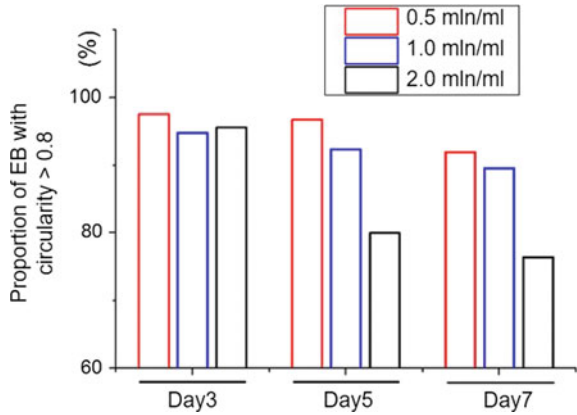
day 7. Specifically, under the cell density of 2.0×10^6/ml, the proportion of EBs with circularity more than 0.8 decreased with time: More than 95% EBs presented a high circularity at day 3, and only 80% retained that at day 5 and even less at day 7. This should be caused by the increased fusion of EBs under a high cell density, and contact inhibition would also add to it.

In summary, longer culture time and higher cell seeding density would slightly compromise the EB uniformity and regularity. The EB size is mainly determined by the culture time, which could reach the dimension of 100–150 µm after one-week culture.

7.4.3 Maintenance of Pluripotency

Pluripotency markers, i.e., Oct-4, SSEA1, and NANOG, were analyzed to determine the pluripotency maintenance of ESCs after 7-day culture in the 3D hydrogel construct. Immunofluorescence staining images showed that almost all of the cells within the EB were successfully stained with both Oct-4 and SSEA1 (Fig. 7.17). The flow cytometry analysis further confirmed the percentages of Oct-4- and SSEA1-positive
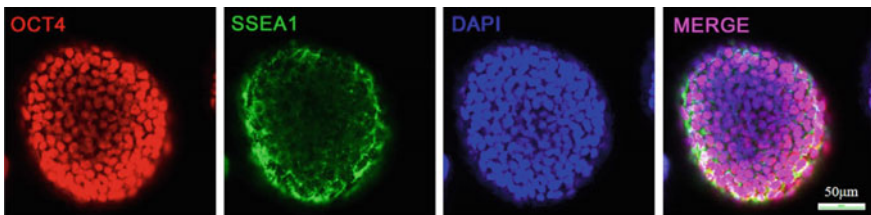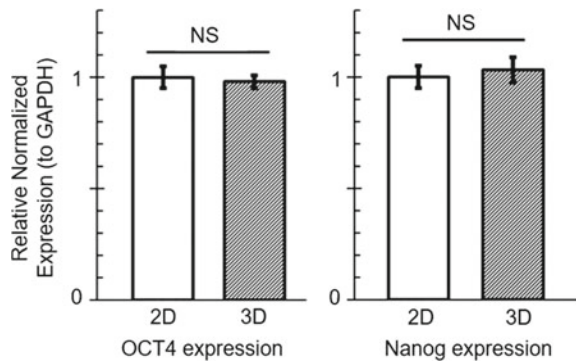

Fig. 7.17 Confocal images of immunofluorescence stained EB at day 7. Reproduced, with permission from [2]
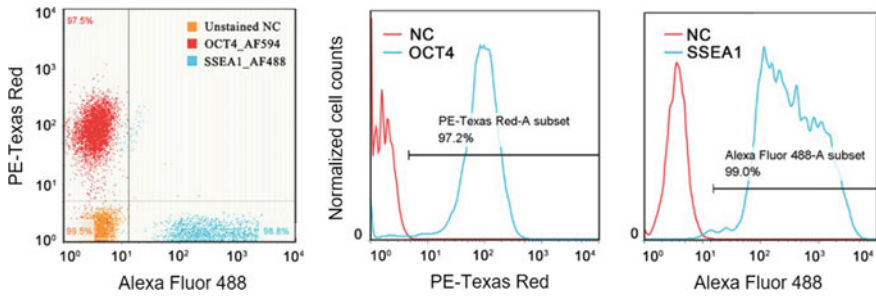
Fig. 7.18 Quantification of Oct-4- and SSEA1-positive cells after EB dissociation (day 7) using flow cytometry. Reproduced, with permission from [2]

Fig. 7.19 Quantification of Oct-4 and NANOG gene expression of EBs (day 7) using q-PCR. Reproduced, with permission from [2]


cells which are 97.2 and 99.0%, respectively, indicating a fairly high pluripotency (Fig. 7.18). When comparing with 2D-cultured cells, no significant difference was observed in the 3D-printed cells with the gene expression of Oct-4 and NANOG (Fig. 7.19). Taking all together, we could conclude that mESCs pluripotency was well maintained after printing and culturing for up to one week, confirmed by a comprehensive set of evidence based on relevant marks.

7.4.4   Comparison with Conventional Methods

Hanging-drop and suspension culture are two conventional approaches being used for EB formation. In the hanging-drop approach, cell suspension drop with certain number of single cells hangs on a surface or well [8]. The embedded cells would quickly aggregate together in the bottom of the drop because of gravity, thus to form a single EB in one drop (Fig. 7.20). The suspension approach relies on a non-attachment culture condition, where ESCs are cultured in suspension status and would aggregate spontaneously [9] (Fig. 7.20). Basically, hanging-drop experiences an extremely low yield efficiency, while suspension suffers poor uniformity. Here we seek to compare
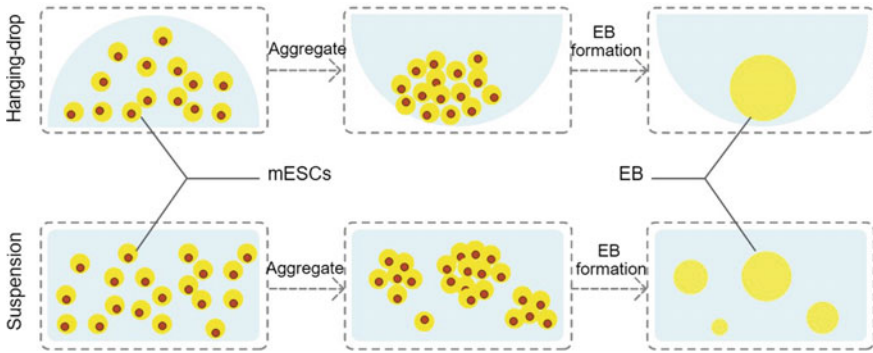
Fig. 7.20 Schematic of hanging-drop and suspension approaches for EB formation
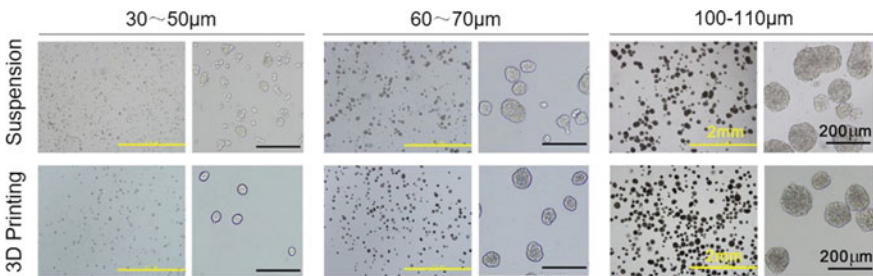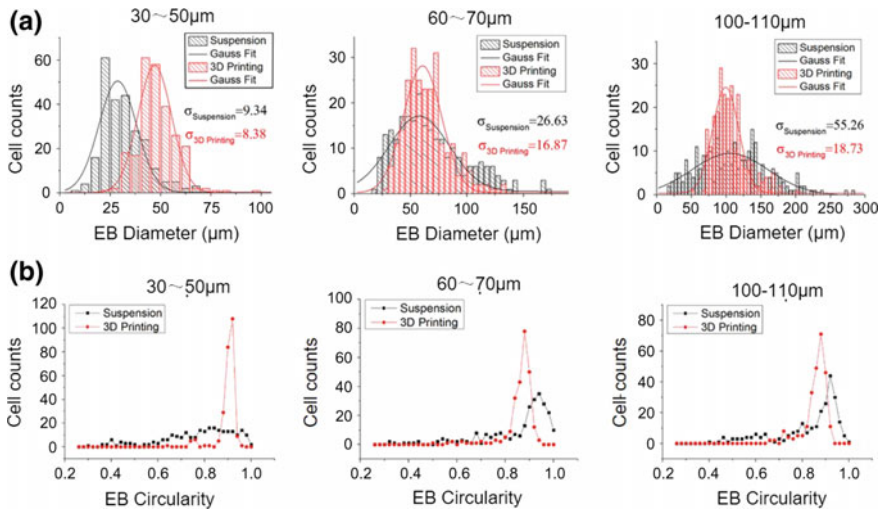

Fig. 7.21 Microscope images of EBs generated from suspension and 3D printing approaches under different ranges of EB dimension. Reproduced, with permission from [2]

the studied 3D printing approach with these conventional ones in terms of EB yield and uniformity.

Following the previous EBs' harvesting protocol, we captured the microscope images of 3D printing EBs at different size ranges, in comparison with suspension EBs (Fig. 7.21). By analyzing the EB morphology, we found that the size distribution of 3D printing EBs was much more concentrated than that of suspension ones in the dimension ranges of $60 \sim 70$ and $100 \sim 110$ μm (Fig. 7.22a). In suspension culture, big aggregates were seen along with tiny ones, even with single cells (Fig. 7.21). The random and uncontrollable aggregating process in suspension culture is believed to cause such varied size distribution. Moreover, the circularity measurement indicated that the suspension EBs presented poor roundness compared with 3D printing: Much more irregular EBs (circularity < 0.8) were found in suspension culture, especially in the dimension range of $30 \sim 50$ μm (Fig. 7.22b). In the early stage of aggregating, cells might not be well organized into a spherical geometry due to a free and spontaneous process in suspension.

In contrast, hanging-drop approach provides a local environment where cells are driven by gravity to form a single uniform spheroid, the size of which is mainly determined by the initial cell counts in the drop (Fig. 7.23): EB diameter increases

Fig. 7.22 Distribution of **a** EB diameter and **b** EB circularity for suspension and 3D printing approaches under different ranges of EB dimension. Reproduced, with permission from [2]

Fig. 7.23 Representative images of EBs generated from hanging-drop approach with gradient initial cell density. Reproduced, with permission from [2]

from ~50 to 250 μm when with the increasing of cell density from 20 to 2000 cells per drop. It should be noted that the aggregate might turn to be out-of-shape when there are too many cells (e.g., 20,000) in one drop. Nevertheless, this approach is recognized with its generally high uniformity and repeatability. However, it might be challenging for hanging-drop to obtain EBs in a high-throughput way due to the one-EB-one-drop principle. Here we assess the EB yields in an area of 1 cm^2 under three approaches (Fig. 7.24). Due to the limitation from drop size (20 μl volume), only nine EBs could be achieved in maximum. When using a medium cell density (0.33×10^6/ml) in suspension culture, around 900 EBs were obtained within the considered area (made of six microscopy images under $4\times$ magnification). In contrast, 3D printing approach could achieve around 3000 uniform EBs (initial cell density 1×10^6/ml) with four layers of lattice filaments. This yield could be easily improved further by adding more layers to the constructs.

Taking these results together, for the generation of EBs smaller than 200 um, 3D bioprinting enjoys significant advantages over suspension culture in terms of EB uniformity in addition to the benefits from high yield compared with hanging-drop
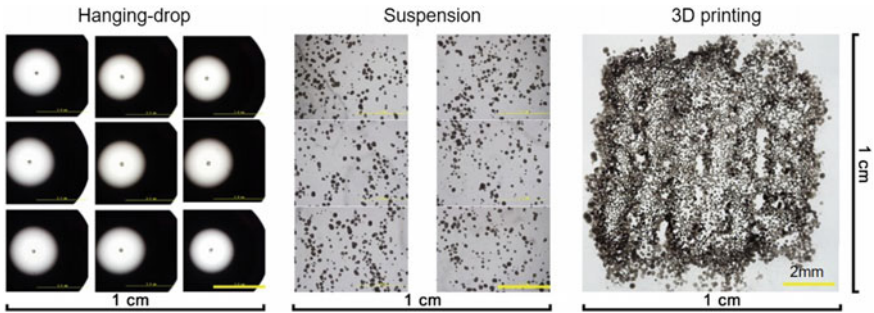
Fig. 7.24 Microscope images of EBs generated from different approaches, showing varied yields in an area of 1×1 cm^2. Reproduced, with permission from [2]

**Table 7.2** Comparison of different EB formation methods. Reproduced, with permission from [2]

	Hanging-drop	Suspension	3D print
Forming mechanism	Aggregation by gravity	Self-aggregation	Proliferation
Size control	Time and cell density	Time and cell density	Mainly time
Diameter range	50 ~ 500 µm	50 ~ 500 µm	30 ~ 200 µm
Uniformity	High	Low	Medium–high
Yield	Low	High	High
Operation	Time-consuming for seeding and medium refresh	Complex for medium refresh	Time-saving and easy for medium refresh

culture (Table 7.2). Moreover, 3D bioprinting allows for easy operation in terms of cell seeding and medium change. Thus, we envision that 3D bioprinting could act as a high-throughput approach for pluripotent EBs production and thus applications in fundamental research on the development and cell-based therapeutics. It should be noted that such EBs could be harvested for subsequent studies in conventional ways or be used in situ based on a well-defined and complex 3D model.

7.5 Cell Behavior Modulation

7.5.1 Material Cues

It has been well known that substrate stiffness and topography play critical roles in cell behavior in 2D culture. The cell–matrix interaction in 3D microenvironment has recently attracted attention due to the development of biocompatible hydrogel materials and biofabrication technologies [10–12]. Basically, cell-binding ligands
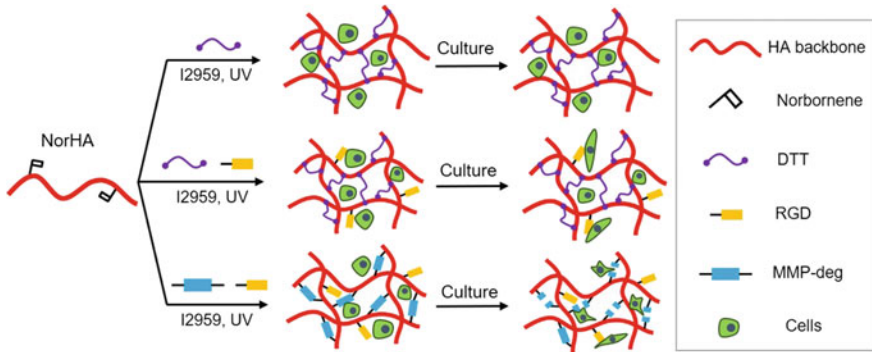
Fig. 7.25 Schematic of three NorHA formulations with different functionalizations. Reproduced, with permission from [3]

(e.g., RGD peptide, collagen, laminin, fibronectin) would affect the cell attachment, migration, and further cell–cell interaction in 3D hydrogel network. The hydrogel crosslinking mechanism and degradation kinetics are also believed to affect cell activity and tissue formation.

Due to the versatility of the in situ crosslinking strategy introduced in Chap. 6, we seek to investigate the effects of typical materials cues on cell behavior, starting from matrix type. Furthermore, different crosslinkers and functionalization will be applied to NorHA-based bioink to achieve different 3D cellular microenvironment (Fig. 7.25). Specifically, non-degradable (DTT) or MMP-degradable (MMP-deg) dithiol crosslinkers and thiolated RGD peptide are added into the formulation to react with norbornene groups via thiol-ene click chemistry in the presence of photo-initiator and curing light. The MMP-degradable crosslinker is a well-established peptide (GCNSGGRM↓SMPVSNCG) which has been proved to be cleaved by MMP-2 [13].

7.5.2 Cell Response

Different cell morphology was observed with different types of bioinks as shown in Fig. 7.26. After 7 days of culture, though high cell viability is maintained in all cases, NIH 3T3 cells turned to be round in most bioinks except GelMA. Specifically, the cell in GelMA presented higher cell density and elongated morphology. The reason for this might be the presence of RGD-binding sites in gelatin backbone, which enhance cell attachment and spreading. All the other formulations do not have such binding ligands and would thus induce round cell geometry.

To further confirm the effect of RGD on fibroblast morphology, we compare different NorHA formulations as shown in Fig. 7.27. Basically, spread cells were observed in the DTT + RGD and MMP-deg + RGD groups, while not in the DTT group. By capturing the sliced images of the printed filament, we could visualize the
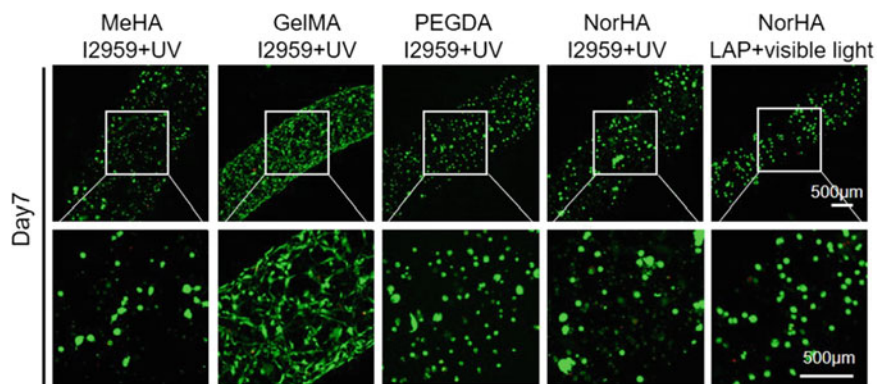
Fig. 7.26 LIVE/DEAD^{TM} staining images of printed 3T3 cells with different bioinks (2.5% MeHA, 5% GelMA, 5% PEGDA, 2% NorHA) at day 7. Reproduced, with permission from [3]
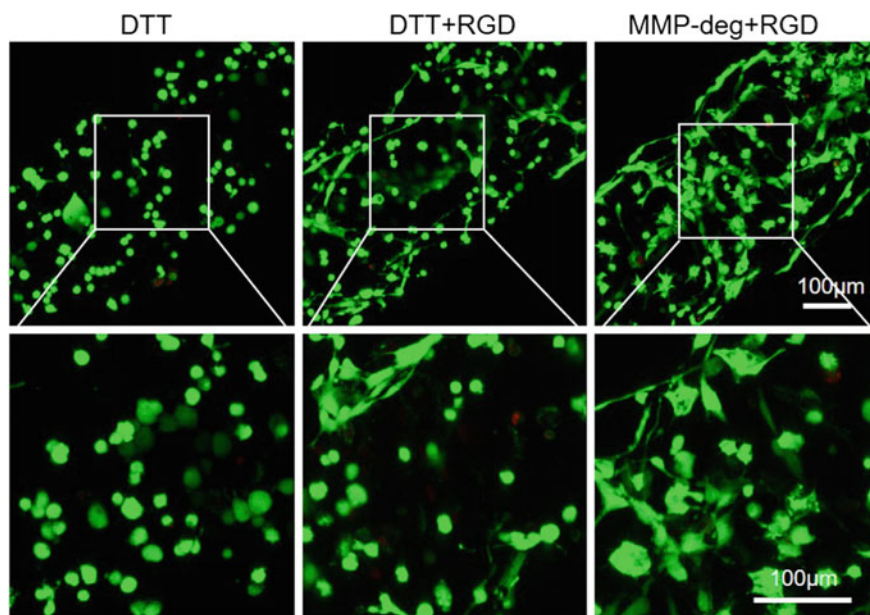
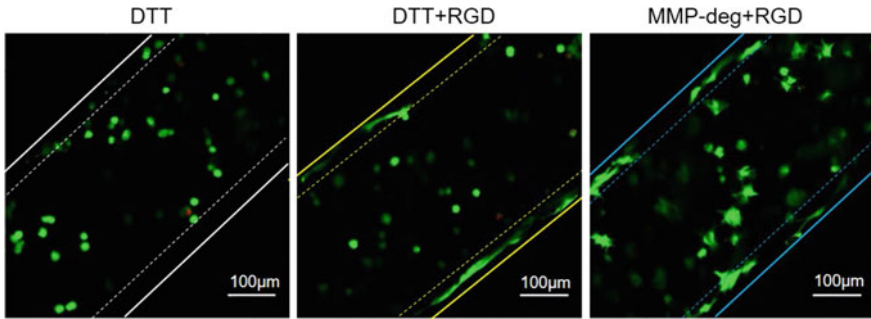**Fig. 7.27** Fluorescence images of 3T3 cells embedded in filaments printed from NorHA bioinks with varied functionalizations. Calcein-AM is indicated as green, and images are captured at day 7. Reproduced, with permission from [3]

Fig. 7.28 Confocal images of cell-laden filaments (sliced at the maximum dimension) printed from NorHA with varied functionalization, showing cell morphology at the near-surface (thin area between solid and dot lines) and inner (are between dot lines) locations. Calcein-AM is indicated as green, and images are captured at day 7. Reproduced, with permission from [3]
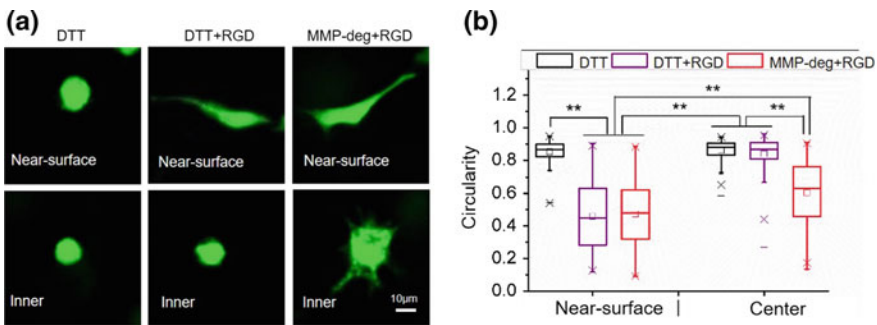
Fig. 7.29 **a** Representative images of single cell and **b** quantified cell circularity at day 7 in near-surface and inner locations of NorHA filaments with varied functionalizations. Reproduced, with permission from [3]

distribution of cells along the cross section (Fig. 7.28). To distinguish the difference of cell morphology in different regions, we define an inner region within the area of 80% diameter, the area out of which is defined as the near-surface region. Cells were consistently round in both regions in the DTT group, while adding RGD in the formulation would help cells in the near-surface region spread (Fig. 7.29a). By introducing both MMP-degradable network and RGDs in the formulation, cells were elongated or spread throughout the filament. These observations were further confirmed by the quantified circularity of single cells in different regions (Fig. 7.29b).

To summarize, bioinks types, RGD incorporation, and degradation kinetics were investigated regarding their effects on fibroblast in 3D-bioprinted filaments. It can be concluded that cells might behave differently at different positions in 3D, and both RGD and the degradable crosslinking network would enhance cell spreading. These results also demonstrated that the in situ crosslinking strategy could act as a platform technology with the capability of applying varied material cues for cell behavior tuning.

References

1. Ouyang L, Yao R, Chen X, Na J, Sun W (2015) 3D printing of HEK 293FT cell-laden hydrogel into macroporous constructs with high cell viability and normal biological functions. Biofabrication 7(1):015010
2. Ouyang L, Yao R, Mao S, Chen X, Na J, Sun W (2015) Three-dimensional bioprinting of embryonic stem cells directs high-throughput and highly uniform embryoid body formation. Biofabrication 7(4):044101
3. Ouyang L, Highley CB, Sun W, Burdick JA (2017) A generalizable strategy for the 3D bioprinting of hydrogels from nonviscous photo-crosslinkable inks. Adv Mater 29(8)
4. Park J, Cho CH, Parashurama N, Li Y, Berthiaume F, Toner M, Tilles AW, Yarmush ML (2007) Microfabrication-based modulation of embryonic stem cell differentiation. Lab Chip 7(8):1018–1028
5. Messana JM, Hwang NS, Coburn J, Elisseeff JH, Zhang Z (2008) Size of the embryoid body influences chondrogenesis of mouse embryonic stem cells. J Tissue Eng Regen Med 2(8):499–506
6. Hwang YS, Chung BG, Ortmann D, Hattori N, Moeller HC, Khademhosseini A (2009) Microwell-mediated control of embryoid body size regulates embryonic stem cell fate via differential expression of WNT5a and WNT11. Proc Natl Acad Sci U S A 106(40):16978–16983
7. Itskovitz-Eldor J, Schuldiner M, Karsenti D, Eden A, Yanuka O, Amit M, Soreq H, Benvenisty N (2000) Differentiation of human embryonic stem cells into embryoid bodies comprising the three embryonic germ layers. Mol Med 6(2):88–95
8. Ohnuki Y, Kurosawa H (2013) Effects of hanging drop culture conditions on embryoid body formation and neuronal cell differentiation using mouse embyonic stem cells: optimization of culture conditions for the formation of well-controlled embryoid bodies. J Biosci Bioeng 115(5):571–574
9. Weeks CA, Newman K, Turner PA, Rodysill B, Hickey RD, Nyberg SL, Janorkar AV (2013) Suspension culture of hepatocyte-derived reporter cells in presence of albumin to form stable three-dimensional spheroids. Biotechnol Bioeng 110(9):2548–2555
10. Liu HY, Korc M, Lin CC (2018) Biomimetic and enzyme-responsive dynamic hydrogels for studying cell-matrix interactions in pancreatic ductal adenocarcinoma. Biomaterials 160:24–36
11. Dorsey SM, McGarvey JR, Wang H, Nikou A, Arama L, Koomalsingh KJ, Kondo N, Gorman JH 3rd, Pilla JJ, Gorman RC, Wenk JF, Burdick JA (2015) MRI evaluation of injectable hyaluronic acid-based hydrogel therapy to limit ventricular remodeling after myocardial infarction. Biomaterials 69:65–75
12. Stowers RS, Allen SC, Suggs LJ (2015) Dynamic phototuning of 3D hydrogel stiffness. Proc Natl Acad Sci U S A 112(7):1953–1958
13. Khetan S, Guvendiren M, Legant WR, Cohen DM, Chen CS, Burdick JA (2013) Degradation-mediated cellular traction directs stem cell fate in covalently crosslinked three-dimensional hydrogels. Nat Mater 12(5):458–465

Chapter 8
Conclusions and Future Work

This chapter concludes the main contributions and findings of this thesis, followed by some suggestions regarding future directions in the field of bioprinting.

8.1 Concluding Remarks

Based on the bioink crosslinking mechanisms, this thesis systematically studies the microextrusion 3D bioprinting, covering the key aspects related to materials science, manufacturing engineering, and cell biology. After reviewing the state-of-the-art (Chap. 2), we carry out a comprehensive analysis of the bioprinting process with the synergy between techniques and bioinks, which leads to guidelines regarding general criteria and research route (Chap. 3). Following this guideline, we then carry out three novel case studies based on different bioink systems, which comprehensively shows how to perform a successful bioprinting practice (Chaps. 4–6). Considering the varied features of the techniques developed, we apply the most suitable ones to some specific applications, such as embryoid body formation and cell–matrix interaction (Chap. 7). The **novel contributions** of this doctoral research are summarized below.

(1) A secondary crosslinking strategy is developed for 3D printing self-assembly guest–host HA bioinks. The printed constructs exhibit excellent structural fidelity and mechanical property as tissue engineering scaffolds. This work clarifies some key issues regarding structure printability and stability with the use of supramolecular hydrogels for 3D printing applications.

(2) A synergetic optimization approach combining rheological characterization with bioprinting practice is developed for the typical gelatin–alginate bioink. By introducing a facile image analysis approach, we could quantify the printability and couple it with cell viability to achieve physically and biologically ideal outcomes. This reliable and versatile approach can easily characterize the printability and has been adopted by other researchers.

(3) An entirely new bioprinting strategy for photo-crosslinkable bioinks is developed, which allows for the use of non-viscous formulations for cell printing, breaking the enduring limit to ink viscosity. Due to the reduction of shear force with using low-viscosity materials, high cell viability (>90%) could be maintained. Moreover, this in-situ crosslinking approach could be easily generalized to different photo-crosslinkable bioinks and varied heterogeneous structures.

(4) Based on the developed bioprinting systems, we demonstrate the successful activation of Wnt signal pathway in 3D constructs. Moreover, a bioprinting-based, high-throughput EB generation system is developed, with the maintenance of almost 100% pluripotency. This lays the basis for pluripotent stem cells assembly and differentiation in 3D complex model.

(5) A practical guideline for microextrusion 3D bioprinting is developed, which is proved to be helpful by the comprehensive case studies. The guideline covers general criteria and research route, together with specific experimental methods regarding characterization. The building block, which is the gel filament in the case of microextrusion bioprinting, is highlighted throughout the studies, giving rise to a better understanding of this bottom-to-up methodology.

Moreover, other **key findings** can be concluded as follows.

(1) Ink material is the core element of microextrusion bioprinting. The crosslinking mechanisms and rheological properties would directly determine the printing process and structural outcomes, while various materials cues would affect the biofunctionality.

(2) From the perspective of bioink, bioprinting process could be generally divided into three stages, namely bioink formulation, gel filament, and 3D structure. The filament formation and deposition are found to be key steps in between, corresponding to the primary and secondary crosslinking mechanisms, respectively. Thus, different bioprinting techniques might be possibly generalized to a "secondary crosslinking" methodology. This has been demonstrated by all the cases studied in this thesis and should be helpful to for future technology development.

(3) The guest–host supramolecular hydrogels share good printability due to the self-assembly and self-healing properties. Such formulation would perfectly serve as a primary crosslinking component for printability achievement.

(4) Gelatin-based formulations exhibit significant time-delayed properties when the temperature changes. This means that printing time, which is usually neglected, should be taken into consideration.

(5) The in situ crosslinking strategy contributes to the use of low-viscosity inks and has comprehensive advantages over pre-crosslinking and post-crosslinking in terms of cell protection, ink type expansion, and microfilament complex structure expansion.

(6) In 3D-bioprinted gelatin–alginate constructs, embryonic stem cells turn to proliferate in situ to form an embryoid body (EB), which comprehensively performs better in EB uniformity and yield than aggregating-based approaches.

8.2 Future Research Directions

The contributions in this dissertation can add to the reference and lead to new lines of inquiry in the field of 3D bioprinting. Some key challenges remain and several new questions emerge. Based on what has been achieved here, a few of the most promising directions are listed as follows:

(1) Generalization solution

Many of the current bioprinting techniques are bioink-specific, which might hinder the exploitation. One of the future directions for bioink and bioprinting process development is toward generalization and simplicity. For example, by breaking the limit of bioinks in terms of polymer type, density, and formulation viscosity, an easy-to-choose bioink bank could be established based on a generalizable guideline. The simplification of the bioprinting process would contribute easier access for people, such as surgeons, who care more about the results. Such generalization solution would cover the development of new bioinks and printing strategies. Chapter 6 has given a successful trial in this direction and more work should be done in terms of resolution and printing speed.

(2) Machine learning

In addition to the development of generalizable strategy, what could also be done is to apply machine learning to the bioprinting system. The motivation for this is the need for careful parameter control during bioprinting. This would be especially helpful for processing some time-dependent bioinks, such as ECM hydrogels and gelatin-based hydrogels as studied in Chap. 5. By doing this, printers would be ideally expected to tune the printing parameter configurations intelligently based on the online feedback (e.g., rheology).

(3) 4D bioprinting

4D printing emerges as a concept of printing shape-change construct, which presents time as the fourth dimension. By assigning the 3D architecture with a movement or deformation, a dynamic complex construct could be engineered, which could be used in soft robotics and related areas. There has been some progress in this topic, manly based on shape-change polymer materials. 4D bioprinting has been proposed recently, with rarely few reports showing the proof-of-concept based on cell seeding strategy. More work should be done in this direction, either investigating new mechanisms for shape change or incorporating cells and biofunctional components for creating living system.

(4) Integrated bioprinting platform

The future bioprinting system would be desired to cover multiple functions, ranging from model scanning, CAD reconstruction, bioprinting, culturing, and characterization. Such bioprinting platform could be programmed to carry out the desired route corresponding to the specific application case. The integrated system is supposed to increase reproducibility and efficiency.